Markerless Motion Correction For Better Image Quality in Brain MRI

Slipsager, Jakob Mølkjær

Publication date:
2022

Document Version
Publisher's PDF, also known as Version of record

Technical University of Denmark
Department of applied mathematics and computer science

PHD THESIS

JAKOB MØLKJÆR SLIPSAGER

Markerless Motion Correction For Better Image Quality in Brain MRI

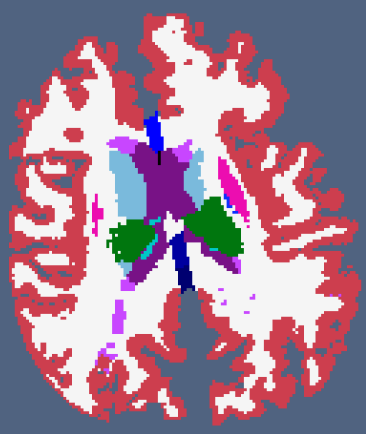

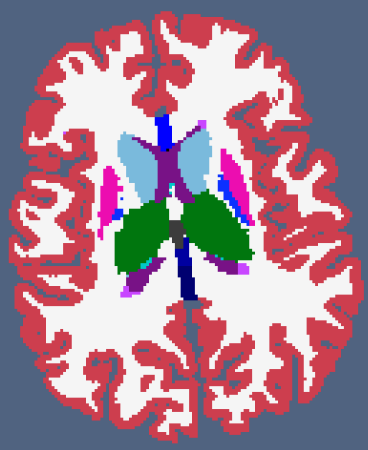

Supervisors:
Dr Rasmus R. Paulsen
Dr Stefan L. Glimberg
Dr Vladimir Fedorov
Professor Liselotte Højgaard

Assessment Committee:
Professor Aasa Feragen
Dr Ender Konukoglu
Dr Aaron T. Hess

Markerless Motion Correction For Better Image Quality in Brain MRI

Jakob Mølkjær Slipsager
Department of Applied Mathematics and Computer Science
Technical University of Denmark, Denmark
Richard Petersens Plads, Bygning 324, 2800 Kgs. Lyngby

Academic Advisors

Professor Liselotte Højgaard, MD, DMsc
Department of Clinical Physiology, Nuclear Medicine & PET
Rigshospitalet, Copenhagen University Hospital, Denmark

Rasmus R. Paulsen, PhD
Department of Applied Mathematics and Computer Science
Technical University of Denmark, Denmark

Vladimir Fedorov, PhD
TracInnovations, Denmark

Stefan L. Glimberg, PhD
TracInnovations, Denmark

Assessment Committee

Professor Aasa Feragen, PhD
Department of Applied Mathematics and Computer Science
Technical University of Denmark, Denmark

Professor Ender Konukoglu, PhD
Department of Information Technology and Electrical Engineering.
Eidgenössische Technische Hochschule Zürich, Switzerland

Aaron T. Hess, PhD
Centre for Clinical Magnetic Resonance Research
University of Oxford, United Kingdom

Summary

A correct diagnosis is paramount for effective treatment of patients. Today, medical imaging is an important part of modern diagnostics, where various non-invasive imaging modalities offer information about antonymy and physiology. One of the imaging modalities is magnetic resonance imaging (MRI). MRI provides anatomical images with high soft-tissue contrast without ionizing radiation, making it a powerful tool for neuroanatomical imaging, both for clinical and research use. A prerequisite for high-quality MRI images is that the subject remains motionless during the data acquisition; otherwise, the image series become motion degraded. However, it is challenging for many patients not to move during multiple MRI sequences that each takes several minutes to complete. Thus, patient motion during MRI is a major concern, and unintended motion leads to insufficient diagnostics image quality and significant revenue loss due to the cost of repeated sequences and expenses to anesthesia or sedation. Therefore, various motion correction (MC) solutions have been developed, showing promising results. However, only a fraction of them is commercially available today, and these solutions are limited to specific sequences and motion types.

This thesis aims to improve the quality of brain MRI by introducing markerless MC to obtain more accurate diagnostics and research results with minimal patient interaction. Further, this thesis examines the additional expenses of head motion and the potential savings of installing MC.

Cost analysis with assumptions estimated the annual cost of head motion to be more than $370,000 per scanner. Based on the cost analysis, repayment periods of MC solutions were calculated as a function of their implementation cost and

performance. The most conservative model showed that an MC solution with a 50% success rate would be financially viable after five years if the installation cost is below $47.000.

The markerless motion tracking system used in this thesis estimates head motion by continuously aligning surface scans of the patient's face back to the initial recorded surface scan. These alignments are performed with a high temporal resolution, allowing for frequent MC updates. Depending on the used MC technic, the markerless MC approach can be used clinically with minimal modification to the existing routine since no patient interaction is necessary.

The motion tracker was demonstrated with two fundamentally different MC methods. Prospective MC (PMC) corrects motion in real-time by updating the scanner's field of view during the data acquisition, while retrospective MC (RMC) corrects motion in the already acquired data as a post-processing step. Both methods come with benefits and trade-offs. PMC is able to provide better correction, while RMC is more robust and can be implemented independently of the scanner. Therefore, in vivo experiments of healthy volunteers were performed to compare the correction capabilities of PMC and RMC. Both methods caused a substantial improvement in the image quality compared to the uncorrected images. Direct comparisons of the two tested MC methods showed that PMC leads to better quality images in every test.

A combined version of PMC and RMC was introduced to accommodate some of the main disadvantages of PMC and RMC. This hybrid MC method was used to demonstrate "reverse" MC to generate the original uncorrected image from scans acquired with PMC.

MC using markerless motion tracking is a promising solution to improve the image quality of brain MRI due to minimal patient interaction and scanner independence. Markerless PMC was shown to have superior correction capabilities compared to RMC and could correct for more significant motion. RMC using markerless tracking works completely independent from the scanner and can be applied without modifying the existing protocol. Hence, RMC is a more mature solution for clinical implementation.

Summary (Danish)

En korrekt diagnose er alt altafgørende for effektive behandling af patienter. I dag er medicinsk billeddannelse en vigtig del af moderne diagnostik med flere forskellige billedmodaliteter, der tilbyder information om anatomi og fysiologi. En af disse billedmodaliteter er magnetisk resonans (MR). MR optager anatomiske billeder med høj blødtvævs kontrast uden brug ioniserende stråling, hvilket gør MR ideelt til at tage neuroanatomiske billeder til både forsknings og klinisk brug. En forudsætning for at MR kan tage højkvalitets billeder er at patienten ligger stille under hele skanningen, ellers bliver billederne ødelagt af bevægelsen. Det er dog svært for mange patienter ikke at bevæge sig under hver eneste MR sekvens der hver især tager flere minutter at optage. Derfor er patientbevægelse et stort problem for MR, da patientbevægelse fører til billeder med utilstrækkeligt diagnostisk kvalitet og øgede udgifter på grund af genskanninger og anæstesi. Derfor er flere forskellige bevægelseskorrektion (BK) metoder blevet udviklet med lovende resultater. Dog er det kun en lille del af de foreslåede metoder, der er kommercielt tilgængelige i dag, og dem der er tilgængelige, er begrænset til specifikke sekvenser og bevægelsestyper.

Målet med denne afhandling er at forbedre billedekvaliteten i hjerne MR-billeder ved at introducere markørløst BK for mere præcis diagnostik og forskning, med minimal patient interaktion. Yderligere undersøger denne afhandling omkostningerne ved hovedbevægelse og de mulige besparelser ved at bruge BK.

En omkostningsanalyse med antagelser estimerer de årlige hovedbevægelsesudgifter til at være mere end $370.000 pr. scanner. Baseret på resultaterne af ovenstående analyse blev tilbagebetalingsperioder på forskellige BK-løsninger udregnet som funktion af implementeringsprisen og korrektionsydeevnen. Her

viste den mest konservative model, at en BK-løsning med en succesrate på 50% vil være finansiel fordelagtig efter fem år, hvis prisen for løsningen holders under $47.000.

Det markørløse bevægelsesmonitoreringssystem brugt i denne afhandling, estimerer hovedbevægelse ved kontinuerligt at ensrette overfladeskanninger af patientens ansigt tilbage til referenceoverfladeskanningen. Disse ensrettelser bliver udført med en høj tidslig opløsning og muliggør BK med hurtig opdateringshastighed. Afhængig af den brugte BK-metode kan markørløs BK blive brugt klinisk uden modifikationer af de eksisterende rutiner, da ingen patientinteraktion er nødvendig.

Bevægelses-monitoreringsenheden blev testet med to fundamental forskellige BK-metoder. Prospektiv BK (PBK) korrigerer bevægelse i realtid, ved at opdatere skanners synsfelt under optagelsen af data, imens korrigerer retrospektiv BK (RBK) bevægelse i det allerede optaget data som et post processerings step. Begge metoder kommer med fordele og ulemper. PBK laver bedre korrektion, mens RBK er mere robust og kan blive implementere uafhængigt af skanneren. Derfor blev korrektionsegenskaberne af PBK og RBK sammenlignet i in vivo eksperimenter af raske forsøgspersoner. Begge metoder førte til en betydelig forbedring af billedkvaliteten sammenlignet med de ukorrigered billeder. Direkte sammenligninger af de to metoder viste at PBK førte til billeder med en bedre kvalitet i hvert eksperiment.

En kombination af PBK og RBK blev introduceret til at i møde gå nogle af begrænsningerne med PBK og RBK. Denne hybrid BK-metode blev brugt til at vise "omvendt" BK til at generere det ukorrigerede billede fra skanninger optaget med PBK.

BK med brug af markørløst bevægelsesmonitorering er en lovende løsning til at forbedre billedkvaliteten af hjerne MR på grund af dens minimal patient interaktion og skanner uafhængighed. Markørløs PBK viste sig at have bedre korrektions egenskaber sammenlignet med RBK og kunne korrigere for mere signifikant bevægelse. RBK ved brug af markørløs monitorering virker fuldstændigt uafhængigt af skanneren og kan blive indført uden at ændre eksisterende skannings protokoller. Således er RBK en mere moden løsning for klinisk integrering.

Acknowledgements

First of all, I would like to thanks my supervisors, Rasmus Paulsen, Stefan Glimberg, Vladimir Fedorov, and Liselotte Højgaard.

Big thanks to Ellen Grant, Borjan Gagoski, and Camilo Jaimes from Boston Children's Hospital and André van der Kouwe, and Robert Frost from the Athinoula A. Martinos Center for facilitating my stay abroad.

I would like to thank all my colleagues in TracInnovations for sharing an excellent working environment both socially and academically.

A special thanks to Oline V. Olesen for your guidance as my supervisor for the first half of my Ph.D.

I am also grateful to TracInnovations and Innovationsfonden for providing funding for my Ph.D. project.

Thank you to the section for Visual Computing at DTU Compute for being my academic host.

A huge thanks to all the patients and volunteers who have participated in my studies.

And finally, thanks to the clinical staff at Dept. of Clinical Physiology, Nuclear Medicine & PET, Rigshospitalet for data collection and review.

List of Publications

This thesis is based on the following studies:

I **Slipsager JM**, Glimberg SL, Søgaard J, Paulsen RR, Johannesen HH, Martens PC, Seth A, Marner L, Henriksen OM, Olesen OV, Højgaard L. *Quantifying the Financial Savings of Motion Correction in Brain MRI: A Model-Based Estimate of the Costs Arising From Patient Head Motion and Potential Savings From Implementation of Motion Correction.* Journal of Magnetic Resonance Imaging, 2020,52(3), 731-738

II **Slipsager JM**, Ellegaard AH, Glimberg SL, Paulsen RR, Dylan TM, Wighton P, Van Der Kouwe A, Marner L, Henriksen OM, Law I, Olesen OV. *Markerless motion tracking and correction for PET, MRI, and simultaneous PET/MRI.* Plos one, 2019, 14(4), e0215524

III **Slipsager JM**, Glimberg SL, Højgaard L, Paulsen RR, Wighton P, Tisdall D, Jaimes C, Gagoski BA, Grant PE ,van der Kouwe A ,Olesen OV, Frost R. *Comparison of prospective and retrospective motion correction in 3D-encoded neuroanatomical MRI.* Accepted for publication in Magnetic Resonance in Medicine.

List of Abbreviations

CT	Computed Tomography
ET	Echo Train
FLASH	Fast Low Angle SHot
FOV	Field Of View
GRAPPA	GeneRalized Autocalibrating Partial Parallel Acquisition
HMC	Hybrid Motion Correction
IFFT	Inverse Fast Fourier Transformation
INUFFT	Inverse Non-Uniform Fast Fourier Transformation
MC	Motion Correction
MPRAGE	Magnetization Prepared RApid Gradient Echo
MRI	Magnetic Resonance Imaging
NMR	Nuclear Magnetic Resonance
PET	Positron Emission Tomography
PMC	Prospective Motion Correction

PROPELLER	Periodically Rotated Overlapping ParallEL Lines with Enhanced Reconstruction
RF	Radiofrequency
RMC	Retrospective Motion Correction
RMS	Root Mean Square
SSIM	Structural Similarity Index Measure
TR	Repetition Time

Contents

Chapter 1

Background

Accurate and correct diagnoses are paramount for the most effective treatment of patients, and a significant part of modern diagnostic is medical imaging. Imaging modalities such as Computed Tomography (CT), Positron Emission Tomography (PET), and Magnetic Resonance Imaging (MRI) reveal information about the anatomy and physiology of the body by non-invasively capturing images "through the skin". The information provided by medical imaging improves physicians' ability to make the correct diagnoses and hence choose the best treatments for patients [1]. Many research settings are heavily dependent on medical imaging to advance our understanding of, e.g., human anatomy, physiology, and pathophysiology. As an example, high resolution cardiac CT images have been used to quantify the shape of the left atrial appendage [2].

MRI is a sophisticated imaging modality developed in the 1970s for which Paul C. Lauterbur and Peter Mansfield were awarded the Nobel Prize in Physiology and Medicine. They independently developed a method to spatially encode Nuclear Magnetic Resonance (NMR) signals to form an image [3]. Hospitals installed the first clinical scanners in the 1980s, and today, MRI is a widely available diagnostic tool with more than 35,000 units installed in hospitals around the world. Structural MRI offers excellent soft-tissue contrast with many different contrast opportunities, without ionizing radiation unlike CT. MRI also provides the ability to image psychological mechanisms by, e.g., measuring the blood oxygen level in the brain [4] or measuring hyperpolarized ^{13}C injected

into the body [5]. This makes MRI a popular imaging modality, especially for neurological and pediatric examinations, and the popularity increases as the cost of MRI is driven down [6].

1.1 Motion Problem in MRI

An MRI examination can be an uncomfortable procedure due to its long examination times and uncomfortable environment. Patients must lie completely still in a narrow and often loud scanner bore. In a neurological examination, the patient's head is enclosed by the head coil[1]. A typical brain examination includes 4 to 6 imaging sequences, each taking 2 to 6 minutes, requiring the patient to lie in the scanner for more than 20 minutes. The uncomfortable environment and long examination time increase the risk of involuntary patient motion. Motion during the data acquisition results in motion artifacts such as blurring, ghosting, and ringing and thereby an overall reduction in image quality [7]. In clinical applications, low-quality images make the interpretation more difficult and increase the risk that the radiologist may not be able to see key diagnostic features. Figure 1.1 shows examples of MRI images corrupted by motion, ranging from minimal to large artifacts. The left image contains no motion artifacts and is optimal for clinical use. The image in the middle contains some motion artifacts and it is no longer optimal for clinical use but still usable, while the image to the right is corrupted by large motion and is not usable. In the clinic, repeating low-quality images is often necessary to obtain images with diagnostic quality. However, this strategy prolongs the examination time, causing reduced patient comfort and patient throughput. Andre et al. [8] estimated that the annual extra cost of repeating motion degraded sequences is approximately $115,000 per scanner. In pediatric MRI examinations, sedation or anesthesia are commonly used to mitigate motion, but these methods are associated with increased health risk and cost [9–11].

Although involuntary patient motion has been a known problem since the early days of MRI, the problem is growing. Reasons for this growth include increased popularity of MRI due to more affordable systems and that MRI scanners have become more sensitive to motion due to improved scanner hardware and more advanced pulse sequences [7].

[1] Plastic cage around the head measuring the MRI signals

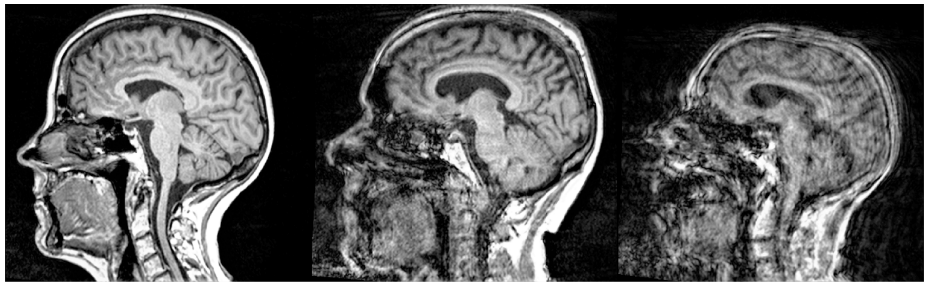

Figure 1.1: Sagittal slices from Magnetization Prepared RApid Gradient Echo (MPRAGE) scans corrupted by minimal (left), moderate (middle), and large (right) motion. The left image is optimal for diagnostic use, while the middle image can be used for diagnosis but is not optimal. The image to the right is not usable and needs to be repeated. From Slipsager et al. [12].

1.2 Image Acquisition and Reconstruction

This Section provides a brief overview of some key aspects of MRI data acquisition and image reconstruction of relevance to MPRAGE. An MRI scanner uses a powerful magnet to create a static and homogeneous magnetic field with a strength of several tesla (T). When a patient is placed inside the scanner, a fraction of the magnetic hydrogen nuclei in the body starts to align with the static field and precess around the field at a specific frequency. Pulses at the resonance frequency are used to excite the hydrogen nuclei. After the excitation, the NMR signal is measured by receiver coils around the patients [13].

To spatially localize the NMR signal, the scanner uses imaging gradient coils (G_x, G_y, and G_z) to create linear variations in the strength of the main magnetic field. The scanner does not spatially encode the entire image at once, as a regular camera does. Instead, it measures the spatial frequency components of the image, e.g. one line or readout of frequencies at a time. The frequency representation of an image is referred to as the k-space, and it is equivalent to the Fourier-space. In practice, the k-space representation of an image is a similar sized array of complex numbers. Each value at a given spatial frequency $\mathbf{k} = [k_x, k_y, k_z]^T$ contains information about the magnitude and phase of every pixel in the corresponding image. As an example, a value near the k-space center ($\mathbf{k} = [0, 0, 0]^T$) contains information about the low-frequency components of the image, which could, e.g., be large objects with homogeneous intensities.

An MRI sequence is a particular combination of Radiofrequency (RF) pulses and imaging gradients. A common anatomical sequence in brain MRI is the MPRAGE sequence. The sequence diagram in Fig. 1.2a illustrates how the

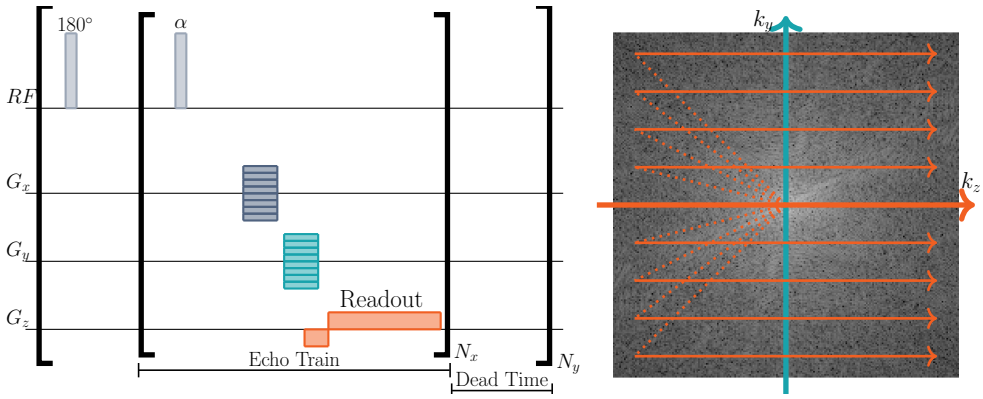

(a) Sequence diagram **(b)** K-space sampling

Figure 1.2: Illustration of how the scanner applies RF-pules and imaging gradients to populate k-space during an MPRAGE sequence. The MPRAGE sequence populates the 3D k-space through an inner and an outer loop illustrated by the square brackets. The inner loop is referred to as the echo train and varies the G_y-gradient, while the outer loop changes the G_z-gradient.

sequence manipulates magnetization to sample k-space. The first row in the diagram shows the applied RF pulses that invert and excite the NMR signal. The remaining rows show the activation time and amplitude of the imaging gradients. The MPRAGE sequence populates the 3D k-space through an inner and an outer loop. The inner loop, also known as the Echo Train (ET), samples frequency components in the k-space plane spanned by the k_z, and the k_y axes, as illustrated in Fig. 1.2b. The first line is sampled by applying a positive y-gradient combined with a negative z-gradient to move from the origin to the top left corner in k-space (dashed line). Then a readout is performed by applying a positive z-gradient while data are measured. This procedure is repeated by gradually decreasing the initial G_y amplitude until the entire k-space plane is populated. The amplitude of G_x is varied in the outer loop to sample all planes of the k-space. The MPRAGE k-space sampling process takes several minutes to complete, depending on the resolution and contrast. Patient motion during this time will usually result in artifacts in the final image due to inconsistency between various portions of the sampled k-space data [7].

The final image is reconstructed by an inverse Fourier transformation of the sampled k-space. In the majority of the clinical sequences, k-space is sampled on a Cartesian grid as in Fig. 1.2b to simplify the reconstruction by using the inverse fast Fourier transformation.

1.3 Estimation of Head Motion

Several of the Motion Correction (MC) approaches introduced later in Section 1.4 depend on accurate and precise estimates of the patient's head movements. Therefore, various motion tracking approaches have been proposed, and they can be divided into navigator, magnetic field detection, or optical methods [14].

Navigator methods estimate motion using the scanner itself without additional hardware [15–20]. In general, navigators are ultra-short MRI sequences that can quickly acquire data for processing in the k-space or image domain. These navigator sequences are interleaved in the host sequence[2] and are periodically executed throughout the scan.

Field detection methods [21–23] utilize a similar principle to the spatial encoding of the image data that points located at different positions in the scanner bore experience different magnetic fields. This concept is used to spatially encode the position of markers attached to the patient's head. The markers used in field detection are referred to in the literature as "active markers" and consist of a small sample of MRI visible material enclosed by a small receiver coil. The marker position is estimated by a short sequence of pulses executed by the scanner.

Optical methods use additional hardware in the form of, e.g., cameras, light sources, and markers to estimate motion, making the optical methods scanner and sequence independent. The majority of the proposed optical methods use one or more markers rigidly attached to the patient's head to estimate the motion [24–26]. However, Olesen et al. [27, 28] demonstrated a "markerless" tracking system for MC in PET and the system has since been redesigned to work in an MRI-scanner [29–32].

All three types of motion tracking methods come with their own trade-offs. Navigator and field detection methods add complexity to the pulse sequence, may add additional scan time, and have a lower temporal resolution than optical methods, meaning that motion estimates are less frequently available for MC. Due to scanner independence, optical systems can provide motion estimates to every MRI sequence. However, since these methods are independent add-on devices, they must be spatially and temporally calibrated (cross-calibration) to match the scanner's coordinate system.

[2] The sequence acquiring the high-resolution image

1.4 Motion Correction

Several motion-mitigation techniques have been proposed to reduce the negative impact of head motion [7, 14]. The most straightforward approach is to use fast or accelerated imaging sequences [33–35] to reduce patient discomfort and the risk of motion during the scan. Other approaches are head fixation using pads and motion robust sequences [36] utilizing (non-Cartesian) sampling strategies that are less sensitive to motion.

Frequently, these motion mitigation methods are not sufficient to provide the necessary image quality. Therefore, more advanced MC techniques have been developed. Overall, two different correction strategies exist: Retrospective Motion Correction (RMC) and Prospective Motion Correction (PMC).

1.4.1 Retrospective Motion Correction

The RMC approach takes place after the data acquisition and corrects the recorded data in the image or k-space domain. Retrospective correction of k-space was first introduced in 1989 by R. Ehman and J. Felmlee [37], who corrected k-space data for subject displacement by adding phase shifts according to motion estimated with navigator echoes. The concept of correcting the k-space trajectory according to how the subject was moving has been further developed to correct for rigid body motion in 3D [38–40]. An implementation of this method is described in Section 3.2.2.

The correction method by Ehman and Felmlee uses external knowledge about the subject motion, which was estimated with navigator echos interleaved in the imaging sequence. However, RMC approaches that work without prior knowledge about the motion have been suggested too. These methods iteratively correct the k-space trajectory to optimize image quality measures (e.g. entropy or gradient entropy) [41].

In the late 1990s, Pipe developed Periodically Rotated Overlapping ParallEL Lines with Enhanced Reconstruction (PROPELLER) [42]. This technique populates k-space by sampling a series of "blades" consisting of multiple parallel k-space lines. Each blade is rotated around the k-space center a certain number of degrees relative to the previously sampled blade. As a result, the k-space center containing the low-resolution image information is sampled during each blade. In the image reconstruction, the over-sampled k-space center is utilized to perform MC.

In recent years, several new MC approaches based on deep learning frameworks have been proposed. These methods use convolutional neural networks, variational autoencoders, or generative adversarial networks to remove motion artifacts directly in the image domain without knowledge about the motion [43,44].

1.4.2 Prospective Motion Correction

PMC is a group of methods where the correction is performed in real-time during the scan. PMC is achieved by continuously updating the scanner's Field Of View (FOV) to follow a moving object (e.g. a patient's head), as illustrated in Fig. 1.3. Special PMC sequences are designed to receive motion estimates and then update the scanner's FOV by adjusting the imaging gradients and system RF settings before a readout.

An early implementation of the PMC approach was introduced by Haacke and Patrick in 1986 [45] to correct periodic 1D chest motion in abdominal imaging. In the late 1990s, Lee et al. [46, 47] introduced the term "Prospective motion correction" in two papers proposing a novel method to correct inter-image motion in functional MRI using motion data estimated in real-time with navigator echos. Further development resulted in methods capable of correcting rigid-body motion in structural MRI images of the brain [15,16]. A recent study by Frost et al. [29] shows that increasing the update frequency of PMC in MPRAGE results in substantially better image quality of the corrected image during fast patient motion.

1.4.3 Current Use of Motion Correction

Although the development of MC has been underway for more than 30 years, and many of the developed methods have shown promising results, only a small fraction are available on clinical MRI systems today. The PROPELLER method is clinically available on scanners from all the major vendors under their own names (e.g Siemens "BLADE" or Phillips "MulitVane"). Another example is PROMO, introduced in 2010 by White et al. [16] which today is commercially available on scanners from GE. However, both methods are limited to specific sequences and does not handle all types of motion equally well.

MC is more commonly used in research applications, especially in functional MRI, where MC is often necessary to measure the functional MRI signal with a high signal-to-noise ratio. Also, in high resolution structural MRI of the brain, MC is applied to correct for artifacts caused by small involuntary motion e.g.

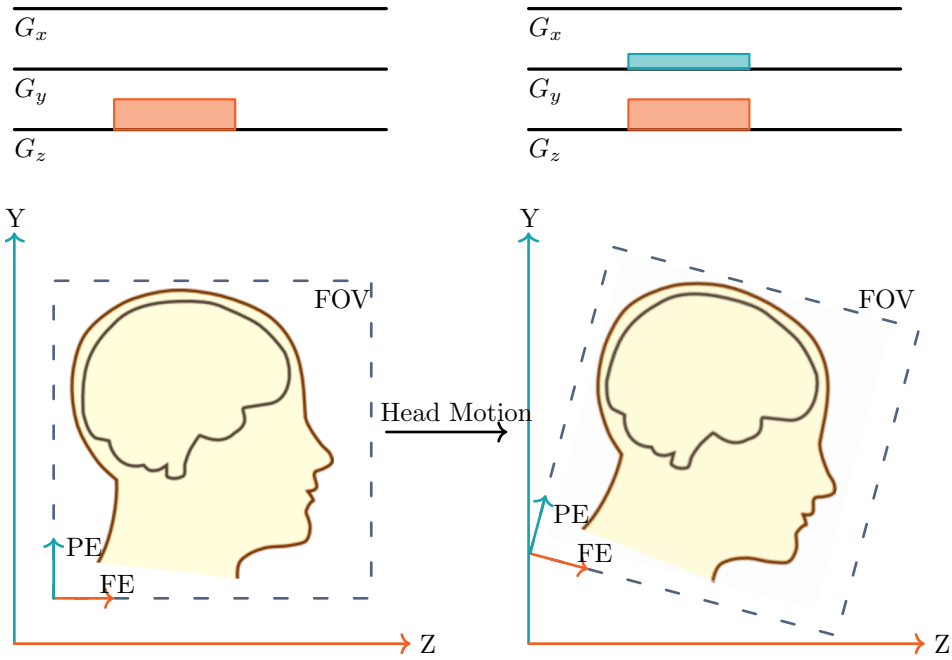

Figure 1.3: Illustration of how prospective motion correction adjusts the imaging gradients (G_x, G_y, and G_z) in order to change the Field of View (FOV) to follow a moving head. The left column illustrates the situation before head motion, while the right column shows how the scanner responses to head motion.

respiratory motion. In a recent study, Priovoulos et al. [48] could visualize the cerebellar cortical layers using a PMC-enabled Fast Low Angle SHot (FLASH) scan with voxel-size 0.2x0.2x1mm on 7T MRI system. The authors also show that the cortical layers were not visible when the scan was acquired without PMC on the same subject.

Chapter 2

Aim

The overall aim of this industrial Ph.D. project was to use motion correction to improve the image quality of structural brain MRI to achieve better diagnostics and reducing the many costs of involuntary head motion. This was achieved by the following intermediate aims:

1. To quantify the prevalence and the cost of motion degraded MRI images in a clinical setting and estimate the potential cost savings of applying motion correction.
2. To evaluate a markerless motion tracking device on clinical MRI protocols and to demonstrate prospective motion correction with markerless motion tracking.
3. To compare the correction performance of prospective and retrospective motion correction and investigate the effect of the correction frequency on the performance of retrospective correction.

Chapter 3

Summary of Methods

The following chapter summarizes the methods employed in this industrial Ph.D. thesis. For a detailed description, please refer to the "Materials and methods" sections in studies I-III.

3.1 Motion Estimation

Rigid-body head motion was estimated using the markerless tracking system Tracoline (TCL) (TracInnovations, Ballerup, Denmark). In study II, the TCL2 system was used, while study III used the TCL3 system. Both TCL versions consist of three main components: trolley, vision probe, and optical fibers as illustrated in Fig. 3.1 as well as the system software TracSuite. The trolley is a radio shielded box (Faraday cage) containing all the electronic components of the system, and it is located behind the scanner as shown in Fig. 3.2a. The vision probe contains non-electronic optical components, and it is mounted to the scanner table. It is positioned to have line of sight of the subject's face through the openings in the head coil (Fig. 3.2b). The optical fibers transfer light between the vision probe and the system electronics in the trolley. TracSuite, running on the tracking computer, controls the system electronics and processes the data to determine how the subject moves.

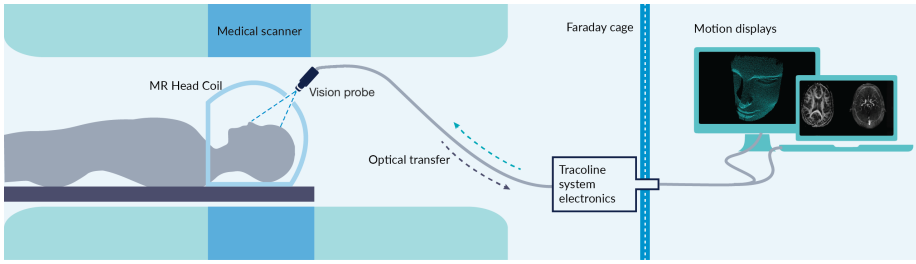

Figure 3.1: Schematic illustration of the TCL system integrated with the MRI scanner. From Slipsager et al. [30]

The TCL system estimates head motion by projecting near-infrared structured light on the face of the patient to reconstruct 3D point clouds of the face at a rate of 30 point clouds per second. Each point in the point cloud acts like a marker attached to the face, and the head motion is estimated by finding the motion between corresponding markers from a current point cloud to a reference point cloud. This is achieved by continuously performing rigid-body registrations using the iterative closest point algorithm between the two point clouds. The head motion is encoded in the 4x4 transformation matrix $\mathbf{T}(t)$ determined in the registration that aligns the two point clouds. An example of such head motion data is shown in Fig. 4.7.

3.1.1 Calibration of External Devices

The TCL system is an external tracking device, and the recorded motion is therefore defined in the tracking device's own coordinate system (tcs). A geometric calibration between the scanner and the TCL system is necessary to represent the estimated motion in the scanner's coordinate system (scs) before the motion estimates could be used for MC. For RMC, a temporal calibration is also required.

The geometric calibration is performed by extracting a point cloud of the patient's head from a special calibration scan on the scanner. In studies II and III, a high-resolution MPRAGE sequence was used as the calibration scan to generate a scanner point cloud representation of the face in the scanner's coordinate system. The geometric transformation ${}_{scs}\mathbf{A}_{tcs}$ that maps between the two coordinate systems tcs and scs was determined by aligning a point cloud from the tracking device to the point cloud from the scanner. The iterative closest point algorithm was used to perform the alignment. The motion defined in tcs

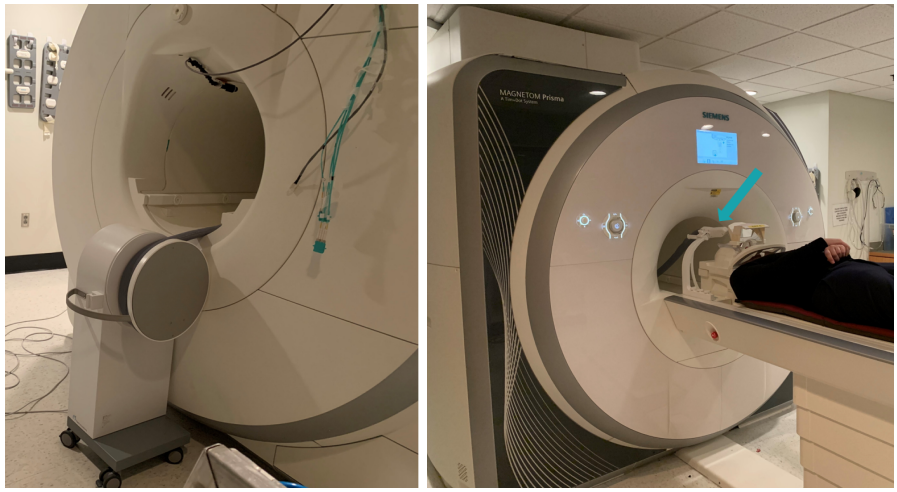

(a) System electronics **(b)** Vision probe

Figure 3.2: The setup of the TCL system on the Siemens MAGNETOM Prisma MRI scanner used in *study III*. The arrow indicates the TCL system's optics (vision probe). The vision probe is mounted to the scanner table to have sufficient visibility of the patient's face through the openings in the head coil.

${}_{tcs}\mathbf{T}_{tcs}(t)$ was transformed to scs by

$$ {}_{scs}\mathbf{T}_{scs}(t) = {}_{scs}\mathbf{A}_{tcs}\,{}_{tcs}\mathbf{T}_{tcs}(t)\,{}_{scs}\mathbf{A}_{tcs}^{-1} \tag{3.1} $$

The temporal calibration for retrospective matching of motion estimates to k-space data was performed by a network time synchronization between the scanner and the tracking computer.

3.2 Motion Correction

3.2.1 Prospective Motion Correction

PMC was enabled by modifying 3D-encoded FLASH (Study II) and 3D-encoded MPRAGE (Study III) sequences to adjust the imaging FOV according to motion estimates received from the TCL system [29, 49]. In study III, two different versions of PMC were implemented to examine the effect of the update frequency on the correction performance. In the first version, referred to as before echo train (Before-ET) PMC, the FOV was adjusted before each ET, resulting in a

FOV update every 2,500ms. In the second version, referred to as within echo train (Within-ET) PMC, the FOV was adjusted before each ET and before every six readouts inside an ET. This resulted in a FOV update every 48ms. Figure 3.3 shows where in the sequence the two different versions update the FOV. In study II, only a single version was created where the FOV was updated every Repetition Time (TR)(every 15ms).

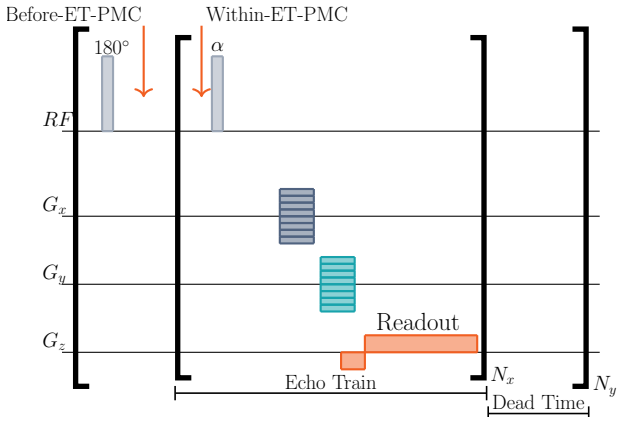

Figure 3.3: Diagram of the modified MPRAGE sequence for PMC used in study III. The orange arrows show were in the sequence the Before-ET, and Within-ET PMC versions update the FOV. Note that Within-ET PMC only updates the FOV every six readouts.

3.2.2 Retrospective Motion Correction

RMC was performed using a modified version of the freely available retroMoCoBox software package [50]. The first step in the RMC pipeline was to reconstruct missing k-space lines due to GeneRalized Autocalibrating Partial Parallel Acquisition (GRAPPA) acceleration [35]. After the GRAPPA-reconstruction, the conventional uncorrected image was reconstructed using an Inverse Fast Fourier Transformation (IFFT) (Fig. 3.4c). In the second step, each k-space readout was assigned with the closest recorded motion estimate in time, as illustrated in Fig. 3.4a. As a result, every readout was assigned with a 4x4 transformation matrix ${}_{tcs}\mathbf{T}_{tcs}(e,r)$ that encodes the subject's position relative to a reference position when the $r'th$ readout in the $e'th$ ET was performed. The assigned motion estimates were transformed from the motion tracker's coordinate system (tcs) into the scanner's coordinate system (scs) by

$$ {}_{scs}\mathbf{T}_{scs}(e,r) = {}_{scs}\,\mathbf{A}_{tcs}\,{}_{tcs}\mathbf{T}_{tcs}(e,r)\,{}_{scs}\mathbf{A}_{tcs}^{-1}, \tag{3.2} $$

where ${}_{scs}\mathbf{A}_{tcs}$ is the cross-calibration matrix between the motion tracker and the scanner. The k-space trajectory was updated by the assigned transformations. Translations were applied by adding additional phase shifts to the acquired k-space values by

$$\hat{I}_{ksp}(\mathbf{k}_{n,e,r}) = I_{ksp}(\mathbf{k}_{n,e,r})\mathrm{e}^{-i\pi(\mathbf{k}_{n,e,r}\mathbf{t}_{e,r})}, \tag{3.3}$$

where $\hat{I}_{ksp}$ is the phase shifted value, $\mathbf{t}_{e,r}$ is the assigned translations, and $\mathbf{k}_{n,e,r}$ is the $n'th$ k-space position within the $r'th$ readout in the $e'th$ ET. Correction of rotational motions was done by rotating each k-space readout according to the assigned rotations by

$$\hat{\mathbf{k}}_{n,e,r} = \mathbf{k}_{n,e,r}\mathbf{R}_{e,r}, \tag{3.4}$$

where $\hat{\mathbf{k}}_{n,e,r}$ is the rotated k-space position and $\mathbf{R}_{e,r}$ is the assigned rotation. The rotated k-space lines are illustrated in Fig. 3.4b. After the rotations were applied, the k-space was no longer uniformly sampled and the Inverse Non-Uniform Fast Fourier Transformation (INUFFT) [51] was used to reconstruct the motion corrected image (Fig. 3.4d).

3.2.3 Hybrid and Reverse Motion Correction

The correction frequency of data acquired with Before-ET PMC was retrospectively increased to reduce the residual motion during an ET using RMC. This Hybrid Motion Correction (HMC) approach is referred to as Within-ET HMC. The HMC method works by passing k-space data acquired with Before-ET PMC through the RMC pipeline to correct residual motion that occurred when the subject moved during an ET (see Fig. 3.6). The residual motion $\mathbf{T}_{res}$ was determined by:

$$\mathbf{T}(e,r)_{res} = \mathbf{T}^{-1}(e,0)\mathbf{T}(e,r), \tag{3.5}$$

where $\mathbf{T}(e,0)$ is the transformation that was used to update the FOV before the e'th ET and $\mathbf{T}(e,r)$ is the recorded transformation at the r'th readout in the e'th ET.

"Reverse" motion correction was performed on scans acquired with both Within-ET PMC and Before-ET PMC to reconstruct uncorrected versions of the scans. Reverse MC was achieved by passing prospectively corrected k-space data through the RMC pipeline. In the pipeline, the k-space trajectory was reversely corrected based on the inverted motion estimates used to update the FOV in real-time.

A final combination of PMC and RMC was used to retrospectively decrease the update frequency from Within-ET to Before-ET. This was done by reverse

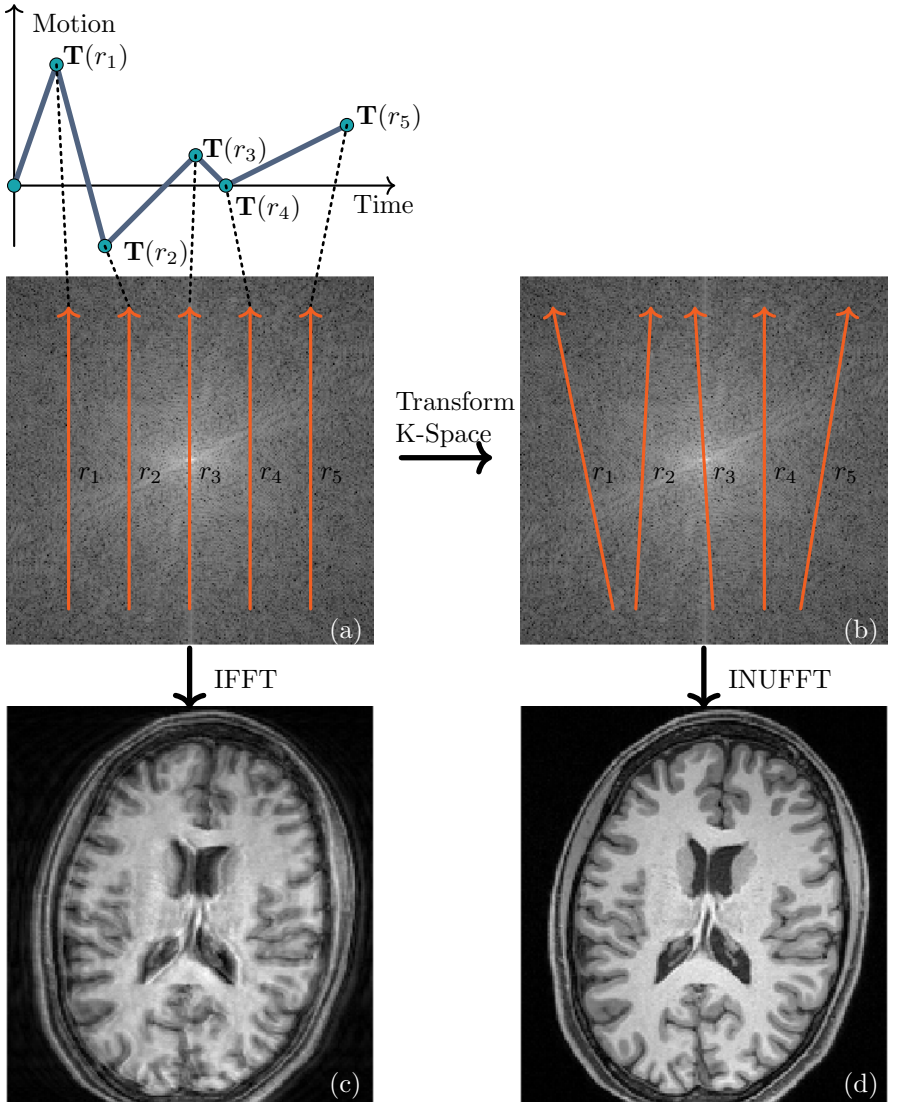

Figure 3.4: Illustration of the RMC pipeline. (a) Each k-space readout r is assigned with the nearest motion estimate $\mathbf{T}(r)$. (b) k-Space is updated according to the assigned motion estimates by rotations and phase shifts. (c) The uncorrected image is reconstructed by an inverse fast Fourier transformation of the original k-space. (d) The retrospective motion corrected image is reconstructed by an inverse non-uniform fast Fourier transformation of the corrected k-space.

correction of the k-space trajectory by the difference between the Within-ET and the Before-ET transformations. The transformation differences $\mathbf{T}_{diff}$ were determined by:

$$\mathbf{T}(e,r)_{diff} = \mathbf{T}^{-1}(e,r)\mathbf{T}(e,0), \tag{3.6}$$

3.3 Study I

Quantifying the Financial Savings of Motion Correction in Brain MRI: A Model-Based Estimate of the Costs Arising From Patient Head Motion and Potential Savings From Implementation of Motion Correction

3.3.1 Data

Two PET/MRI protocols with a total of 228 patients were retrospectively selected for this study: one protocol examining dementia patients and one protocol examining pediatric patients with brain tumors including, both pre- and postoperative examinations. A demographic overview of the selected patients is given in Table 3.1. Both protocols were performed on a Siemens mMR Biograph hybrid 3T PET/MRI scanner (Siemens Healthineers, Erlangen, Germany). The pediatric study was approved by the Danish National Committee on Health Research Ethics (ID: H6-2014-095), and all patients/parents gave written informed consent for participation in the study. For the dementia protocol, the retrospective use of patient data was approved by the Danish Patient Safety Authority (ref. 3-3013-1513/1).

In order to generalize to non-hybrid MRI scanners all PET and PET-related MRI sequences, e.g. for planning and attenuation correction were excluded from both selected protocols. Examinations with sedation or anesthesia were excluded under the assumption that motion is minimal in these examinations.

Table 3.1: Patient overview in study I

Protocol	Number of Patients	Median Age	Range
Dementia Patients	173	73 years	17-94 years
Pediatric Patients	55	11 years	0.1-19 years

Pediatric Patients with brain tumors including pre- and postoperative examinations.

3.3.2 Review of MRI Images

The image quality was quantified by assigning a score to each image series. The quality score was divided into three groups: score 1 = images optimal for clinical use; score 2 = images useful for diagnosis, but not optimal; and score 3 = nondiagnostic images, i.e., requiring a repeated scan. Three radiologists with 19, 5, and 4 years of experience reviewed all image series uploaded to PACS from the two protocols and assigned a quality score to each series. The radiologists were instructed to assign the quality score based only on the severity of motion related artifacts. Image series that only contained artifacts that were unrelated to motion were assigned with a score of 1. All image series were scored individually by the three radiologists and the median score was used as the final image score.

3.3.3 Estimation of Motion-Induced Cost

The financial costs of head motion were estimated in four different cost categories. Cost categories (1), (2), and (4) estimates the additional cost of head motion to the hospital while cost category (3) estimates the cost to the society. The cost estimates were calculated based on an MRI scanner performing 2000 brain examinations per year[1] and assuming that an examination consists of five MRI-sequences. The costs were estimated from the perspective of the Department of Clinical Physiology, Nuclear Medicine & PET, Rigshospitalet, Denmark. All assumptions used in this cost estimation model were assigned with lower and upper bound values to specify the uncertainty of the assumptions. Every cost category was calculated based on the lower and upper bound values. All assumptions and uncertainties used in the four cost categories are summarized in study I [12], Table 1.

Cost categories (1–4) estimates the following:

Cost Category (1) *The added extra costs to the clinic when motion-corrupted images are detected and repeated during the examination.* The cost of a standard MRI head examination, including staff expenses at the Department of Clinical Physiology, Nuclear Medicine & PET, Rigshospitalet was $555 per hour. Based on the results of the image quality review outlined in Section 4.1.1 it was found that the probability that a given sequence must be repeated was 2.0%. This probability was in a previous study [8] reported to 5.5% and this was used as an upper bound in the cost estimation.

[1] Corresponding to 8 examinations per day if the scanner operates only on weekdays.

Cost Category (2) *The additional costs to the clinic when motion-corrupted images are not detected or repeated during the examination.* If an examination contains an essential image series corrupted by motion that was not detected and repeated during the scan, a reexamination is necessary. It was assumed that the radiologist spends additional 20 minutes per examination to review and to refer the patient to a new MRI examination. It was assumed that the hourly rate of the radiologist was $111. Based on the image review in Section 4.1.1 it was found that 4.4% of the examination contains at least a single nondiagnostic sequence.

Cost Category (3) *The additional costs to society, as lost working earnings from the scanned patients, due to prolonged examination time.* As a consequence of head motion, it is common for the department to add a 30-minute time buffer in the patient information in case that nondiagnostic sequences need to be repeated. Due to this precaution, every patient loses 30 minutes. The cost categories were estimated from the perspective of Danish society. Here, Danish citizens' average working earning rate was approximately $33 per hour [52]. However, not all patients undergoing an examination are in a job due to their physical condition or age. For these patients, the time buffer will not result in lost working earnings. Therefore, it was assumed that 50% of the examined patients are within the working-age (18-70 years) and that 50% of these patients cannot maintain a job due to their condition. Hence, 25% of the examined patients were assumed to be working on the day of the MRI examination.

Cost Category (4) *The additional costs to the hospital or clinic when anesthesia is necessary to avoid motion in pediatric examinations.* In pediatric MRI examination, anesthesia is often used to avoid motion. In the referred department, an MRI examination with anesthesia increases the cost by $4433. It was assumed that pediatric examinations constitute 10% of the performed examinations and 36% of these scans were with anesthesia.

3.3.4 Savings When Implementing Motion Correction

The potential savings when implementing a MC system depend on the repayment period and how long the system continues to operate before it needs to be updated or replaced. This work focuses on the repayment period of the MC solution. The repayment period of a MC solution in a clinical workflow depends on the cost of subject motion, the MC implementation cost, and the performance of the implemented solution. Performance and implementation cost comparison of various MC methods were not the purpose of this work. The correction performance and implementation cost were therefore left as function variables in the cost-saving model. The repayment period of a MC solution was estimated as a function of the total cost of the solution and the performance, given as:

$$f\left(c,p\right)=\frac{c}{\sum_i\left[Cost\ category\ i)\right]p}, \tag{3.7}$$

where $f\left(c,p\right)$ is the repayment period, c is the implementation cost, and p is the MC performance rate. *Cost category i)* corresponds to the additional annual cost due to subject motion, as previously described in cost categories (1–4).

It was assumed in the model that all adult patients completed their scans. This assumption does not hold for pediatric patients, where anesthesia in some cases is necessary to obtain a diagnostic exam. In these cases, anesthesia is still necessary and MC will not have cost-saving effects. A solution to reduce the number of examinations with anesthesia is child-centered care suggested by Runge et al. [53]. The authors reported that 95% of the tested MRI examinations of 4-6 years old children were successfully completed without anesthesia after using their suggested method. The anesthesia rate for children in the age ranging from 4-10 years is reported as 47–75% in the literature [53]. Assuming uniformly distributed ages and that anesthesia was not used to scan children older than 11 years, the group of 4–10-year-old children corresponds to 64% of all scanned children <11 years old. Including the anesthesia rates for this group of children shows that 30-48% of the children were scanned with anesthesia. Using MC in combination with a similar solution as child-centered care [53] with a combined success rate of 95% (76% lower bound and 95% upper bound), it is assumed at that 37% (46% upper bound, 23% lower bound) would be able to complete a standard examination. In order to include the above assumptions in the repayment period calculation model in Eq. (3.7), 37% (46% upper bound and 23% lower bound) of cost category (4) should be used. For simplicity, the total implementation cost reflects the price of the combined MC solution.

3.4 Study II

Markerless motion tracking and correction for PET, MRI, and simultaneous PET/MRI.

3.4.1 Compatibility of TCL Within a Clinical PET/MRI Environment

To demonstrate the compatibility of the motion tracker in a clinical PET/MRI environment, the TCL2 system was used for motion tracking in the same pediatric protocol as previously described in Section 3.3.1. During the period between March 2015 and January 2018, the TCL2 system recorded head motion from 94 pediatric patients. The pediatric protocol consists of a 40 minutes ^{18}F-FET PET acquisition and six MRI sequences. The two last MRI sequences are acquired with the contrast medium Gadovist. The protocols of the performed MRI sequences are given in Table 3.2.

The motion tracking accuracy of TCL2 depends on rigid-body registration of the acquired points clouds representing the patient's face. The iterative closest point algorithm that aligns the points clouds imposes the assumption of rigid body motion of the tracked surface. Facial movements, occlusion, or insufficient visibility of the face may violate the rigid body assumption. Therefore, every estimated head pose of the 94 patients was analyzed against the reference point cloud, in order to determine how reliable the tracking results were. A tracking validity parameter with values ranging from 0 to 1 was introduced to indicate the tracking validity of each head pose. When the tracking validity parameter

Table 3.2: List of MRI sequences used in the pediatric PET/MRI protocol. From Slipsager *et al.* [30]

Sequence	Parameters	Voxel Size [mm]
T1 MPRAGE	9° flip angle TR/TE/TI 1900/2.52/900 ms	1.00x1.00x1.00
T1 TIRM	150° flip angle TR/TE/TI 2000/34/800 ms	0.45x0.45x4.00
T2 FLAIR	130° flip angle TR/TE/TI 9000/95/2500 ms	0.43x0.43x4.00
DWI	180° flip angle TR/TE 5600/61 ms	1.15x1.15x4.00
T2 BLADE(GD)	140° flip angle TR/TE 4000/118 ms	0.72x0.72x5.00
T1 MPRAGE(GD)	9° flip angle TR/TE/TI 1900/2.52/900 ms	1.00x1.00x1.00

(GD), Contrast enhanced sequences. Contrast medium Gadovist.

is equal or close to 1, it indicates high tracking validity and if the parameter becomes 0, the pose estimate is rejected.

3.4.2 PMC Using Markerless Tracking

To demonstrate PMC using a makerless tracking system for motion estimation, two in vivo experiments of healthy volunteers were performed. The performed experiments are summarized in Table 3.3. Each volunteer was scanned four times with the same PMC enabled FLASH sequence. In two of the scans (with and without PMC), the volunteers were instructed to remain motionless during the entire scan. In the two remaining scans also acquired with and without PMC, the volunteers were instructed to perform a repeatable motion pattern. Subject 1 was instructed to perform continuous motion with a moderate motion amplitude, while subject 2 was instructed to perform continuous motion with a high motion amplitude.

3.4.2.1 Data acquisition

The scans were performed on a Siemens mMR Biograph hybrid 3T PET/MRI scanner (Siemens Healthineers, Erlangen, Germany) with a 16-channel head coil. Image data were acquired with a 3D-encoded FLASH sequences with the following protocol: FOV 256x256x56mm^3 with 1x1x2mm^3 voxels (phase/read/slice directions respectively), bandwidth of 1000 Hz/pixel, TR of 15 ms, TE of 2.68 ms, and flip angle 35 degrees.

Table 3.3: List of the performed experiments in Study II

Session	Motion Pattern	Experiments	Performed Sequences
Subject 1	Continuous	The pattern was performed with medium and high motion amplitude.	Still, No PMC Still, PMC Motion, No PMC Motion, PMC
Subject 2	Continuous	The pattern was performed with medium and high motion amplitude.	Still, No PMC Still, PMC Motion, No PMC Motion, PMC

3.5 Study III

Comparison of prospective and retrospective motion correction in 3D-encoded neuroanatomical MRI.

3.5.1 Eexperiments

In vivo experiments of healthy volunteers were performed to investigate the correction performance of PMC and RMC. Furthermore, phantom experiments were performed to assess the effect of correction frequency on the performance during rapid motion. A summary of the performed motion patterns and sequences for each of the experiments is given in Table 3.4. An uncorrected scan without intentional motion was acquired for every subject as a ground truth image for the quantitative evaluation of the image quality. A total of six healthy volunteers were scanned in accordance with Institutional Review Board guidelines during the in vivo experiments. Each volunteer was trained before the scan using the real-time motion feedback provided by the TCL3 system to perform a repeatable head motion pattern. The training was necessary to obtain PMC data and uncorrected data (for RMC) corrupted by similar motion. In all experiments, MPRAGE scans using no MC and Within-ET PMC were acquired.

3.5.2 Comparison of PMC and RMC

Scans of subjects 1, 2, and 3 were designed to compare the correction performance of RMC and PMC during various types of motion patterns and motion amplitude. Subject 1, was instructed to perform a discrete motion pattern by changing head position (look right, up, left, down, back to center) at 1-minute intervals. Subject 2, was instructed to perform periodic continuous motion patterns by continuously changing head position by looking left to right for a 1-minute period. For both subjects 1 and 2, the pattern was performed with a medium and high motion amplitude. Subject 3, was instructed to perform both the discrete and the periodic continuous patterns in separate scans.

Table 3.4: List of the performed experiments in Study III. From Slipsager *et al.* [32]

Session	Motion Pattern	Experiments	Performed Sequences
Phantom	Continuous	Three experiments were performed, where the motion period began 0, 1, and 2 minutes into the sequence.	3 x No MC 3 x Before-ET-PMC 3 x Within-ET-PMC
Subject 1	Discrete	The pattern was performed with medium and high motion amplitude.	2 x No MC 2 x Within-ET-PMC
Subject 2	Continuous	The pattern was performed with medium and high motion amplitude.	2 x No MC 2 x Before-ET-PMC 2 x Within-ET-PMC
Subject 3	Discrete Continuous	Both the discrete and the continuous motion patterns were performed.	2 x No MC 2 x Within-ET-PMC
Subject 4	Discrete	The pattern was repeated in all 3 scans.	1 x No MC, External ACS 1 x No MC, Integrated ACS 1 x Within-ET-PMC, External ACS
Subject 5	Continuous	The pattern was repeated in all 3 scans.	1 x No MC, External ACS 1 x No MC, Integrated ACS 1 x Within-ET-PMC, External ACS
Subject 6	Discrete Continuous	Both the discrete and the continuous motion patterns were performed.	2 x No MC, No GRAPPA 2 x Within-ET-PMC, No GRAPPA

3.5.3 Motion Correction frequency experiments

A mechanical device compatible with the MRI environment was used to rotate a pineapple around the scanner's vertical axis. The pineapple was continuously moved back and forth for 1 minute while the MPRAGE sequence was running. The motion pattern was reproduced during MPRAGE scans with no MC, Before-ET PMC, and Within-ET PMC. This procedure was performed for three motion onset times, with the motion period beginning at approximately 0, 1, and 2 minutes into the sequences.

Scan session two (see Table 3.4) was also designed to test the effect of the update frequency on the performance; thus, MPRAGE scans with Before-ET-PMC were acquired.

3.5.4 Data acquisition and Reconstruction

The experiments were carried out on a Siemens 3 T Prisma scanner (Siemens Healthineers, Erlangen, Germany) using a 64-channel head coil. Raw data were acquired with a Cartesian 3D-encoded MPRAGE sequence using the following protocol: FOV=256x256 mm^2, matrix=256x256, 176 1 mm sagittal slices, in-plane GRAPPA R=2, TR=2500 ms, TE=3.3 ms, TI = 1070 ms, bandwidth=240 Hz/px, echo spacing=8 ms, and turbo factor=176.

In order to compare the correction performance of PMC and RMC all data were reconstructed using the RMC reconstruction pipeline to eliminate potential differences between the reconstruction running on the scanner and the offline RMC reconstruction. The flow chart in Fig. 3.5 shows the reconstruction of images corrected by the tested MC methods.

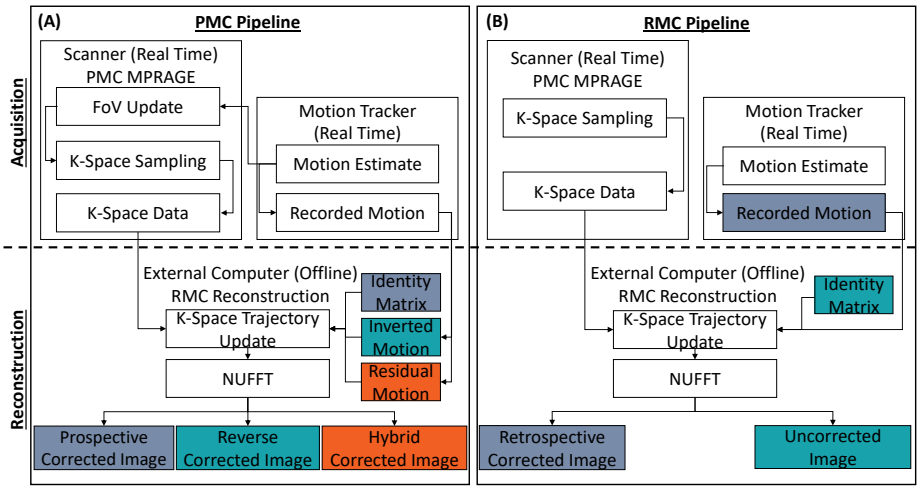

Figure 3.5: Flow chart showing the data acquisition and reconstruction pipeline used to generate images without MC, and with PMC, RMC, reverse MC, and HMC. Matching colors illustrate what type of motion a given image was corrected by. (A) Shows the pipeline for PMC data. The PMC takes place on the scanner while the hybrid and the reverse correction were performed during the reconstruction on an external computer. (B) Shows the pipeline for both RMC and without MC. From Slipsager *et al.* [32]

3.5.5 Quantification of Image Quality

The image quality of the reconstructed images was quantified by calculating the Structural Similarity Index Measure (SSIM) [54] using an uncorrected image without intentional motion as reference. Before calculating the SSIM, rigid registration using the Insight Toolkit [55,56] was performed to align each image to the reference image within a scan session. In addition, non-brain tissue was removed from each volume by a mask created from the reference image to ensure that each image volume only contains rigid structures.

3.5.6 Quantification of Motion

The head motion during a scan was quantified by calculating the Root Mean Square (RMS) discrepancy between the recorded motion $\mathbf{T}_{recorded}$ defined in the scanner's coordinate system and the identity matrix. The discrepancy $d(e,r)$ was determined as the average voxel displacement deviation over a 64 mm-radius sphere as suggested by Jenkinson in [57]. The RMS discrepancy was calculated over the entire scan by:

$$RMS_{discrepancy} = \sqrt{\frac{1}{ER}\sum_{e=1}^{E}\sum_{r=1}^{R} d(e,r)^2}, \tag{3.8}$$

where R is the number of readouts in an ET and E is the number of ETs.

The encoding error of MC was also quantified by calculating the RMS discrepancy. Here, the discrepancy was calculated between $\mathbf{T}_{true}(e,r)$ and $\mathbf{T}_{encode}(e,r)$. The transformation matrix $\mathbf{T}_{true}(e,r)$ describes the "true" subject position when readout r in ET e is acquired, while $\mathbf{T}_{encode}(e,r)$ describes the encoded position used to update the FOV. Examples of the discrepancy between the true and the encoded motion are shown in Fig. 3.6.

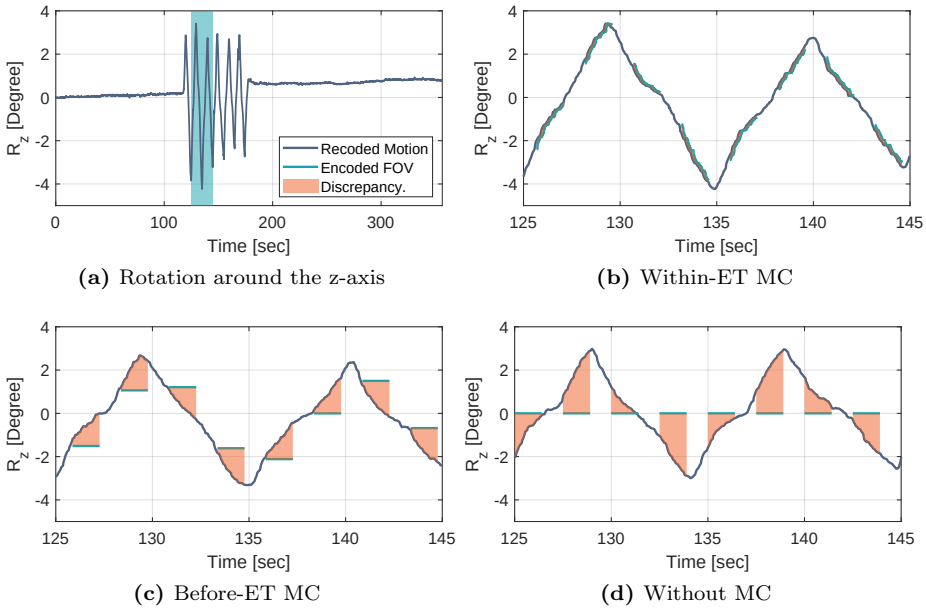

(a) Rotation around the z-axis

(b) Within-ET MC

(c) Before-ET MC

(d) Without MC

Figure 3.6: Discrepancy between the "true" motion and the encoded FOV of scan session 2, where the volunteer performed periodic continuous head motion with a medium amplitude. Only the discrepancy of rotation around the z-axis (R_z) is shown. The graph in (a) shows the recorded motion from the full scan, while (b-d) show magnification of R_z in the highlighted area during Within-ET MC, Before-ET MC, and no MC . Adapted from Slipsager *et al.* [32]

Chapter 4

Summary of Results

The following chapter summarizes the findings of this industrial Ph.D. thesis. To see all results, please refer to the "Results" sections in studies I-III.

4.1 Study I

The experiments performed in study I quantify the problem of patient head motion during MRI examinations and estimates the additional expenses of motion to the hospital and to society. Study I also addresses the potential savings of implementing a MC solution.

4.1.1 Prevalence of Motion Corrupted Images

The three radiologists reviewed 228 MRI examinations containing 1013 image series. All reviewed image series were assigned with a quality score according to the severity of motion artifacts. The three radiologists assigned the same score in 85.7% of the review sequences, and in 14.0% of the series, a single score was differently assigned. In 0.3% of the cases, the radiologists assigned all scores

differently. The median score was used in the cases with score disagreement. The results of the review are summarized in the left chart in Fig. 4.1. In 913 (90.1%) of the acquired sequences, the image quality was optimal for clinical use with minimal motion artifacts. Images corrupted by motion to a degree that it decreases the diagnostic utility (score 2) were observed in 80 (7.9%) of reviewed image series. Twenty (2.0%) of the reviewed image series were corrupted to a degree that they could not be used for diagnostics and should be repeated.

The total acquisition time of the 100 motion-corrupted sequences was ∼4.5 hours, corresponding to ∼3 minutes per sequence. Dividing the examination time into three equally sized bins shows that 23, 20, and 57 of the motion-corrupted sequences were acquired in the first, second, and third parts of the examination. This could indicate that the sequences obtained late in the examination are more likely to be motion corrupted. Either due to discomfort or fatigue for the patient or that the sequences performed late in the examination are more sensitive to motion.

The chart to the right in Fig. 4.1 shows the distribution of the 228 MRI examinations, with 10 (4.4 %) of the examinations containing one or more image series that needed to be repeated. It also shows that 42 (18.4 %) of the examinations contain a sub-optimal image series, and 176 (77.2 %) only contain optimal image series.

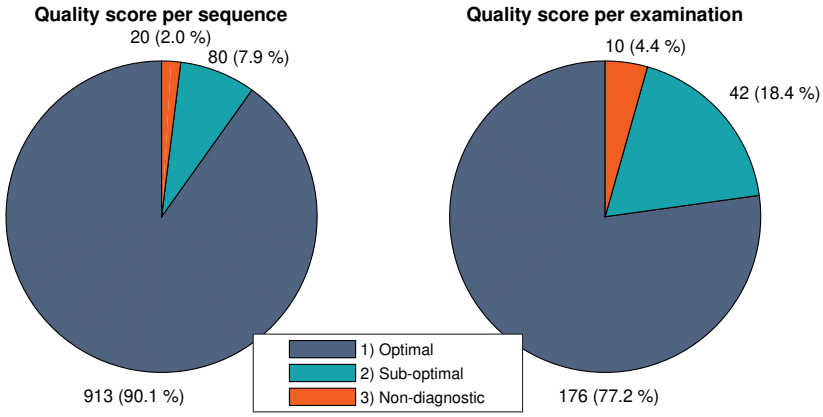

Figure 4.1: Review of 228 MRI examinations acquired in a dementia and a pediatric protocol. Left: Review of 1013 sequences, where each sequence is classified into one of three classes. Right: Distribution of 228 MRI examinations classified into the same three classes based on the sequence with the lowest quality. Adapted from Slipsager *et al.* [12].

4.1.2 Motion-Induced Cost

The motion-induced cost was estimated in four separate cost categories (described above in Section 3.3.3), and the results are presented in Table 4.1 together with the assumptions used. The annual cost to the department or hospital is given as the sum of cost categories (1), (2), and (4) and was estimated to $364,242 per scanner. Using the lower and upper bound assumption resulted in $150,101 and $785,795 per scanner per year, respectively. The sum of categories (1-4) is the total cost to society: $372,492 per scanner per year, where lower and upper bound values are $154,325 and $800,051 per scanner per year.

4.1.3 Savings When Implementing Motion Correction

Based on the estimated costs, Eq. (3.7) was used to calculate the repayment period when employing a MC solution in a clinical workflow. The estimated repayment period is shown as a function of implementation cost and correction performance in Fig. 4.2. The top row in the figure shows the repayment period for a MC solution for adult scans only. Here, it is seen that a MC solution with a total implementation cost of $100,000 would be financially viable after 5 years if the solution achieves a correction performance of at least 45% (16% for upper bound). The same solution would be financially viable after 12 years if the model used the conservative lower bound assumptions. Including the cost estimates of pediatric scans with anesthesia (cost category 3), the above MC solution would be repaid after 1.5 years (row 2, column 1).

4.2 Study II

Study II evaluated the compatibility of the markerless tracking system (TCL2) within a clinical PET/MRI environment. Furthermore, study II demonstrated PMC with markerless motion tracking during in vivo experiments.

4.2.1 Compatibility of TCL Within a Clinical PET/MRI Environment

The TCL2 motion tracker has been installed and used to track motion with a hybrid PET/MRI scanner during normal clinical routines. In a period of more

Table 4.1: Results of the costs estimated in categories (1–4). From Slipsager *et al.* [12].

	Model result	Lower bound	Upper bound
Cost category (1): Repeated sequences			
Number of examinations per year	2000	1600	2400
Number of sequences per examination	5	4	6
The fraction of repeated sequences	2.0%	2.0%	5.5%
Added time per rescan	5 min.	4 min.	6 min.
Examination cost per hour	$555	$444	$666
The extra costs to the clinic per scanner per year	$9,250	$3,789	$52,747
Cost category (2): Repeated examinations			
Number of examinations per year	2000	1600	2400
The fraction of repeated examinations	4.4%	3.5%	5.3%
Added work time to a radiologist	20 min.	16 min.	24 min.
The hourly fee to a radiologist	$111	$89	$133
Examination cost per hour	$555	$444	$666
Duration of new examination	40 min.	32 min.	48 min.
Additional cost to the clinic per scanner per year	$35,816	$14,670	$74,268
Cost category (3): Lost work from the patients			
Number of examinations per year	2000	1600	2400
The fraction of patients in work	25%	20%	30%
Lost working time per examination	30 min.	30 min.	30 min.
Hourly working value	$33	$26	$40
The extra costs to the society per scanner per year	$8,250	$4,224	$14,256
Cost category (4): Anesthesia			
Number of examinations per year	2000	1600	2400
Fraction of pediatric examination	10%	8%	12%
Fraction of examinations using anesthesia	36%	29%	43%
Cost of MRI examination with anesthesia	$4,433	$3,546	$5,320
The extra costs to the clinic per scanner per year	$319,176	$131,642	$658,779
Cost categories combined			
Cost category (1) + (2)	$45,066	$18,459	$127,015
Cost category (1) + (2) + (3)	$53,316	$22,683	$141,271
Cost category (1) + (2) + (4)	$364,242	$150,101	$785,795
Cost category (1) + (2) + (3) + (4)	$372,492	$154,325	$800,051

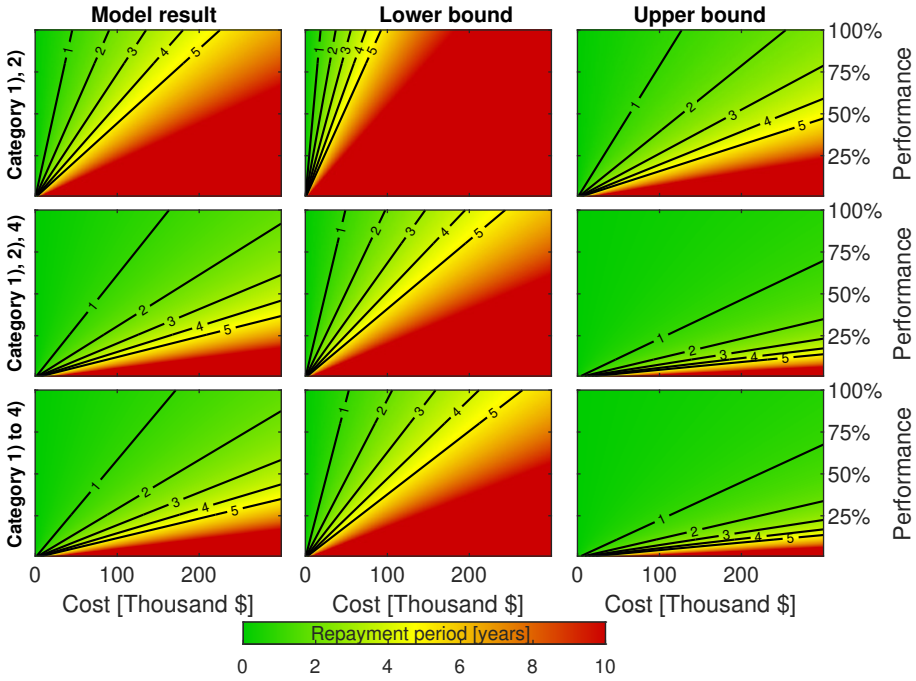

Figure 4.2: Repayment period as a function of the price for implementing MC and the performance of the implemented MC solution. Each line indicates an iso-repayment level in years. Top row: Repayment periods based on costs from an adult population only (the sum of cost categories (1) and (2)). Middle row: Repayment periods based on costs from a mixed population with 10% pediatric patients (the sum of cost categories (1), (2), and (4)). Bottom row: Repayment periods based on costs from a mixed population with 10% pediatric patients and the cost of lost earnings to the society (the sum of cost categories (1–4)). From Slipsager et al. [12].

than two and a half years, the TCL2 system was operated by unsupervised radiographers for the majority of the performed examinations. The radiographers reported no problems related to interference and compatibility between the scanner and the TCL2 system during this period. During the study, the TCL2 system captured motion estimates for all 94 patients. In 88 (93.6%) of the performed examinations, the TCL system recorded motion parameters with high tracking confidence, and no estimates were rejected. Five of the remaining six examinations contain approximately 0.1% rejected tracking estimates due to low point cloud quality occurring during rapid motion. The remaining examination contains almost 15% rejected estimates. A closer inspection revealed that the large proportion of rejections was caused by a reference point cloud containing very little of the patient's face.

Head translations from one of the examined pediatric patients recorded during the PET/MRI examination are shown in Fig. 4.3a. A magnification of the z-translations in the highlighted area is shown in Fig. 4.3b. The periodic oscillations observed in the magnified graph corresponds to the patient's respiratory motion. In this particular case, the patient has a respiration frequency of 18 breaths per minute, which is within the normal range for children. The detection of respiratory motion demonstrates that the TCL2 system has a sufficient sensitivity to estimate motion substantially smaller than the general resolution used in clinical MRI.

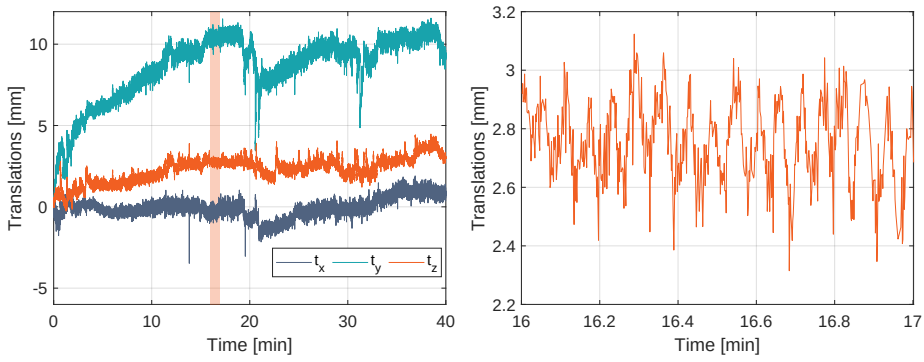

(a) Patient motion **(b)** Patient motion magnified

Figure 4.3: Recorded head translations defined in the scanner's coordinate system of one of the patients in the examined pediatric PET/MRI protocol. The graph in (b) shows a magnification of the translations along the z-direction equal to the highlighted area in (a). The periodic oscillations are the respiratory motion performed by the patient. Adapted from Slipsager *et al.* [30]

4.2.2 PMC Using Markerless Motion Tracking

PMC with markerless tracking was demonstrated in two in vivo experiments using a modified 3D-encoded FLASH sequence. The acquired images of subjects 1 and 2 are shown in Fig. 4.4, and the corresponding motion parameters are shown in study II [30] in Fig. 6. It is seen that the image quality is substantially improved after PMC compared to the images corrupted by similar motion but without PMC. In the case of moderate motion amplitude (subject 1), some motion-related artifacts are still present after PMC. However, in the case of high motion amplitude (subject 2), the image is still notably motion corrupted after PMC. Comparing the images acquired without intentional motion with and without PMC for both subjects show that the image quality is maintained after PMC in case of minimal motion.

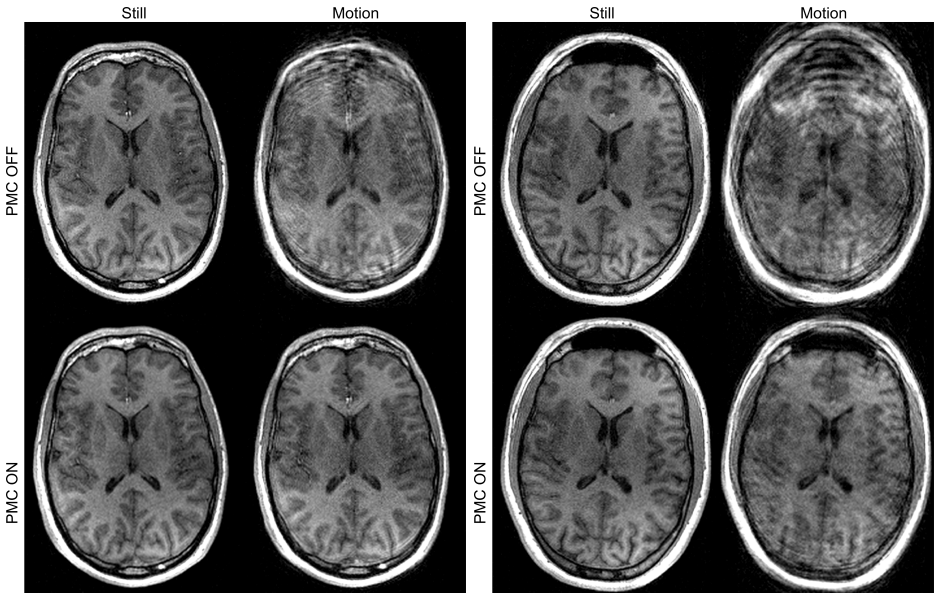

(a) Subject 1 - Moderate motion **(b)** Subject 2 - High Motion

Figure 4.4: In vivo 3D-encoded FLASH scans of two healthy volunteers (Subject 1 and 2). Four scans were acquired for each subject - two still scans with and without PMC and two scans with subject motion with and without PMC. Adapted from Slipsager *et al.* [30]

4.3 Study III

This study qualitatively and quantitatively compared the correction performance of PMC and RMC. The study also investigated the effect of the correction frequency of the encoding error and the performance of RMC.

4.3.1 Comparison of PMC and RMC

Images without MC, with RMC, and with PMC were reconstructed as described in Section 3.5. The image quality comparisons performed in scan sessions 1 and 2 are shown in Fig. 4.5 and 4.6 respectively. The recorded motion parameters from the scans with large motion amplitudes defined in the scanner's coordinate system are shown in Fig. 4.7. It is seen that both PMC and RMC provide improved image quality compared to the uncorrected scans. In the case of the discrete motion with medium motion amplitude (Fig. 4.5), a visual comparison revealed that the PMC image is marginally better than the image corrected by RMC which is more blurred and has less contrast. In the case of large discrete motion, there is a substantial difference in the image quality of the two methods where the RMC image is noticeably more blurred compared to the PMC image. The periodic continuous motion experiment (Fig. 4.6) shows similar results to the discrete experiment where both MC methods lead to improved image quality. As for discrete motion, more artifacts are evident in the RMC images than in the PMC images. The motion parameters recorded during the scans (Fig. 4.7) show that the two volunteers were able to reproduce similar motion patterns in nearly all scans. However, in the case of large discrete motion (subject 1), the volunteer performed less motion during the PMC scans than in the uncorrected scans used for RMC.

Figure 4.8 shows the magnitude values of k-space data from a single receiver channel after no MC, RMC, and PMC during high amplitude discrete motion. The consequence of retrospectively updating k-space trajectories is seen from the center image which contains under- and over-sampled regions. This effect was also observed from the periodic continuous motion patterns, but it was less noticeable than with discrete motion.

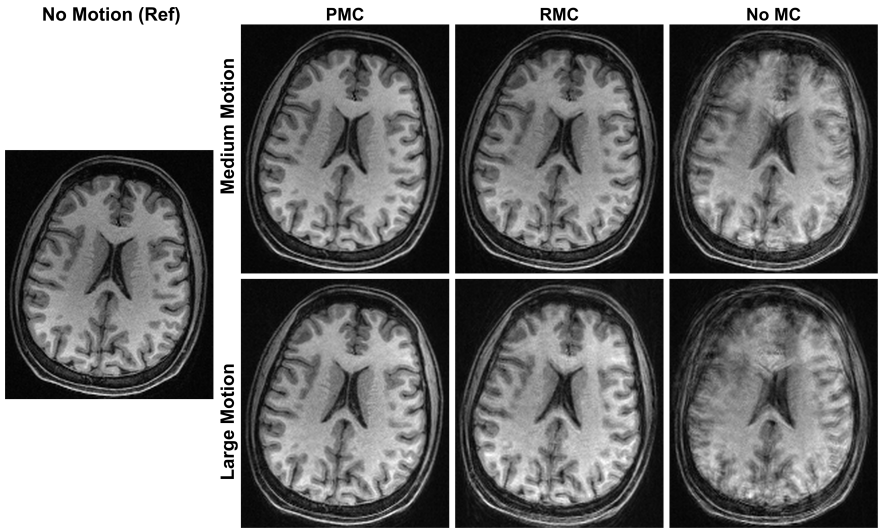

Figure 4.5: In vivo comparison of Within-ET-PMC, Within-ET-RMC, and without MC during scans with discrete motion with medium and large amplitude (Subject 1). The leftmost MPRAGE image was acquired in a scan with no motion and without motion correction and was used as a reference for image quality. Adapted from Slipsager *et al.* [32]

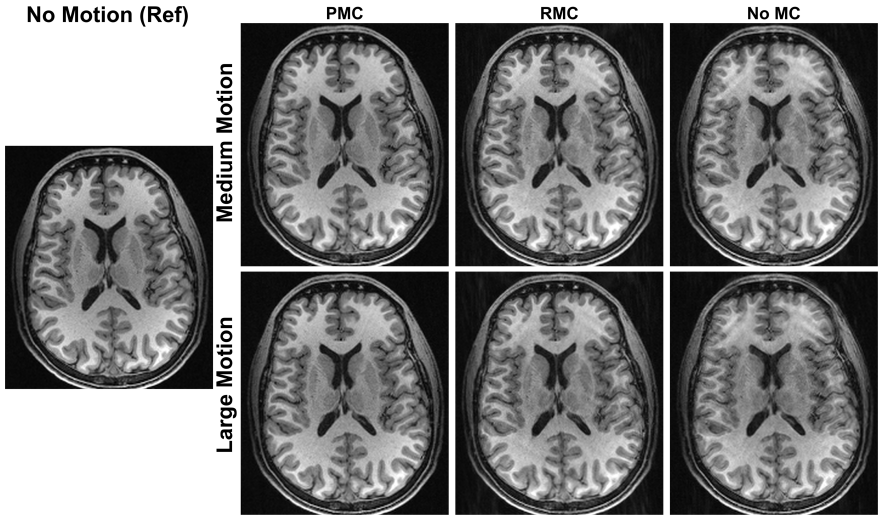

Figure 4.6: In vivo comparison of Within-ET PMC, Within-ET RMC, and no MC during periodic continuous motion with medium and large amplitude (Subject 2). The leftmost MPRAGE image was acquired in a scan with no motion and without motion correction and was used as a reference for image quality. Adapted from Slipsager *et al.* [32]

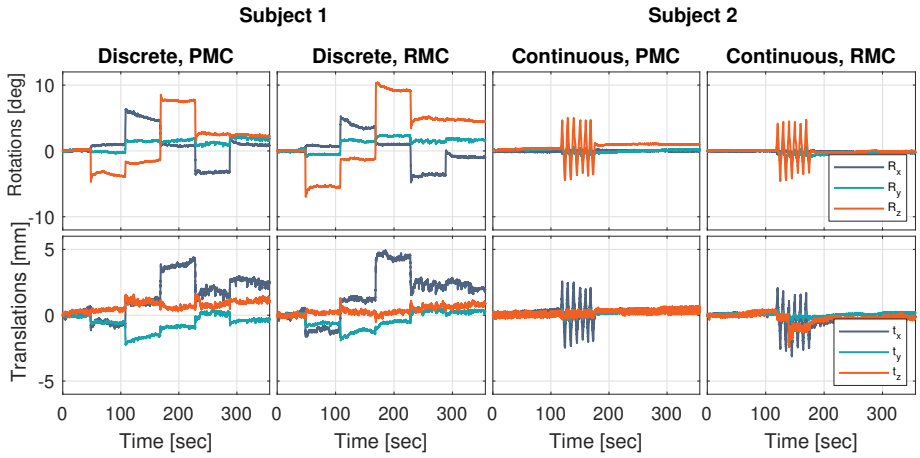

Figure 4.7: Recorded motion parameters during the two experiments with large motion amplitude of subjects 1 and 2. The motion data is defined in the scanner's coordinate system. Adapted from Slipsager *et al.* [32]

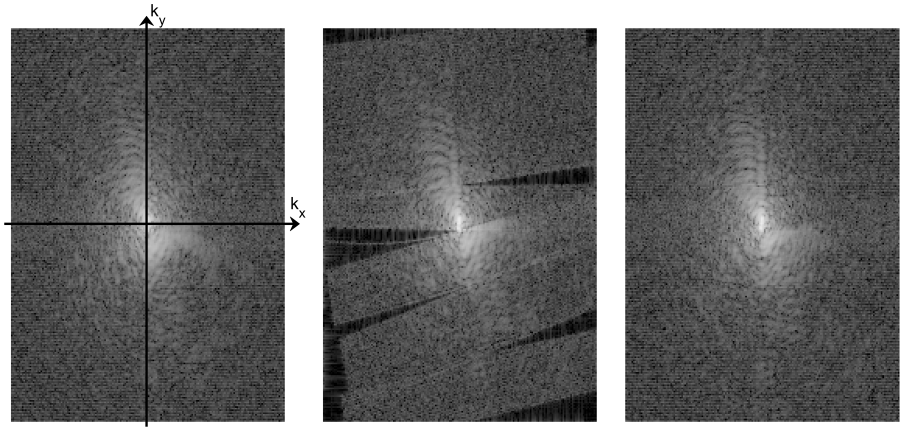

(a) MC Off **(b)** RMC **(c)** PMC

Figure 4.8: The magnitude of the k-space with MC Off, RMC, and PMC. The k-space data were acquired during discrete motion (subject 1) with large amplitude. The k-space data are from a single receiver channel, and the logarithm was applied for better visualization. Adapted from Slipsager *et al.* [32]

The quantitative evaluation of the image quality is shown in Fig. 4.9 where the SSIM of the reconstructed images is plotted as a function of the RMS discrepancy of the recorded motion. It is seen that both PMC and RMC lead to higher SSIM compared to the uncorrected images and that PMC results in the highest SSIM. However, in the scan with large continuous motion, RMC resulted in a marginally lower SSIM compared to the uncorrected image, despite a visual improvement of the image quality (see Fig. 4.6, bottom row). It is also seen that image quality reduces when the motion is increased in nearly every case, both with and without correction. However, the image quality of PMC decreases less compared to no MC and RMC.

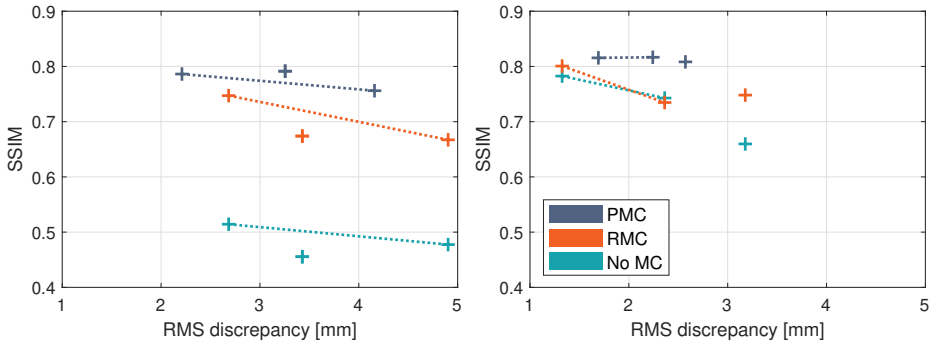

(a) Discrete motion **(b)** Continuous motion

Figure 4.9: Quantitative comparison of the correction performance of Within-ET PMC and Within-ET RMC during discrete and continuous motion. The SSIM relative to an uncorrected scan without intentional motion is plotted as a function of RMS discrepancy between the recorded motion and no motion (identity matrix). Connected points correspond to experiments with the same motion correction but with varied amplitude of motion. Adapted from Slipsager *et al.* [32]

4.3.2 Effect of FOV correction frequency on image quality

The recorded motion estimates and images from the phantom experiments with motion onset at 2 minutes into the sequence are shown in Fig. 4.10. Images along the diagonal were acquired with PMC off, Before-ET PMC, and Within-ET PMC and reconstructed without RMC. Images outside the diagonal are retrospectively corrected or reverse corrected versions of the images in the diagonal. This reconstruction and correction scheme resulted in three images for each acquired scan. It is seen that both retrospective and prospective correction before each ET increase the image quality (column 2, rows 1 and 2). The image quality is further improved after increasing the MC update rate to Within-ET,

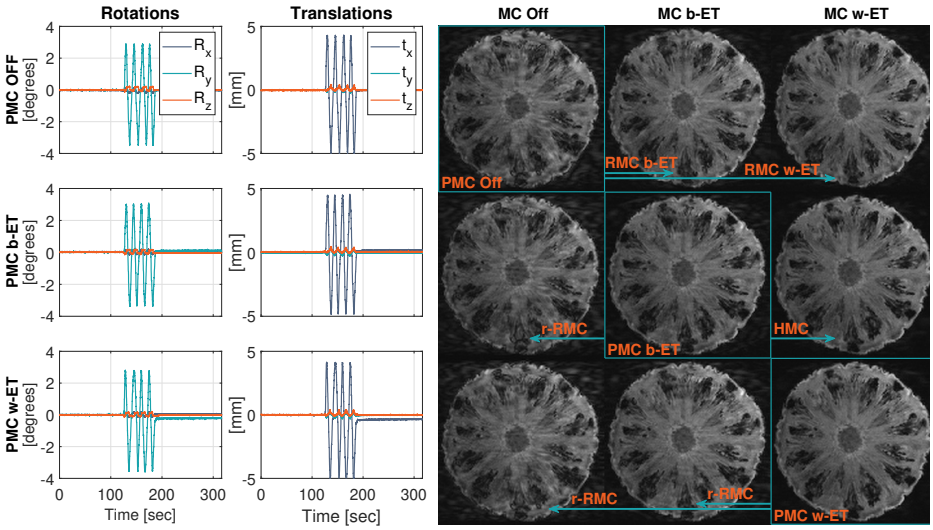

(a) Motion during the scans **(b)** MPRAGE images of the Phantom

Figure 4.10: Phantom comparison of MC OFF, PMC and RMC during periodic continuous motion. (a) Recorded motion parameters of the performed motion with start time 2 minutes into the sequence. (b) MPRAGE images along the diagonal show increasing image quality and were acquired with PMC off, Before echo train PMC (PMC b-ET), and Within echo train PMC (PMC w-ET). Images outside the diagonal are retrospectively corrected or reverse corrected versions of the highlighted image along the same row (indicated by the arrows). These images include RMC, reverse RMC (r-RMC) and HMC. From Slipsager *et al.* [32]

as seen from rows 1 and 3 in column 3. Retrospectively increasing the update rate of data acquired with Before-ET PMC to Within-ET updates through HMC resulted in similar quality to the native Within-ET PMC scan (column 3, rows 2 and 3). The results of reverse correction are shown in column 1, where the first row is the image acquired without PMC. It is seen that reverse RMC can undo the effects of PMC and generate an image with artifacts similar to the image without PMC.

The in vivo scans of subject 2 performing periodic continuous motion were reconstructed with the same correction scheme as for the phantom experiments. Motion parameters and images for the high motion amplitude experiments are shown in Fig. 4.11a and 4.11b, respectively. Generally, similar results were seen in the in vivo experiments, where Within-ET correction leads to images with the highest quality. However, PMC provided images with visual better quality compared to RMC, while the quality of HMC is between PMC and

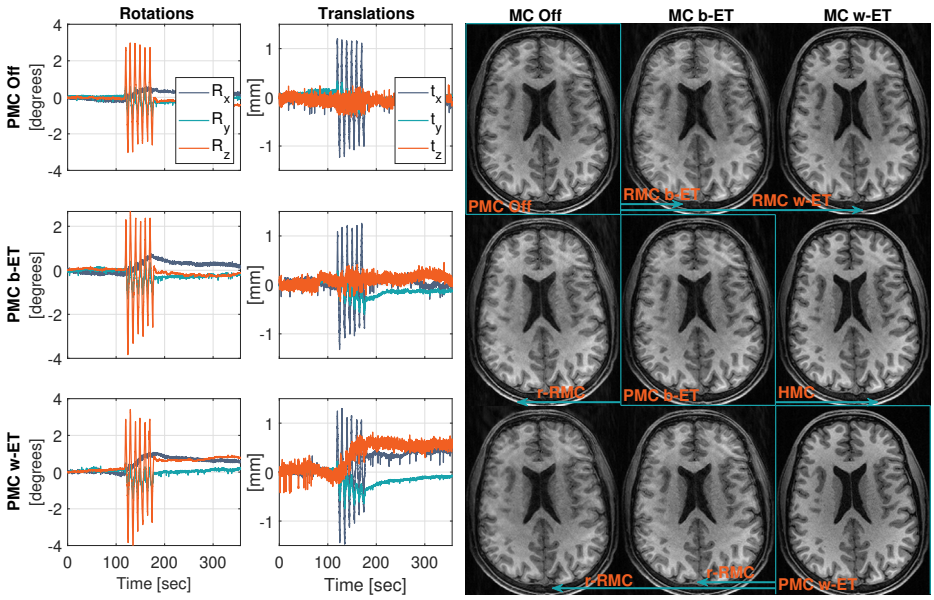

(a) Motion during the scans **(b)** MPRAGE images of subject 2

Figure 4.11: In vivo comparison of MC OFF, PMC, and RMC during periodic continuous motion (large amplitude, subject 2. (a) Recorded motion parameters of the performed motion. (b) The MPRAGE images along the diagonal were acquired with PMC off, Before echo train PMC (PMC b-ET), and Within echo train PMC (PMC w-ET). Images outside the diagonal are retrospectively corrected or reverse corrected versions of the highlighted image along the same row (indicated by the arrows). These images include RMC, reverse RMC (r-RMC), and HMC. From Slipsager *et al.* [32]

RMC. Another difference from the phantom experiments is that the Before-ET correction with PMC and RMC does not improve the image quality compared to the uncorrected image.

The RMS discrepancy between the true motion and the encoded motion was used as a quantitative measure of the encoding error of the correction. In Fig. 4.12 the SSIM is plotted as a function of the RMS discrepancy for all images (both phantom and in vivo) reconstructed with the same correction scheme as used in Fig. 4.10b and 4.11b. k-Space data acquired with PMC off, Before-ET PMC, and Within-ET PMC are labeled with blue markers. Images reconstructed from the same k-space data are connected, and data points with the same color were corrupted by similar motion patterns and amplitudes. From Fig. 4.12a showing the phantom experiments, it is seen that Within-ET MC leads to the best quality images, while Before-ET MC resulted in lower quality

images. It is also seen that images reconstructed with reverse RMC (most right circles) have similar SSIM to the images acquired without PMC. The same general tendencies are seen in the in vivo experiments (Fig. 4.12b). However, in the scan with high motion amplitude, Before-ET RMC caused and reduction of the image quality.

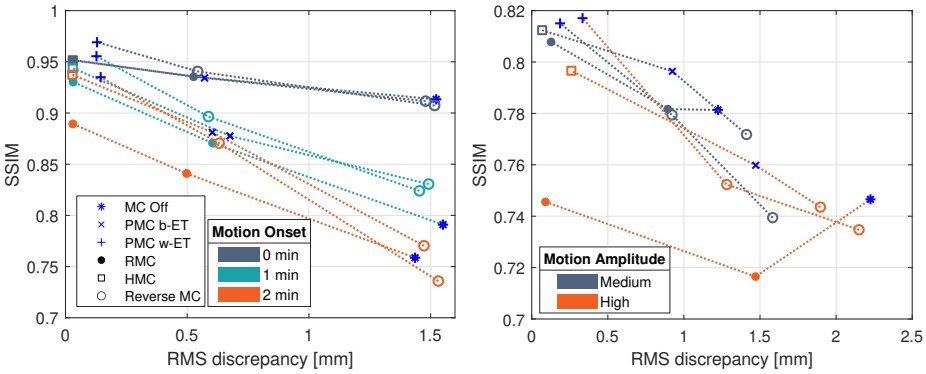

(a) Phantom **(b)** In vivo

Figure 4.12: SSIM as a function of RMS discrepancy between true motion and encoded motion. Blue markers correspond to data acquired with PMC off, before echo train (b-ET) PMC, and within echo train (w-ET) PMC. Connected points represent images reconstructed from the same data. The color corresponds to a given type of motion. In the phantom scans (a) the colors correspond to the motion starting 0, 1, and 2 minutes into the sequences. In the in vivo scans (b) the colors correspond to the medium and high motion amplitude experiments. Both figures show that increasing the correction frequency from Before-ET to Within-ET results in lower RMS-discrepancy and higher image quality. Adapted from Slipsager *et al.* [32]

Chapter 5

Discussion

This industrial Ph.D. thesis aimed to provide better image quality of motion corrupted MRI images by improving MC. Subject motion during MRI scans lead to images corrupted by motion artifacts such as ghosting, ringing, and blurring. Low-quality MRI images make the image interpretation more challenging for radiologists and researchers and can potentially lead to incorrect diagnosis or introduce variance and bias in research results [18, 58]. Repeating images that have artifacts and anesthesia are commonly used to obtain images with the necessary quality. However, both of these methods increase the cost of the MRI examination [8, 12] and anesthesia is associated with increased health risk [11].

To improve the image quality of neuroanatomical MRI images, we introduced PMC and RMC using motion information of the head estimated with markerless tracking. We have shown that both RMC and PMC resulted in a substantial improvement in the quality of structural MRI images of the brain. In vivo comparisons of RMC and PMC show superior correction performance of PMC during scans corrupted by reproduced motion. The inferiority of RMC is due to Nyquist violations and irregular sampling of the k-space, which are side effects of retrospective correction. To accommodate some of the main disadvantages of PMC, we demonstrated combined prospective and retrospective correction both for correction and for "reverse" correction. We showed that k-space data acquired with PMC can be reverse corrected to estimate what the uncorrected image would have looked like, because this image is not preserved by PMC in

its native configuration. The possibility of estimating the uncorrected images simplifies the validation of PMC especially in clinical settings where scans with and without PMC corrupted by the same motion pattern are not possible to acquire. Retrospectively increasing the correction frequency of k-space data acquired with Before-ET PMC was successfully demonstrated, and a notable improvement in the image quality was observed.

When this Ph.D. project began, MC had been successfully demonstrated in several studies since the late 1980s [37, 45]. However, today, only two commercial MC solutions [16, 42] are available for clinical use despite the large cost of unintended patient motion during MRI examinations [8, 12]. Furthermore, these MC solutions are limited to certain pulse sequences, scanner vendors, and types of motion.

Of the proposed methods, two main MC categories exist; PMC and RMC. Both categories have been demonstrated using a variety of different motion tracking strategies. Motion correction using tracking data acquired with MRI navigators [16, 20, 38, 59, 60] requires no additional hardware and no patient interaction. The minimal patient interaction of these methods fits a clinical workflow well. However, the temporal resolution of navigator tracking limits the correction frequency of MC, which has a substantial impact on the image quality during fast motion [29, 32]. External motion tracking systems [25, 26, 61] offer a much higher temporal resolution compared to navigators, and correction frequency is thus not limited by these motion estimation methods. A disadvantage for the majority of the suggested external tracking methods is that they require patient interaction in the form of attaching markers to the patient's face, which adds to time the clinical routine. Maclaren et al. [14] pointed out in a review article from 2013 that "markerless" motion tracking would be the ideal solution from a patient handling perspective, but the accuracy and speed of the tracking were not sufficient for MC yet.

Like the proposed tracking methods, PMC and RMC have advantages and disadvantages too. Prospective motion correction has been demonstrated in several studies [23, 62, 63] using tracking data acquired with navigators and external tracking systems. Nael et al. [64] evaluated in a recent study the correction performance of PMC using optical tracking on 100 patients during clinical brain MRI examinations. They found that PMC significantly reduced the number of nondiagnostic sequences from 19.5% to 5.7%. The main drawback of PMC is that it does not preserve the original uncorrected image, which makes clinical evaluation of PMC challenging. Not having the original image is also a problem in situations where inaccurate tracking is provided, and the PMC introduces artifacts that would not have been present in the uncorrected image. Maclaren et al. [65], and Zahneisen et al. [40] both proposed solutions to this problem where RMC is used to reverse correct the effect of PMC to either generate the

uncorrected image with PMC disabled or to decorrecting artifacts caused by tracking errors.

RMC has also been demonstrated in several studies showing substantial reduction of motion related artifacts [60, 66]. Glessgen et al. [67] evaluated RMC using navigators on 40 patients undergoing a clinical brain tumor MRI protocol and reported that RMC caused a significant improvement of the image quality. The main disadvantage of RMC compared to PMC is that RMC is expected to have a lower correction performance mainly due to Nyquist violations and irregular sampling of the k-space as a side effect of retrospectively updating the k-space trajectories [14]. However, to our knowledge, this difference in correction performance has never been directly compared.

Unintended patient motion is a common problem, and it adds significant expenses to the hospital. Andre et al. [8] reported that the annual cost of patient motion due to repeated sequences is approximately $115,000 per scanner. Our estimation of the motion-induced cost (Table 4.1) caused by repeated sequences and examinations shows comparable results. However, our estimates resulted in lower costs as the number of annual performed MRI examination was assumed to 2000 per scanner compared to 3588 in [8]. Our cost estimates also include the expenses of using anesthesia in pediatric MRI examinations which were not included in the study by Andre et al. Here, we estimated that the expense of anesthesia is approximately $319,000 on a scanner where 10% of examinations are pediatric.

A lot of work has been devoted to developing new and better MC solutions, although the potential financial benefits of MC have not been thoroughly investigated. Hence, we designed a model to analyze the potential financial benefits of employing MC based on our cost estimates. We found that a MC solution with an implementation cost of $100,000 and capable of correcting 45% of the corrupted sequences is financially viable after 5 years if only an adult population is included. If 10% of scans are pediatric examinations, the same MC solution is financially viable after $\sim$1.5 years. This suggests that MC in many cases is a financially beneficial solution, assuming successful correction in 45% of cases. However, our model does not include any additional preparation time to set up the MC system, which has a negative effect on the cost savings.

Our objective was to mature MC to make it more ready for clinical use. Hence, we introduced PMC and RMC using head motion data recorded with a markerless tracking device. Like motion tracking with MRI navigators, markerless tracking requires no patient interaction and thereby minimizes the initialization time of MC compared to markers-based optical tracking systems. However, the current version of TCL still requires some additional time for the scanner operators to set up the system prior to an examination. Markerless tracking

also benefits from being an external system, meaning that the head motion is estimated with a high temporal resolution independently from the scanner. Our experiments of healthy volunteers show that PMC and RMC with markerless tracking produces images with comparable quality to the previous proposed MC solutions. It is challenging to judge the performance of different MC setups without direct comparisons, mainly due to variation in the tested motion.

The motion correction capabilities of PMC is expected to be superior to the capabilities of RMC due to Nyquist violations caused by the RMC method [14]. However, RMC is more robust to tracking noise, and RMC preserves the original uncorrected image. RMC also allow better post-processing of motion data, e.g., filtering. Hence RMC may is a more viable solution in clinical applications despite the expected inferior correction performance. Therefore, we performed direct performance comparisons of RMC and PMC using motion data from the same markerless tracking system. The comparison showed that PMC leads to superior quality images, and the difference in image quality increases with the amplitude of the motion. This dependency between performance and motion amplitude also indicates that the performance of RMC and PMC would be more similar in cases of reduced motion. To our knowledge, PMC and RMC have not been compared in previous studies. Visual assessment of the results in Zahneisen et al. 2016 [40] shows similar performance of PMC and RMC during discrete and periodic continuous motion patterns. However, there was substantial variation in motion amplitude between the PMC and RMC scans. Our comparisons were conducted on 3D-encoded sequences, where RMC is not limited by through slice motion as it is for 2D-encoded sequences. If we have evaluated RMC and PMC on 2D-encoded sequences we had probably observed more considerable performance differences between the two methods.

We combined PMC and RMC to accommodate some of the limitations of both methods. This hybrid correction approach uses Before-ET PMC to roughly correct the data and RMC to fine tune the correction. Our performed experiments showed that the performance of HMC is superior to RMC, but the quality of standalone PMC is still marginally better. However, the hybrid approach is a potential solution to the tracking noise of standalone PMC if the Before-ET PMC scan is more robust to tracking noise than Within-ET PMC. Combined PMC and RMC have been demonstrated in previous studies [40, 65] to remove artifacts caused by noisy tracking during the prospective correction. But instead of using RMC for fine tuning, RMC was used to reverse correct artifacts caused by the tracking noise in the data acquired with PMC.

Applying reverse MC to estimate the uncorrected image is another synergy of combined PMC and RMC. Here, RMC is used to "undo" the correction of PMC by respectively applying the inverse of transformations used to update the FOV during PMC. Our experiments showed that reverse MC was able to estimate

an uncorrected image with artifacts similar to the image from the scan without PMC. Having the possibility to generate the uncorrected image simplifies the evaluation process of PMC since it is not possible to acquire sets of scans with and without PMC corrupted by the same motion. However, reverse MC is based on RMC. Thus it is limited to 3D sequences, and it has the same issues with k-space irregularities and Nyquist violations as RMC.

In study I, we found that 2.0% of the reviewed MRI images were corrupted by motion to a degree where the images could no longer be used for clinical purposes. Further, we found that 4.4% of the MRI brain examinations had nonusable sequences. Our two selected protocols are considered particularly prone to motion; however, Andre et al. [8] reported in another study that 19.8% of the exams contained repeated sequences. Our suggested cost analysis indicated that a MC solution with a correction performance of 50% should have a maximal implementation cost of $47,000 using the most conservative model for the adult population before it is financially viable within five years (Fig. 4.2). Including 10% pediatric examinations in the same solution, the maximal implementation cost is $132.500. A limitation of our conducted cost analysis is that it was performed as a model-based estimate with assumptions, meaning that no prospective studies were made to estimate the cost savings of MC. This implies uncertainty in the estimated cost and repayment periods. Therefore, we conducted the analysis with 20% lower and upper bounds to include the uncertainty in the model.

In study II, we examined the compatibility of the markerless tracking system (TCL) within a clinical PET/MRI environment. No interference between the motion tracker and the scanner was observed, and the scanner operators were able to operate the TCL system autonomously in the majority of the performed examinations. Our review of the generated point clouds showed that 88 out of 94 examinations contained no rejected point clouds. One of the remaining six examinations contains 15% rejected point clouds due to a poorly selected reference point cloud by the operator. We tried to select a new reference point cloud and then run the tracking algorithm retrospectively on the prerecorded point clouds. The re-tracking with the new reference reduces the amount of rejected point clouds to 4%, showing that the tracking system is sensitive to the selected reference point cloud. Automation of the reference point cloud selection may increase the overall robustness of the motion tracker. Although we saw that the TCL system was capable of capturing respiratory motion (See Fig. 4.3), the motion estimates were not used for MC. Hence it was difficult to evaluate the accuracy of the tracking in a clinical setting.

In Study II, we also demonstrated PMC with markerless tracking of two healthy volunteers. Visual assessment of the acquired images showed that the image quality of PMC images was maintained in scans without intended motion while

the image quality was improved in the scans with intended motion (Fig. 4.4). Despite the overall improvement of the image quality, motion artifacts are still present in the corrected images. The remaining artifacts are likely in part the result of B0-field inhomogeneities induced by the extreme head motion and can not be corrected by updating the FOV alone. Additional artifacts may also have been induced by the motion of the subject relative to the B0 receive fields of the coil elements, which is not accounted for in the PMC sequence we have used.

The performed motion patterns in studies II and III are not realistic, and it is unlikely that any clinical scanned patient would perform similar motion patterns. However, our selected motion patterns are reproducible for the volunteers between the separate scans, and the selected patterns are typically used to test MRI MC.

Chapter 6

Conclusion

Motion correction is an instrumental step to acquiring high-quality structural MRI images in case of unintended patient motion. Involuntary head motion is a major concern in both clinical and research MRI as it causes low-quality images. We estimated that the annual expenses of head motion due to the cost of anesthesia, repeated sequences, and entire examinations were ∼$372,492 per scanner. Based on the estimated cost, we designed a model to calculate the repayment periods of MC solutions as functions of the correction performance and implementation cost. Our most conservative model showed that a MC solution with a performance of 50% would be financially viable after five years if its implementation cost is kept below $47,000.

Today, several MC solutions have been proposed in the literature, showing impressive results. However, only a fraction of the MC methods are commercially available today, and these methods are limited to certain pulse sequences and scanner vendors. In this thesis, we propose MC with markerless tracking. Markerless tracking has the benefit of MRI navigators of not requiring patient interaction, and it has the benefits of being an external motion tracking (high temporal resolution and sequences/scanner independent). We evaluated the compatibility of the markerless motion tracking TCL in a clinical PET/MRI environment. No interference between the TCL and the scanner was found, and the TCL system could be operated autonomously by the scanner staff in the majority of the performed examinations.

We demonstrated PMC, RMC, and combined PMC and RMC (HMC), all with markerless tracking. All three correction methods result in substantial improvement of the image quality. However, a direct comparison shows that the image quality of PMC is superior.

Motion correction with markerless tracking is a promising solution to move into the clinical workflow. However, there are still challenges that need to be addressed. Our proposed markerless MC solution currently requires some manual steps to perform MC, which adds additional steps to the examination protocol. Although we have shown that PMC is the best performing of our three tested methods, PMC is sensitive to noise and inaccurate tracking. On the other hand, our suggested markerless RMC solution can be implemented completely independent from the clinical protocol. Hence, RMC may be the more pragmatic solution for clinical application at present.

Bibliography

[1] W. R. Hendee, G. J. Becker, J. P. Borgstede, J. Bosma, W. J. Casarella, B. A. Erickson, C. D. Maynard, J. H. Thrall, and P. E. Wallner, "Addressing overutilization in medical imaging," *Radiology*, vol. 257, no. 1, pp. 240–245, 2010.

[2] J. M. Slipsager, K. A. Juhl, P. E. Sigvardsen, K. F. Kofoed, O. De Backer, A. L. Olivares, O. Camara, and R. R. Paulsen, "Statistical Shape Clustering of Left Atrial Appendages," in *International Workshop on Statistical Atlases and Computational Models of the Heart*, vol. 11395. Springer International Publishing, 2018, pp. 32–39.

[3] T. Geva, "Magnetic resonance imaging: Historical perspective," *Journal of Cardiovascular Magnetic Resonance*, vol. 8, no. 4, pp. 573–580, 2006.

[4] F. Barkhof, S. Haller, and S. A. Rombouts, "Resting-state functional MR imaging: A new window to the brain," *Radiology*, vol. 272, no. 1, pp. 29–49, 2014.

[5] J. Kurhanewicz, D. B. Vigneron, J. H. Ardenkjaer-Larsen, J. A. Bankson, K. Brindle, C. H. Cunningham, F. A. Gallagher, K. R. Keshari, A. Kjaer, C. Laustsen, D. A. Mankoff, M. E. Merritt, S. J. Nelson, J. M. Pauly, P. Lee, S. Ronen, D. J. Tyler, S. S. Rajan, D. M. Spielman, L. Wald, X. Zhang, C. R. Malloy, and R. Rizi, "Hyperpolarized 13C MRI: Path to Clinical Translation in Oncology," *Neoplasia (United States)*, vol. 21, no. 1, pp. 1–16, 2019.

[6] V. P. Grover, J. M. Tognarelli, M. M. Crossey, I. J. Cox, S. D. Taylor-Robinson, and M. J. McPhail, "Magnetic Resonance Imaging: Principles

and Techniques: Lessons for Clinicians," *Journal of Clinical and Experimental Hepatology*, vol. 5, no. 3, pp. 246–255, 2015.

[7] M. Zaitsev, J. Maclaren, and M. Herbst, "Motion artifacts in MRI: A complex problem with many partial solutions," *Journal of Magnetic Resonance Imaging*, vol. 42, no. 4, pp. 887–901, jan 2015.

[8] J. B. Andre, B. W. Bresnahan, M. Mossa-Basha, M. N. Hoff, C. Patrick Smith, Y. Anzai, and W. A. Cohen, "Toward quantifying the prevalence, severity, and cost associated with patient motion during clinical MR examinations," *Journal of the American College of Radiology*, vol. 12, no. 7, pp. 689–695, 2015.

[9] S. A. Vanderby, P. S. Babyn, M. W. Carter, S. M. Jewell, and P. D. Mckeever, "Effect of Anesthesia and Sedation on Pediatric MR Imaging Patient Flow," *Radiology*, vol. 256, no. 1, pp. 229–237, 2010.

[10] R. D. Sanders, J. Hassell, A. J. Davidson, N. J. Robertson, and D. Ma, "Impact of anaesthetics and surgery on neurodevelopment: An update," *British Journal of Anaesthesia*, vol. 110, pp. 53–72, 2013.

[11] D. Blumenthal and M. Tavenner, "Anesthesia and Developing Brains — Implications of the FDA Warning," *The New England Journal of Medicine*, vol. 376, no. 10, pp. 905–907, 2017.

[12] J. M. Slipsager, S. L. Glimberg, J. Søgaard, R. R. Paulsen, H. H. Johannesen, P. C. Martens, A. Seth, L. Marner, O. M. Henriksen, O. V. Olesen, and L. Højgaard, "Quantifying the Financial Savings of Motion Correction in Brain MRI : A Model-Based Estimate of the Costs Arising From Patient Head Motion and Potential Savings From Implementation of Motion Correction," *Journal of Magnetic Resonance Imaging*, vol. 52, no. 3, pp. 731–738, 2020.

[13] D. G. Nishimura, *Principles of Magnetic Resonance Imaging*, 1st ed., 2016.

[14] J. Maclaren, M. Herbst, O. Speck, and M. Zaitsev, "Prospective Motion Correction in Brain Imaging: A Review," *Magnetic resonance in medicine*, vol. 69, no. 3, pp. 621–636, 2013.

[15] A. J. W. Van der Kouwe, T. Benner, and A. M. Dale, "Real-time rigid body motion correction and shimming using cloverleaf navigators," *Magnetic resonance in medicine*, vol. 56, no. 5, pp. 1019–1032, 2006.

[16] N. White, C. Roddey, A. Shankaranarayanan, E. Han, D. Rettmann, J. Santos, J. Kuperman, and A. Dale, "PROMO: Real-time prospective motion correction in MRI using image-based tracking," *Magnetic Resonance in Medicine*, vol. 63, no. 1, pp. 91–105, 2010.

[17] M. D. Tisdall, A. T. Hess, M. Reuter, E. M. Meintjes, B. Fischl, and A. J. W. van der Kouwe, "Volumetric navigators for prospective motion correction and selective reacquisition in neuroanatomical MRI," *Magnetic resonance in medicine*, vol. 68, no. 2, pp. 389–399, 2012.

[18] M. D. Tisdall, M. Reuter, A. Qureshi, R. L. Buckner, B. Fischl, and A. J. van der Kouwe, "Prospective motion correction with volumetric navigators (vNavs) reduces the bias and variance in brain morphometry induced by subject motion," *NeuroImage*, vol. 127, pp. 11–22, 2016.

[19] D. Gallichan and J. P. Marques, "Optimizing the acceleration and resolution of three-dimensional fat image navigators for high-resolution motion correction at 7T," *Magnetic Resonance in Medicine*, vol. 77, no. 2, pp. 547–558, 2017.

[20] T. E. Wallace, O. Afacan, M. Waszak, T. Kober, and S. K. Warfield, "Head motion measurement and correction using FID navigators," *Magnetic Resonance in Medicine*, vol. 81, no. 1, pp. 258–274, 2019.

[21] M. B. Ooi, S. Krueger, W. J. Thomas, S. V. Swaminathan, and T. R. Brown, "Prospective Real-Time Correction for Arbitrary Head Motion Using Active Markers," *Magnetic resonance in medicine*, vol. 62, no. 4, pp. 943–954, 2009.

[22] A. Aranovitch, M. Haeberlin, S. Gross, B. E. Dietrich, B. J. Wilm, D. O. Brunner, T. Schmid, R. Luechinger, and K. P. Pruessmann, "Prospective motion correction with NMR markers using only native sequence elements," *Magnetic Resonance in Medicine*, vol. 79, no. 4, pp. 2046–2056, 2018.

[23] A. van Niekerk, A. van der Kouwe, and E. Meintjes, "Toward "plug and play" prospective motion correction for MRI by combining observations of the time varying gradient and static vector fields," *Magnetic Resonance in Medicine*, vol. 82, no. 3, pp. 1214–1228, 2019.

[24] M. Zaitsev, C. Dold, G. Sakas, J. Hennig, and O. Speck, "Magnetic resonance imaging of freely moving objects: prospective real-time motion correction using an external optical motion tracking system," *Neuroimage*, vol. 31, no. 3, pp. 1038–1050, 2006.

[25] J. Schulz, T. Siegert, E. Reimer, C. Labadie, J. Maclaren, M. Herbst, M. Zaitsev, and R. Turner, "An embedded optical tracking system for motion-corrected magnetic resonance imaging at 7T," *Magnetic Resonance Materials in Physics, Biology and Medicine*, vol. 25, no. 6, pp. 443–453, 2012.

[26] M. Aksoy, C. Forman, M. Straka, S. Skare, S. Holdsworth, J. Hornegger, and R. Bammer, "Real-time optical motion correction for diffusion tensor imaging," *Magnetic Resonance in Medicine*, vol. 66, no. 2, pp. 366–378, 2011.

[27] O. V. Olesen, R. R. Paulsen, L. Hojgaard, B. Roed, and R. Larsen, "Motion Tracking for Medical Imaging: A Nonvisible Structured Light Tracking Approach," *IEEE transactions on medical imaging*, vol. 31, no. 1, pp. 79–87, 2012.

[28] O. V. Olesen, J. M. Sullivan, T. Mulnix, R. R. Paulsen, L. Hojgaard, B. Roed, R. E. Carson, E. D. Morris, and R. Larsen, "List-Mode PET Motion Correction Using Markerless Head Tracking: Proof-of-Concept With Acans of Human Subject," *IEEE transactions on medical imaging*, vol. 32, no. 2, pp. 200–209, 2013.

[29] R. Frost, P. Wighton, F. I. Karahanoğlu, R. L. Robertson, P. E. Grant, B. Fischl, M. D. Tisdall, and A. van der Kouwe, "Markerless high-frequency prospective motion correction for neuroanatomical MRI," *Magnetic Resonance in Medicine*, vol. 82, no. 1, pp. 126–144, 2019.

[30] J. M. Slipsager, A. H. Ellegaard, S. L. Glimberg, R. R. Paulsen, M. Dylan Tisdall, P. Wighton, A. Van Der Kouwe, L. Marner, O. M. Henriksen, I. Law, and O. V. Olesen, "Markerless motion tracking and correction for PET, MRI, and simultaneous PET/MRI," *PLoS ONE*, vol. 14, no. 4, pp. 1–17, 2019.

[31] J. Berglund, A. van Niekerk, H. Rydén, T. Sprenger, E. Avventi, O. Norbeck, S. L. Glimberg, O. V. Olesen, and S. Skare, "Prospective motion correction for diffusion weighted EPI of the brain using an optical markerless tracker," *Magnetic Resonance in Medicine*, vol. 85, no. 3, pp. 1427–1440, 2021.

[32] J. M. Slipsager, S. L. Glimberg, L. Højgaard, R. R. Paulsen, P. Wighton, M. D. Tisdall, C. Jaimes, B. A. Gagoski, P. E. Grant, A. van der Kouwe, O. V. Olesen, and R. Frost, "Comparison of prospective and retrospective motion correction in 3D-encoded neuroanatomical MRI," *Accepted for publication in Magnetic Resonance in Medicine*, 2021.

[33] M. K. Stehling, R. Turner, and P. Mansfield, "Echo-planar imaging: Magnetic resonance imaging in a fraction of a second," *Science*, vol. 254, no. 5028, pp. 43–50, 1991.

[34] D. K. Sodickson and W. J. Manning, "Simultaneous acquisition of spatial harmonics (SMASH): Fast imaging with radiofrequency coil arrays," *Magnetic Resonance in Medicine*, vol. 38, no. 4, pp. 591–603, 1997.

[35] M. A. Griswold, P. M. Jakob, R. M. Heidemann, M. Nittka, V. Jellus, J. Wang, B. Kiefer, and A. Haase, "Generalized Autocalibrating Partially Parallel Acquisitions (GRAPPA)," *Magnetic Resonance in Medicine*, vol. 47, no. 6, pp. 1202–1210, 2002.

[36] G. E. Sarty, "Single TrAjectory Radial (STAR) Imaging," *Magnetic Resonance in Medicine*, vol. 51, no. 3, pp. 445–451, 2004.

[37] R. L. Ehman and J. P. Felmlee, "Adaptive technique for high-definition MR imaging of moving structures," *Radiology*, vol. 173, no. 1, pp. 255–263, 1989.

[38] D. Gallichan, J. P. Marques, and R. Gruetter, "Retrospective correction of involuntary microscopic head movement using highly accelerated fat image navigators (3D FatNavs) at 7T," *Magnetic Resonance in Medicine*, vol. 75, no. 3, pp. 1030–1039, 2016.

[39] P. M. Johnson, J. Liu, T. Wade, M. Ali, and M. Drangova, "Retrospective 3D motion correction using spherical navigator echoes," *Magnetic Resonance Imaging*, vol. 34, no. 9, pp. 1274–1282, 2016.

[40] B. Zahneisen, B. Keating, A. Singh, M. Herbst, and T. Ernst, "Reverse retrospective motion correction," *Magnetic Resonance in Medicine*, vol. 75, no. 6, pp. 2341–2349, 2016.

[41] D. Atkinson, D. L. Hill, P. N. Stoyle, P. E. Summers, S. Clare, R. Bowtell, and S. F. Keevil, "Automatic compensation of motion artifacts in MRI," *Magnetic Resonance in Medicine*, vol. 41, no. 1, pp. 163–170, 1999.

[42] J. G. Pipe, "Motion correction with PROPELLER MRI: application to head motion and free-breathing cardiac imaging," *Magnetic Resonance in Medicine*, vol. 42, no. 5, pp. 963–969, 1999.

[43] T. Küstner, K. Armanious, J. Yang, B. Yang, F. Schick, and S. Gatidis, "Retrospective correction of motion - affected MR images using deep learning frameworks," *Magnetic Resonance in Medicine*, vol. 82, no. 4, pp. 1527–1540, 2019.

[44] P. M. Johnson and M. Drangova, "Conditional generative adversarial network for 3D rigid - body motion correction in MRI," *Magnetic Resonance in Medicine*, vol. 82, no. 3, pp. 901–910, 2019.

[45] E. M. Haacke and J. L. Patrick, "Reducing motion artifacts in two-dimensional Fourier transform imaging," *Magnetic Resonance Imaging*, vol. 4, no. 4, pp. 359–376, 1986.

[46] C. C. Lee, C. R. Jack, R. C. Grimm, P. J. Rossman, J. P. Felmlee, R. L. Ehman, and S. J. Riederer, "Real-time adaptive motion correction in functional MRI," *Magnetic Resonance in Medicine*, vol. 36, no. 3, pp. 436–444, 1996.

[47] C. C. Lee, R. C. Grimm, A. Manduca, J. P. Felmlee, R. L. Ehman, S. J. Riederer, and C. R. Jack, "A prospective approach to correct for inter-image head rotation in FMRI," *Magnetic Resonance in Medicine*, vol. 39, no. 2, pp. 234–243, 1998.

[48] N. Priovoulos, M. Andersen, V. O. Boer, and W. van der Zwaag, "Visualizing the cerebellar cortical layers with prospective motion correction," in *29th Annual Meeting of the International Society of Magnetic Resonance in Medicine*, 2021, p. Abstract 0121.

[49] P. Wighton, D. M. Tisdall, H. Bhat, E. Nevo, and A. der Kouwe, "Slice-by-slice prospective motion correction in EPI sequences," in *ISMRM Workshop on Motion Correction in MRI*, 2014.

[50] D. Gallichan, "RetroMoCoBox Toolbox." [Online]. Available: https://github.com/dgallichan/retroMoCoBox

[51] A. Schwarzl and F. Knoll, "Implementation of Non Uniform Fast Fourier Transformation." [Online]. Available: https://github.com/andyschwarzl/gpuNUFFT

[52] Danmarks Statistik, "Average Income in Denmark." [Online]. Available: https://statistikbanken.dk/INDKP105

[53] S. B. Runge, N. L. Christensen, K. Jensen, and I. E. Jensen, "Children centered care: Minimizing the need for anesthesia with a multi-faceted concept for MRI in children aged 4–6," *European Journal of Radiology*, vol. 107, pp. 183–187, 2018.

[54] Z. Wang, A. C. Bovik, H. R. Sheikh, and E. P. Simoncelli, "Image quality assessment: From error visibility to structural similarity," *IEEE Transactions on Image Processing*, vol. 13, no. 4, pp. 600–612, 2004.

[55] Yoo, T.S., M. J. Ackerman, W. E. Lorensen, W. Schroeder, V. Chalana, S. Aylward, D. Metaxas, and R. Whitaker., "Engineering and Algorithm Design for an Image Processing API: A Technical Report on ITK - The Insight Toolkit. In Proc. of Medicine Meets Virtual Reality,," *J. Westwood, ed., IOS Press Amsterdam*, vol. 85, pp. 586–592, 2002.

[56] M. Mccormick, X. Liu, J. Jomier, C. Marion, and L. Ibanez, "Itk: Enabling reproducible research and open science," *Frontiers in Neuroinformatics*, vol. 8, no. FEB, pp. 1–11, 2014.

[57] M. Jenkinson, "Measuring Transformation Error by RMS Deviation," Oxford Centre for Functional Magnetic Resonance Imaging of the Brain (FMRIB), Oxford, Tech. Rep., 1999.

[58] M. Reuter, M. D. Tisdall, A. Qureshi, R. L. Buckner, A. J. van der Kouwe, and B. Fischl, "Head motion during MRI acquisition reduces gray matter volume and thickness estimates," *NeuroImage*, vol. 107, pp. 107–115, 2015.

[59] P. L. Bazin, H. E. Nijsse, W. van der Zwaag, D. Gallichan, A. Alkemade, F. M. Vos, B. U. Forstmann, and M. W. Caan, "Sharpness in motion corrected quantitative imaging at 7T," *NeuroImage*, vol. 222, no. July, p. 117227, 2020.

[60] F. Gretsch, H. Mattern, D. Gallichan, and O. Speck, "Fat navigators and Moiré phase tracking comparison for motion estimation and retrospective correction," *Magnetic Resonance in Medicine*, vol. 83, no. 1, pp. 83–93, 2020.

[61] P. DiGiacomo, J. Maclaren, M. Aksoy, E. Tong, M. Carlson, B. Lanzman, S. Hashmi, R. Watkins, J. Rosenberg, B. Burns, T. W. Skloss, D. Rettmann, B. Rutt, R. Bammer, and M. Zeineh, "A within-coil optical prospective motion-correction system for brain imaging at 7T," *Magnetic Resonance in Medicine*, vol. 84, no. 3, pp. 1661–1671, 2020.

[62] M. Aksoy, J. Maclaren, and R. Bammer, "Prospective motion correction for 3D pseudo-continuous arterial spin labeling using an external optical tracking system," *Magnetic Resonance Imaging*, vol. 39, pp. 44–52, 2017.

[63] A. Z. Kyme, M. Aksoy, D. L. Henry, R. Bammer, and J. Maclaren, "Marker-free optical stereo motion tracking for in-bore MRI and PET-MRI application," *Medical Physics*, vol. 47, no. 8, pp. 3321–3331, 2020.

[64] K. Nael, P. S. Pawha, L. Fleysher, K. George, J. Stueben, M. Roas-Loeffler, B. N. Delman, and Z. A. Fayad, "Prospective Motion Correction for Brain MRI Using an External Tracking System," *Journal of Neuroimaging*, vol. 31, no. 1, pp. 57–61, 2021.

[65] J. MacLaren, K. J. Lee, C. Luengviriya, O. Speck, and M. Zaitsev, "Combined prospective and retrospective motion correction to relax navigator requirements," *Magnetic Resonance in Medicine*, vol. 65, no. 6, pp. 1724–1732, 2011.

[66] S. Kecskemeti, A. Samsonov, J. Velikina, A. S. Field, P. Turski, H. Rowley, J. E. Lainhart, and A. L. Alexander, "Robust motion correction strategy for structural MRI in unsedated children demonstrated with three-dimensional radial MPnRAGE," *Radiology*, vol. 289, no. 2, pp. 509–516, 2018.

[67] C. Glessgen, D. Gallichan, M. Moor, N. Hainc, and C. Federau, "Evaluation of 3D fat-navigator based retrospective motion correction in the clinical setting of patients with brain tumors," *Neuroradiology*, vol. 61, no. 5, pp. 557–563, 2019.

Appendix A

Paper I

Slipsager JM, Glimberg SL, Søgaard J, Paulsen RR, Johannesen HH, Martens PC, Seth A, Marner L, Henriksen OM, Olesen OV, Højgaard L. *Quantifying the Financial Savings of Motion Correction in Brain MRI: A Model-Based Estimate of the Costs Arising From Patient Head Motion and Potential Savings From Implementation of Motion Correction.* Journal of Magnetic Resonance Imaging, 2020,52(3), 731-738

Quantifying the Financial Savings of Motion Correction in Brain MRI: A Model-Based Estimate of the Costs Arising From Patient Head Motion and Potential Savings From Implementation of Motion Correction

Jakob M. Slipsager*†‡, Stefan L. Glimberg‡, Jes Søgaard,§ Rasmus R. Paulsen*, Helle H. Johannesen†, Pernille C. Martens¶, Alka Seth¶, Lisbeth Marner†‖, Otto M. Henriksen†, Oline V. Olesen*†‡, Liselotte Højgaard†
*DTU Compute, Technical University of Denmark, Denmark
†Department. of Clinical Physiology, Nuclear Medicine & PET, Rigshospitalet, University of Copenhagen, Denmark
‡TracInnovations, Ballerup, Denmark
§Institute of Clinical Research, Health, University of Southern Denmark, Odense, Denmark
¶Department of Radiology, Rigshospitalet, University of Copenhagen, Copenhagen, Denmark
‖Department of Clinical Physiology and Nuclear Medicine, Copenhagen University Hospital Bispebjerg, Copenhagen, Denmark

***Abstract*—Background: Patient head motion is a major concern in clinical brain MRI, as it reduces the diagnostic image quality and may increase examination time and cost.**

Purpose: To investigate the prevalence of MR images with significant motion artifacts on a given clinical scanner and to estimate the potential financial cost savings of applying motion correction to clinical brain MRI examinations.

Study Type: Retrospective.

Subjects: In all, 173 patients undergoing a PET/MRI dementia protocol and 55 pediatric patients undergoing a PET/MRI brain tumor protocol. The total scan time of the two protocols were 17 and 40 minutes, respectively.

Field Strength/Sequences: 3 T, Siemens mMR Biograph, MPRAGE, DWI, T1 and T2-weighted FLAIR, T2-weighted 2D-FLASH, T2-weighted TSE.

Assessment: A retrospective review of image sequences from a given clinical MRI scanner was conducted to investigate the prevalence of motion-corrupted images. The review was performed by three radiologists with different levels of experience using a three-step semiquantitative scale to classify the quality of the images. A total of 1013 sequences distributed on 228 MRI examinations were reviewed. The potential cost savings of motion correction were estimated by a cost estimation for our country with assumptions.

Statistical Test: The cost estimation was conducted with a 20% lower and upper bound on the model assumptions to include the uncertainty of the assumptions.

Results: 7.9% of the sequences had motion artifacts that decreased the interpretability, while 2.0% of the sequences had motion artifacts causing the images to be nondiagnostic. The estimated annual cost to the clinic/hospital due to patient head motion per scanner was $45,066 without pediatric examinations and $364,242 with pediatric examinations.

Data Conclusion: The prevalence of a motion-corrupted image was found in 2.0% of the reviewed sequences. Based on the model, repayment periods are presented as a function of the price for applying motion correction and its performance.

I. Introduction

Magnetic Resonance Imaging (MRI) is an important imaging modality for patient diagnosis and research, and brain MRI is performed worldwide. However, MRI requires longer acquisition times when compared to computed tomography (CT), and patients need to lie still in a narrow and often loud scanner bore. A typical brain examination includes four to six sequences, each taking 2–6 minutes, requiring the patient to lie in the scanner for more than 20 minutes. Such long examinations can make MRI an uncomfortable and stressful experience for the patients. Due to the long acquisition times and uncomfortable environment, patient head motion is a major concern in brain MRI, as motion impairs the diagnostic quality of the images. Recent advancements of high-field MR scanners allowing improved spatial resolution [1], are even more sensitive to small motions, since the threshold for destructible subject motion decreases with the spatial resolution [2, 3]. Gretsch et al. reported [4] that 33 out of 36 MP2RAGE scans with a 0.5 mm isotropic resolution of healthy volunteers have visual artifacts related to motion. The volunteers were instructed to remain motionless during the scans and only small motion due to, e.g., breathing or swallowing, was observed.

The consequences of head motion during image acquisition are low-quality images corrupted by artifacts, known as ghosting, ringing, and blurring [5]. This degradation in image quality makes the interpretation more difficult and increases the

risk that the radiologist may overlook key diagnostic features. Repeating one or more of the MRI sequences is often necessary to obtain images of sufficient diagnostic quality, but at the expense of prolonged examination time, causing increased patient stress and discomfort, and a lower patient throughput. According to a recent study, repeated sequences were necessary in 19.8% of the MRI examinations, adding an extra cost of ∼$115,000 per scanner per year [6]. Thus, motion not only increases patient discomfort by prolonging the examination, but also adds additional costs for the hospital. Sedation or anesthesia are commonly used in pediatric examinations to avoid motion, but these methods come with risks [7, 8] and costs. Vanderby et al. [9] reported that an MRI examination using sedation or anesthesia increased the total examination costs by a factor of 3 and 10, respectively.

To reduce the negative impact of head motion, numerous motion mitigation techniques have been proposed [10, 11].

While there is much work devoted to developing new and better solutions for motion correction, the potential financial benefits of motion correction have not been thoroughly investigated. Hence, the focus of this work was on qualifying, in an extreme model, the costs of motion degradation.

II. Materials and Methods

A. Data

Two examination protocols with 228 patients in total were selected for this study: one investigating dementia patients (N = 173), and one investigating pediatric patients (N = 55) with brain tumors including both pre- and postoperative examinations. The median ages were 73 years (range 17–94 years) and 11 years (range 1 month to 19 years), respectively. Both hybrid positron emission tomography (PET)/MRI protocols were performed with an mMR Biograph hybrid 3T PET/MRI scanner (Siemens Healthcare, Erlangen, Germany). The pediatric study was approved by the Danish National Committee on Health Research Ethics (ID: H-6-2014-095) and registered at clinicaltrials.gov (NCT03402425), and all patients/parents gave written informed consent for participation in the study. For the dementia protocol, the retrospective use of patient data was approved by the Danish Patient Safety Authority (ref. 3-3013-1513/1).

Only diagnostically used MRI sequences were evaluated, whereas all PET and PET-related MRI sequences, e.g., for planning and attenuation correction, from both protocols were excluded, in order to be able to generalize to nonhybrid MRI scanners. Examinations using sedation or anesthesia were excluded, since these patients were assumed to remain motionless during the examination.

B. Review of MRI Images

Three MRI radiologists (years of experience: H.J.: 19 years, P.M.: 4 years, A.S.: 5 years) visually reviewed all sequences uploaded to PACS (General Electric, Milwaukee, WI) from the two selected protocols and assigned a quality score to each image volume. The quality score was divided into three groups: score 1 = images optimal for clinical use; score 2 = images useful for diagnosis, but not optimal; and score 3 = nondiagnostic images, i.e., requiring a repeated scan. The radiologists were instructed to assign the quality score based only on the severity of motion artifacts. Images with minor motion artifacts appearing on a single slice or with artifacts other than motion were classified as optimal for clinical use (score 1). Images were scored individually by the three radiologists and the median score was used as the final image score. The interobserver variability is given by the number of sequences with all equal scores, two equal scores, and all different scores as the fraction of the total number of evaluated sequences.

C. Estimation of Motion-Induced Costs

The financial costs of head motion were estimated in four different cost categories described below. Cost categories (1), (2), and (4) estimated the motion-related costs to the clinic or hospital, while (3) estimated the additional costs to society other than to the clinic and hospital, as described below. The four cost categories were based on an MRI scanner performing 2000 brain examinations per year, corresponding to eight examinations per day with the scanner operating only on weekdays. The average examination contained five sequences, based on the number of non-PET related sequences in the two selected protocols. All assumptions used to estimate (1–4) are summarized in Table I. Values for lower and upper ranges are also shown, to specify the uncertainty for each assumption. Cost categories (1–4) estimates the following:

1) *The added extra costs to the clinic when motion-corrupted images are detected and repeated during the examination.* The added costs are estimated from the perspective of the Department of Clinical Physiology, Nuclear Medicine & PET, Rigshospitalet, Denmark. Here, the cost of a standard head MRI examination is $555 per hour inclusive of costs for the radiologist, radiographers, and other staff. Extra examination costs related to gadolinium administration, sedation, or anesthesia were not considered here in order to simplify the assumptions. Based on our image quality review, outlined in the next section, it is assumed that the probability that a given sequence must be repeated is 2.0%. In a previous study this was 5.5%, and this is used as an upper bound [6].
2) *The additional costs to the clinic when motion-corrupted images are not detected or repeated during the examination.* Examinations with motion-corrupted image volumes add additional inspection time to the radiologist and if essential images are nondiagnostic, a reexamination must be conducted. The additional time to review and to refer the patient to a new MRI examination by a radiologist is assumed to be 20 minutes per examination, and it is assumed that the hourly rate of the radiologist is $111. Our review of 1013 sequences uploaded to PACS showed that 4.4% of the examinations contained at least one nondiagnostic sequence.

TABLE I. LIST OF ASSUMPTION USED IN THE FOUR MODEL CALCULATIONS

Assumption	Model value	Range[a]	Explanation
Number of MRI neuro examinations per scanner per year.	2000	1600–2400	Correspond to eight examinations per day if the scanner is operating only at weekdays
The fraction of repeated MRI sequences.	2.0%	2.0–5.5%	Prevalence of motion corrupted images. The upper bound is equal to previous findings [6].
Number of MRI sequences per examination.	5	4-6	Average number of sequences per examination
Added time per repeated sequence.	5 minutes	4–6 minutes	The cost of an MRI examination at Department of Clinical Physiology, Nuclear Medicine & PET, Rigshospitalet.
MRI examination cost with anesthesia.	$4,433	$3,546–$5,320	Additional cost of a brain MRI examination, where the pediatric patient is anesthetized during the examination.
The fraction of MRI examinations that needs to be repeated.	4.4%	3.5–5.3%	See section (Prevalence of Motion-Corrupted Images).
Added work time to radiologists.	20 minutes	16–24 minutes	When an uploaded examination contains one or more nondiagnostic sequences, a radiologist uses additional time to conclude that the images are not suited for diagnostic and order a new examination.
Duration of new MRI examination	40 minutes	32–48 minutes	Scan time plus patient preparation.
Hourly rate of a radiologist.	$111	$89–$133	Hourly rate of a radiologist at Department of Clinical Physiology, Nuclear Medicine & PET, Rigshospitalet.
The fraction of patients working.	25%	20–30%	We assume that 50% of the examined patients are within the working age (18–70 years) and 50% of this group is not able to maintain a job, due to their illness.
Lost working time per examination.	30 minutes		A 30-minute time buffer is added to every examination in case that motion corrupted sequences need to be repeated.
The fraction of pediatric examinations.	10%	8%–12%	Assumption will depend on case mix.
The fraction of pediatric examinations using sedation or anesthesia	36%	29–43%	36% of the reviewed examinations in the pediatric protocol were performed with sedation or anesthesia.
Lost earnings to the society per hour.	$33	$26–$40	

MRI = MRI = magnetic resonance imaging.
[a] Values used for our model are average value or lower bound, whichever seems most correct. This choice was made to avoid overestimating the cost savings of implementing motion correction. Assumptions are dependent on local healthcare costs; please see Discussion for further considerations.

3) *The additional costs to society, as lost working earnings from the scanned patients, due to prolonged examination time.* Due to the problem of head motion, it is a common practice in the department to add a 30-minute time buffer in our patient information, so that patients are prepared if motion-corrupted sequences need to be repeated. Due to this precaution every patient loses 30 minutes. Our cost categories are estimated from the perspective of Danish society, where the average working earning rate for Danish citizens is ∼$33 per hour [12]. Not all scanned patients have jobs, and for them the time buffer will not result in lost working earnings. It is assumed that 50% of the examined patients are within the working age (18-70 years) and that 50% of these patients are not able to maintain a job, due to their physical condition. Hence, 25% of the scanned patients are assumed to be working on the day of the MRI examination. For simplicity, patients accompanied by a relative are also represented in the 25%.
4) *The additional costs to the hospital or clinic when anesthesia is necessary to avoid motion in pediatric examinations.* Anesthesia is a common tool to minimize motion in pediatric patients and remove the risk of motion-corrupted images. At our target department, a pediatric MRI examination with anesthesia increases the cost by $4433. The number of pediatric examinations and the use of anesthesia varies between scanner sites. In our model, it is assumed that 10% of the examinations are pediatric, and that 36% of the pediatric

patients are anesthetized during the examination. These expenditures can either be on the budget of the imaging department or the hospital, depending on the hospital administration.

On top of the costs listed above, there are costs to informal caregivers and family, which might be reduced by reducing motion artifacts, as their time spent at the hospital may be shorter and their anxiety may be reduced. Patients may also be anxious and worry if their movements might impair the quality of their scan. These costs are not well documented and difficult to estimate and have not been included in the model.

D. Savings When Implementing Motion Correction

The potential repayment period when implementing motion correction in a clinical workflow depends on the cost of subject motion, the motion correction implementation cost, and the performance of the implemented solution. Due to differences in correction strategies, the performance or the fraction of motion-corrupted sequences that can be corrected depends on the correction method itself. Performance and implantation cost comparison of various motion correction methods are not the purpose of this article. The correction performance and implementation cost are therefore left as function variables in the cost-saving model. The potential repayment period of a motion correction solution is estimated as a function of the total cost and the performance of the implemented motion correction solution, given as:

$$f\left(c,p\right)=\frac{c}{\sum_i\left[Cost\ category\ i\right)]\,p}, \tag{1}$$

where f is the repayment period, c is the implementation cost, and p is the motion correction performance rate. Cost category i) corresponds to the additional cost due to subject motion, as previously described in cost categories (1–4).

It is assumed that all adult patients complete their scans. This is not the case for pediatric patients, where anesthesia is necessary to avoid motion and even to keep the child in the scanner. Even with perfect motion correction, some pediatric patients still need anesthesia, for whom motion correction will not have cost-saving effects. Runge et al. [13] suggested a child-centered care solution to reduce the number of examinations with anesthesia of 4–10-year-old children. The concept was tested on 41 children 4–6 years old and 95% of the examinations were successfully completed without anesthesia. Anesthesia rates in the literature are reported as 47–75% [13] for children in the age range of 4–10 years. It is assumed that the age of the scanned children is uniformly distributed and children older than 11 years are scanned without anesthesia. Thus, the group of 4–10-year-old children corresponds to 64% of all scanned children <11 years old. This results in 30–48% of the pediatric patients scanned with anesthesia are 4–10 years old. Using a similar solution [13] together with motion correction with a combined success rate of 95% (76% lower bound and 95% upper bound), it is assumed that 37% (46% upper bound, 23% lower bound) would be able to complete a standard examination. Hence, prior to estimating the repayment period in Eq. (1), 37% (46% upper bound and 23% lower bound) of cost category (4) was used. The total implementation cost of motion correction would also include the cost of a solution similar to child-centered care.

III. Results

A. Prevalence of Motion-Corrupted Images

For the review, 228 MRI examinations from a period between March 2015 and December 2017 were included with a total of 1013 sequences. One hundred and seventy-three (76%) of the examinations were from the dementia protocol and 55 (24%) from the pediatric protocol. The radiologists reviewed all 1013 sequences and assigned a quality score according to the severity of motion artifacts to each sequence. In 85.7% of the reviewed sequences the same score were assigned by all three radiologists. In 14.0% one score was assigned differently and in 0.3% all scores were different. Figure 1 shows example magnetization-prepared rapid gradient-echo (MPRAGE) sequences assigned with a score from 1–3, respectively. The

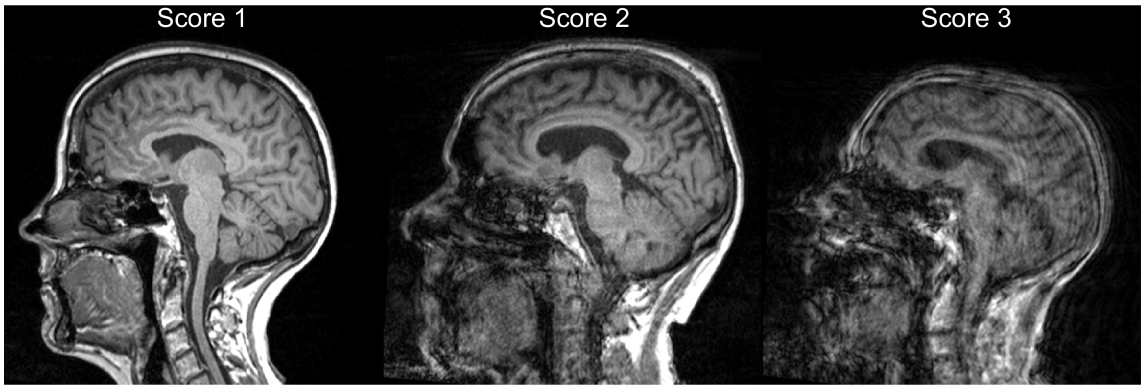

Fig. 1. Sagittal slices from MPRAGE sequences assigned with a score from 1 to 3.

left chart in Fig. 2 summarizes the results of the review. It shows that 913 (90.1%) of the acquired sequences contain no or minimal motion artifacts and the image quality was optimal for clinical use. It also shows that 80 (7.9%) of sequences were corrupted by motion to a degree that it decreased the diagnostic utility and 20 (2.0%) of these sequences could not be used for diagnostics purposes and should be repeated. Out of the 100 motion-corrupted sequences, 23, 20, and 57 were acquired in the first, second, and third part of the examination, respectively. The total raw image acquisition time for those 100 sequences was ∼4½ hours, which is equal to 3 minutes per sequence. The chart to the right shows the distribution of the 228 MRI examinations, with 10 (4.4%) of the examinations containing one or more sequences that needed to be repeated.

B. Estimation of Motion-Induced Cost

The results of the four estimated cost categories are presented in Table II together with the assumptions used for each. The sum of the costs in categories (1), (2), and (4) are the annual costs to the department or hospital: $364,242 per scanner. The results using the lower and upper bounds are $150,101 and $785,795 per scanner per year, respectively. The total cost to society is $372,492 per scanner per year as the sum of the costs estimated in cost categories (1–4), and the results using the lower bound values: $154,325 and upper bound values: $800,051 (Table II).

C. Savings When Implementing Motion Correction

Using the above estimated costs, the potential repayment period when implementing motion correction in a clinical workflow is shown as a function of cost and performance in Fig. 3. From the figure it is seen that a motion correction solution for adult scans only (top row) with a total cost of $100,000 would be financially viable for the hospital after 5 years if it achieves correction performance of at least 45% (16% for upper bound). The same solution would be viable after 3 years if 75% performance is achieved. Based on the conservative lower bound estimates, such a solution with 45% performance would be financially viable after 12 years.

IV. Discussion

MRI is the method of choice for diagnosis of patients with brain diseases and for research in neurobiology. However, the acquisition time is often long and during the scan patients must lie still in a narrow and noisy scanner bore, making MRI examinations uncomfortable. This increases the risk of patient motion, impairing image quality.

In this work, the prevalence of motion-corrupted images was studied by reviewing 1013 sequences from 228 MRI examinations. Further, a model-based estimate was used to estimate the financial costs of head motion and to determine if implementation of motion correction is cost saving.

We found that 4.4% of the MRI brain examinations had sequences that were corrupted by motion artifacts to such an extent that they had to be repeated. It is important to note that the two patient populations are considered particularly prone to motion and the cost-saving estimates are likely exaggerated. However, another study that was performed across a broader patient population and a wider range of illnesses reported that 19.8% of the exams contained repeated sequences [6].

The suggested cost analysis indicates that the implementation cost of a perfect (100% performance) motion correction solution on an adult population must not be more than $225,300 ($91,990 lower bound and $634,500 upper bound), if the solution would be financially viable after 5 years. However, it is unlikely that a motion correction solution would have 100% performance on any sequence under any motion condition. A more reasonable motion correction solution with a performance on 50% would result in a maximal implementation cost of $47,000, using the most conservative model

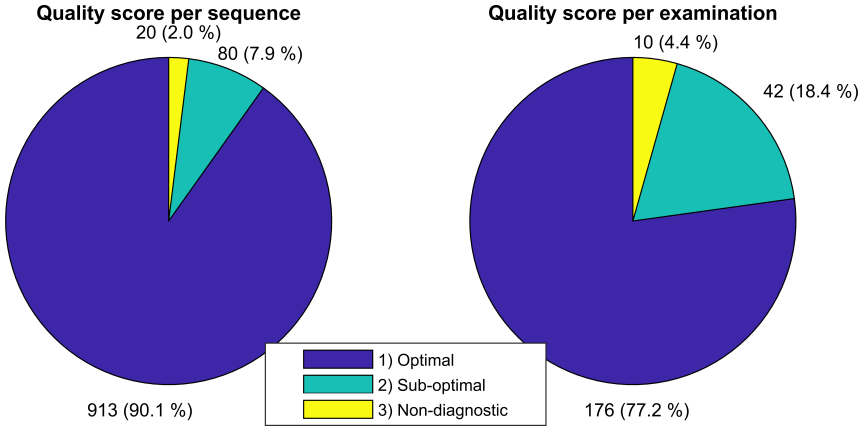

Fig. 2. Left: Review of 1013 sequences, where each sequence is classified into one of three classes. Right: Distribution of 228 MRI examinations classified into the same three classes based on the sequence with the lowest quality.

TABLE II. RESULTS OF THE COSTS IN CATEGORIES (1–4)

	Model result	Lower bound	Upper bound
Cost category (1): Costs due to repeated sequences			
Number of examinations per year	2000	1600	2400
Number of sequences per examination	5	4	6
The fraction of repeated sequences	2.0%	2.0%	5.5%
Added time per rescan	5 min.	4 min.	6 min.
Examination cost per hour	$555	$444	$666
The extra costs to the clinic per scanner per year	$9,250	$3,789	$52,747
Cost category (2): Repeated examinations			
Number of examinations per year Number	2000	1600	2400
The fraction of repeated examinations	4.4%	3.5%	5.3%
Added work time to a radiologist	20 min.	16 min.	24 min.
The hourly fee to a radiologist	$111	$89	$133
Examination cost per hour	$555	$444	$666
Duration of new examination	40 min.	32 min.	48 min.
Additional cost to the clinic per scanner per year	$35,816	$14,670	$74,268
Cost category (3): Lost work from the patients			
Number of examinations per year Number	2000	1600	2400
The fraction of patients in work Lost	25%	20%	30%
Lost working time per examination	30 min.	30 min.	30 min.
Hourly working value	$33	$26	$40
The extra costs to the society per scanner per year	$8,250	$4,224	$14,256
Cost category (4): Anesthesia			
Number of examinations per year Number	2000	1600	2400
Fraction of pediatric examination	10%	8%	12%
Fraction of examinations using anesthesia	36%	29%	43%
Cost of MRI examination with anesthesia	$4,433	$3,546	$5,320
The extra costs to the clinic per scanner per year	$319,176	$131,642	$658,779
Cost categories combined			
Cost category (1) + (2)	$45,066	$18,459	$127,015
Cost category (1) + (2) + (3)	$53,316	$22,683	$141,271
Cost category (1) + (2) + (4)	$364,242	$150,101	$785,795
Cost category (1) + (2) + (3) + (4)	$372,492	$154,325	$800,051

assumptions for the adult population. Applying the same solution and conservative assumptions to a mixed population with 10% pediatric, the highest implementation cost is $132,500. However, this implementation cost is also including the cost of extra preparation of the pediatric patients to make them complete their examination.

Kecskemeti et al. [14] reported that retrospective motion correction of MPRAGE sequences was able to increase image quality from unusable to good for clinical use in all of the seven sequences. Applying such a solution in our setting with five sequences per examination results in a performance of 20%, since this solution is only available for MPRAGE sequences. Based on our suggested cost analysis, such a motion correction solution would be a cost saving after 5 years if the implementation cost is below $45,000 ($18,400 lower bound $127,000 upper bound) for the adult population.

Besides the financial benefits to the clinic, hospital, and society, motion correction decreases the need for rescans and results in shorter examination times, leading to increased comfort of the patients. Other nonfinancial benefits to the patients include reduced patient anxiety for causing motion problems. For relatives and informal caregivers, reduced anxiety and reduced waste of time are important. These costs have not been included in our model. Also, patient time costs include only lost work hours and not shadow prices or lost leisure time.

In pediatric examinations, anesthesia is often necessary to avoid patient motion in order to obtain images of sufficient quality, or just to keep the patient in the scanner. It is expected that motion correction reduces the use of anesthesia especially for the group of older children. It is of great importance to minimize the use of anesthesia due to the associated health risks and the discomfort to the patient and relatives. Further, there would be substantial financial benefits to the clinic if anesthesia rates could be reduced using motion correction as seen from cost category (4).

A recent study [15] concluded that it is essential to reduce motion artifacts to increase reproducibility and credibility of neuroreceptor studies in research protocols. The costs related to a reduction of such methodologically flawed studies are difficult to estimate, but are likely substantial.

The additional cost due to repeated sequences in an MRI examination, estimated in cost category (1), is comparable to the cost estimated by Andre et al. [6]. However, our estimated

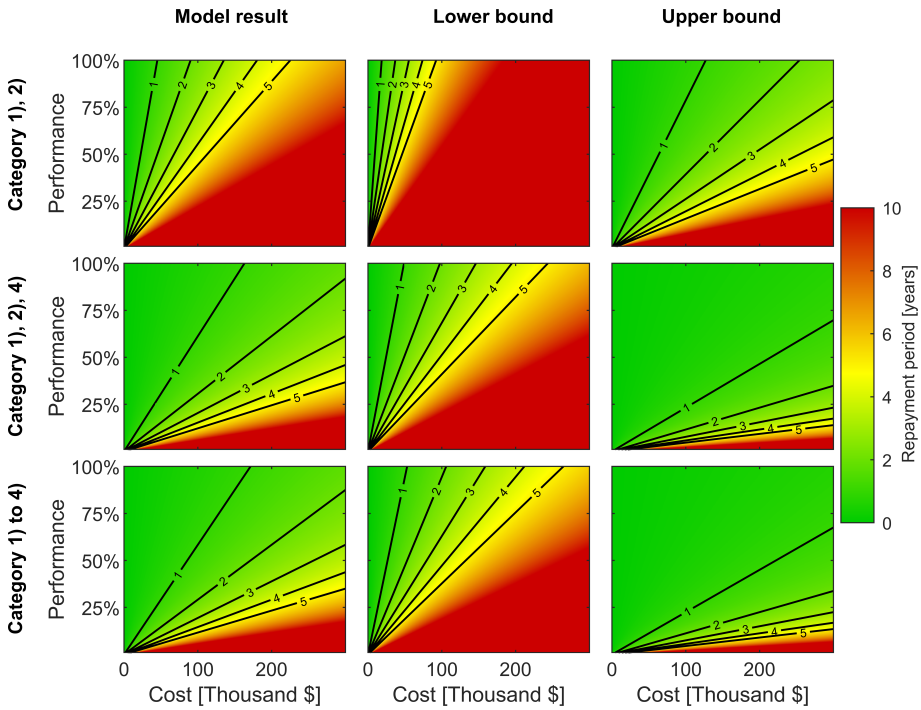

Fig. 3. Repayment period as a function of the price for implementing motion correction and the performance of the implemented motion correction solution. Each line indicates an iso-repayment level in years. Top row: Repayment periods based on costs from an adult population only (the sum of cost categories (1) and (2)). Middle row: Repayment periods based on costs from a mixed population with 10% pediatric patients (the sum of cost categories (1), (2), and (4)). Bottom row: Repayment periods based on costs from a mixed population with 10% pediatric patients and the cost of lost earnings to the society (the sum of cost categories (1–4)).

costs are generally lower, as the number of MRI examinations per scanner per year was assumed to be 2000 compared to 3588 in Ref. [6].

In the estimated cost of subject motion, it was assumed in cost category (2) that patients would get a standard reexamination if the previous examination could not be used for diagnostics. This may not be the case for patients where all means were tried to obtain images with sufficient quality in the ordinary examination and these patients would not get a standard reexamination. No additional cost is therefore added in these cases where reexaminations are not performed, which results in overestimated cost.

The cost analysis was conducted as a model-based estimate with assumptions, thus no prospective studies were made in order to estimate the net cost of motion correction. This implies uncertainty in the estimated costs and repayment period. Therefore, the analysis was conducted including 20% lower and upper bounds. However, no investment recommendation can be given before pilot motion correction installations have shown a proven cost advantage.

The estimated costs and savings are a result of the value assumptions based on our clinic in Denmark. The assumed values are specific to Denmark and values for usage of scanners, payment to radiologists, working value in the society at large, etc., will differ in other countries [16]. In particular, the values for <MRI examination cost per hour>, <MRI examination cost with anesthesia>, <Hourly rate of a radiologist>, and <Lost earnings to the society per hour> must be changed to represent other specific countries.

V. Conclusion

It was found that 2.0% of the reviewed MRI brain sequences were corrupted by motion artifacts to a degree that they could not be used for diagnostics. Model calculations with assumptions were used to estimate the financial costs of head motion to the Danish society. These costs were used to estimate repayment periods of motion correction as functions of correction performance and implementation cost.

Acknowledgment

Contract grant sponsor: John and Birthe Meyer Foundation The Danish Childhood Cancer Foundation.

REFERENCES

[1] I. Havsteen, A. Ohlhues, K. H. Madsen, J. D. Nybing, H. Christensen, and A. Christensen, "Are movement artifacts in magnetic resonance imaging a real problem?-a narrative review," *Frontiers in Neurology*, vol. 8, no. 1, pp. 1–8, 2017.

[2] D. Stucht, K. A. Danishad, P. Schulze, F. Godenschweger, M. Zaitsev, and O. Speck, "Highest Resolution In Vivo Human Brain MRI Using Prospective Motion Correction," *PLOS ONE*, vol. 10, no. 7, p. e0133921, jul 2015. [Online]. Available: https://dx.plos.org/10.1371/journal.pone.0133921

[3] C. Federau and D. Gallichan, "Motion-Correction Enabled Ultra-High Resolution In-Vivo 7T-MRI of the Brain," *PLoS ONE*, pp. 1–12, 2016.

[4] F. Gretsch, H. Mattern, D. Gallichan, and O. Speck, "Fat navigators and Moiré phase tracking comparison for motion estimation and retrospective correction," *Magnetic Resonance in Medicine*, vol. 83, no. 1, pp. 83–93, 2020.

[5] M. L. Wood and R. M. Henkelman, "MR image artifacts from periodic motion," *Medical physics*, vol. 12, no. 2, pp. 143–151, 1985.

[6] J. B. Andre, B. W. Bresnahan, M. Mossa-Basha, M. N. Hoff, C. Patrick Smith, Y. Anzai, and W. A. Cohen, "Toward quantifying the prevalence, severity, and cost associated with patient motion during clinical MR examinations," *Journal of the American College of Radiology*, vol. 12, no. 7, pp. 689–695, 2015.

[7] R. D. Sanders, J. Hassell, A. J. Davidson, N. J. Robertson, and D. Ma, "Impact of anaesthetics and surgery on neurodevelopment: An update," *British Journal of Anaesthesia*, vol. 110, pp. 53–72, 2013.

[8] D. Blumenthal and M. Tavenner, "Anesthesia and Developing Brains — Implications of the FDA Warning," *The New England Journal of Medicine*, vol. 376, no. 10, pp. 905–907, 2017.

[9] S. A. Vanderby, P. S. Babyn, M. W. Carter, S. M. Jewell, and P. D. Mckeever, "Effect of Anesthesia and Sedation on Pediatric MR Imaging Patient Flow," *Radiology*, vol. 256, no. 1, pp. 229–237, 2010.

[10] M. Zaitsev, J. Maclaren, and M. Herbst, "Motion artifacts in MRI: A complex problem with many partial solutions," *Journal of Magnetic Resonance Imaging*, vol. 42, no. 4, pp. 887–901, jan 2015.

[11] J. Maclaren, M. Herbst, O. Speck, and M. Zaitsev, "Prospective Motion Correction in Brain Imaging: A Review," *Magnetic resonance in medicine*, vol. 69, no. 3, pp. 621–636, 2013.

[12] Danmarks Statistik, "Average Income in Denmark." [Online]. Available: https://statistikbanken.dk/INDKP105

[13] S. B. Runge, N. L. Christensen, K. Jensen, and I. E. Jensen, "Children centered care: Minimizing the need for anesthesia with a multi-faceted concept for MRI in children aged 4–6," *European Journal of Radiology*, vol. 107, pp. 183–187, 2018.

[14] S. Kecskemeti, A. Samsonov, J. Velikina, A. S. Field, P. Turski, H. Rowley, J. E. Lainhart, and A. L. Alexander, "Robust motion correction strategy for structural MRI in unsedated children demonstrated with three-dimensional radial MPnRAGE," *Radiology*, vol. 289, no. 2, pp. 509–516, 2018.

[15] M. Nørgaard, "Optimizing Preprocessing Pipelines in PET/MR Neuroimaging," Ph.D. dissertation, University of Copenhagen, 2019.

[16] D. G. Walker, Y. Teerawattananon, R. Anderson, and G. Richardson, "Generalisability, transferability, complexity and relevance, chapter 5," in *Evidence-based decisions and economics health care, social welfare, education and criminal justice*, 2nd ed., I. Shemilt, M. Mugford, L. Vale, K. Marsh, and C. Donaldson, Eds. Wiley-Blackwell, 2011, ch. 5, pp. 56–65.

Appendix B

Paper II

Slipsager JM, Ellegaard AH, Glimberg SL, Paulsen RR, Dylan TM, Wighton P, Van Der Kouwe A, Marner L, Henriksen OM, Law I, Olesen OV. *Markerless motion tracking and correction for PET, MRI, and simultaneous PET/MRI.* Plos one, 2019, 14(4), e0215524

PLOS ONE

RESEARCH ARTICLE

Markerless motion tracking and correction for PET, MRI, and simultaneous PET/MRI

Jakob M. Slipsager[1,2,3☯]*, Andreas H. Ellegaard[1,2☯], Stefan L. Glimberg[3], Rasmus R. Paulsen[1], M. Dylan Tisdall[4], Paul Wighton[5], André van der Kouwe[5], Lisbeth Marner[2], Otto M. Henriksen[2], Ian Law[2], Oline V. Olesen[1,2,3]

1 Department of Applied Mathematics and Computer Science, Technical University of Denmark, Lyngby, Denmark, **2** Department of Clinical Physiology, Nuclear Medicine and PET, Rigshospitalet, University of Copenhagen, Copenhagen, Denmark, **3** TracInnovations, Ballerup, Denmark, **4** Radiology, Perelman School of Medicine, University of Pennsylvania, Philadelphia, Pennsylvania, United States of America, **5** Athinoula. A. Matinos Center for Biomedical Imaging, Department of Radiology, Massachusetts General Hospital, Boston, Massachusetts, United States of America

☯ These authors contributed equally to this work.
* jmsl@dtu.dk

OPEN ACCESS

Citation: Slipsager JM, Ellegaard AH, Glimberg SL, Paulsen RR, Tisdall MD, Wighton P, et al. (2019) Markerless motion tracking and correction for PET, MRI, and simultaneous PET/MRI. PLoS ONE 14(4): e0215524. https://doi.org/10.1371/journal.pone.0215524

Editor: Qinghui Zhang, North Shore Long Island Jewish Health System, UNITED STATES

Received: August 27, 2018

Accepted: April 3, 2019

Published: April 19, 2019

Data Availability Statement: All data files are available from FigShare: Fig 4: 10.6084/m9.figshare.6989339 10.6084/m9.figshare.6989336 Fig 5: 10.6084/m9.figshare.6988802 10.6084/m9.figshare.6989183 10.6084/m9.figshare.6989243 10.6084/m9.figshare.6989309 10.6084/m9.figshare.6989315 10.6084/m9.figshare.6989324 10.6084/m9.figshare.6989327 10.6084/m9.figshare.6989333 Fig 6: 10.6084/m9.figshare.6989354 10.6084/m9.figshare.6989423 10.6084/m9.figshare.6989426 10.6084/m9.figshare.6989429 10.6084/m9.figshare.6989435 10.6084/

Abstract

Objective

We demonstrate and evaluate the first markerless motion tracker compatible with PET, MRI, and simultaneous PET/MRI systems for motion correction (MC) of brain imaging.

Methods

PET and MRI compatibility is achieved by careful positioning of in-bore vision extenders and by placing all electronic components out-of-bore. The motion tracker is demonstrated in a clinical setup during a pediatric PET/MRI study including 94 pediatric patient scans. PET MC is presented for two of these scans using a customized version of the Multiple Acquisition Frame method. Prospective MC of MRI acquisition of two healthy subjects is demonstrated using a motion-aware MRI sequence. Real-time motion estimates are accompanied with a tracking validity parameter to improve tracking reliability.

Results

For both modalities, MC shows that motion induced artifacts are noticeably reduced and that motion estimates are sufficiently accurate to capture motion ranging from small respiratory motion to large intentional motion. In the PET/MRI study, a time-activity curve analysis shows image improvements for a patient performing head movements corresponding to a tumor motion of ±5-10 mm with a 19% maximal difference in standardized uptake value before and after MC.

Conclusion

The first markerless motion tracker is successfully demonstrated for prospective MC in MRI and MC in PET with good tracking validity.

m9.figshare.6989444 10.6084/m9.figshare.6989453 10.6084/m9.figshare.6989462.

Funding: This study was funded by The Danish Childhood Cancer Foundation funded salary (LM) and anesthesia assistance for the clinical PET/MRI study (2014-34, 2015-48), The United States National Institutes of Health (NIH) funded salary (MDT) with grant number R00HD074649, and The United States National Institutes of Health (NIH) National Institute of Child Health and Human Development (NICHD) funded salary (AVDK) with grant number R01HD071664. The funder (TracInnovations) provided support in the form of salaries for authors JMS, SLG and OVO, but did not have any additional role in the study design, data collection, and analysis, decision to publish, or preparation of the manuscript. The specific roles of these authors are articulated in the 'author contributions' section.

Competing interests: The authors JMS, SLG and OVO are commercial affiliated and employees at TracInnovations. This does not alter our adherence to PLOS ONE policies on sharing data and materials.

Significance

As simultaneous PET/MRI systems have become available for clinical use, an increasing demand for accurate motion tracking and MC in PET/MRI scans has emerged. The presented markerless motion tracker facilitate this demand.

Introduction

Magnetic resonance imaging (MRI) and positron emission tomography (PET) are of great importance in the diagnosis and treatment of many neurological diseases. These modalities offer unique tissue contrasts at the expense of long image acquisition duration, making patient head motion a critical problem. The degradation of image quality resulting from patient motion can potentially lead to reduced detection of clinically relevant features, negatively influencing diagnosis and treatment. It is estimated that patient motion increases the cost of MRI examinatios by $115,000 per scanner per year [1]. The problem is particularly acute in pediatric scans, where sedation and anesthesia are often used, which can lead to adverse reactions [2, 3]. To minimize the negative outcome of such head motion, various methods for motion correction (MC) has been proposed for MRI and PET reconstruction.

For MRI, prospective MC, where the imaging field of view (FOV) coordinate system is continuously updated during acquisition, has been demonstrated using a variety of tracking techniques [4, 5]. Retrospective MRI MC uses motion information retrospectively to adjust the reconstruction to compensate for motion-induced errors [5]. Unlike prospective MC, retrospective correction enables reconstruction both with and without motion corrected images.

PET only allows retrospective MC, as the acquisition cannot be dynamically adapted to compensate for motion. However, the MC can take place at different phases of the PET reconstruction, from MC of raw listmode data [6–8] to MC of the reconstructed image frames [9–11]. These MC methods are generally based on the assumption of knowing the precise head pose (position and orientation) during the scanning.

Motion information can be acquired using different sources, both directly from the acquired imaging data or using an add-on motion-tracking systems. Each approach has its own trade-off in terms of accuracy, complexity of implementation, and demands for additional hardware. Estimating motion from the imaging device itself requires no additional hardware, but can impose additional complexity on the acquisition and reconstruction of the data and may have limited time and spatial resolution at the same time. In the context of MRI, motion data are often acquired by redundant sampling patterns, either built into the imaging acquisition, or interleaved as "motion navigators" [4, 5]. In contrast, a variety of methods have been suggested for tracking markers attached to the subject. For MRI, markers have included field probes [12, 13], active markers [14], gradient sensors [15], and optical targets [16–18]. In general, markers must be attached rigidly to the subject, and different attachment strategies have been presented for each of these markers to address this challenge. Applying a stamp to the patient's head has also been investigated as a mean to avoid the risk of marker detachment [19]. However, feature extraction from stamps or facial characteristics alone may be computationally expensive or unstable and has been demonstrated only for retrospective correction. Data-driven motion detection in PET shows promising results [11, 20]. However, it may be difficult to distinguish motion-induced changes from functional changes in tracer distribution over time. These methods resemble a limited time resolution of the motion estimation. Optical marker tracking is somewhat simpler in PET, as the line of sight to the subject is not obscured

by receive coils, as in MRI, allowing more flexible marker design [21]. A markerless motion tracking approach in PET has also been demonstrated on small awake animals using head landmarks and structured light to estimate motion [22, 23]. However, the same accuracy obtained by similar marker based approaches was not achieved and the method was not applied to humans. Finally, simultaneous PET/MRI systems can also use the motion information intrinsic in the MRI data to estimate motion for both systems [24].

Until now, no external motion tracking device has been designed to be compatible with both PET and MRI scanners. Existing solutions for MRI typically require attachment to the receive coils and do not consider the location of the PET detectors. Conversely, motion trackers for PET scanners are not designed to be compatible with the strong magnetic forces acting in the MRI environment.

In this work we present and evaluate the first markerless motion tracker, Tracoline 2.0 (TCL2), addressing rigid head motion for PET, MRI, and simultaneous PET/MRI. While the first generation of Tracoline was designed for MC of PET scans only [25], a mechanical and optical redesign now makes it compatible with both PET and MRI. PET compatibility was originally achieved by positioning the hardware outside the range of the PET detectors to maintain good PET sensitivity. MRI compatibility however, requires a strict non-interfering in-bore design, such that the scanner's strong magnetic field is not affected by any magnetic or electric components. Furthermore, all system components need to resist the strong magnetic field during operation. Finally, for MRI, the limited view of the patient's head through the MRI coils needs to be considered.

The new hardware design comply with these conditions and the current software performance allows for accurate and real-time motion tracking. In combination, these improvements can effectively address the challenge of patient motion in both PET and MRI. Fast and reliable motion estimation are the key features for enabling real-time MC and for being a valuable tool in a clinical setting. We present results demonstrating how real-time motion tracking is applied for prospective MC in MRI and for retrospective MC of PET data reconstruction.

The motion tracker is installed and evaluated on a hybrid PET/MRI scanner during a clinical study consisting of 94 pediatric patients with brain tumors and a controlled MC study with two healthy volunteers. Volunteers are used to demonstrate prospective MC in MRI, because customized scan sequences supporting motion input are required in MRI, but are currently not available for clinical use.

The motion tracker is based on a computer vision technology using a structured light surface scanner, continuously scanning the face of the patient using a synchronized light modulator and camera. This approach requires no attachment of optical markers, reducing the clinical preparation time compared to maker-based solutions. In addition, no patient interaction is required and therefore it does not compromise patient comfort. Further, it eliminates tracking failure due to slipping markers. The system is capable of motion tracking of real patients and a tracking validity parameter (TVP) is used to ensure that the tracking is reliable and that incorrect tracking is not used for motion correction. Using incorrect tracking for motion correction may degrade the images in contrast to correcting the images, which is unacceptable for clinical use especially for prospective MC, where the images without correction does not exist. A TVP is computed for each motion estimate to accept or reject estimates in real time to ensure tracking robustness.

Materials and methods

The motion tracker

TCL2 is the first markerless motion tracker, addressing the challenge of rigid head motion during PET and MRI neuroimaging. It is designed to be compatible with both PET and MRI

modalities and to provide reliable real-time motion feedback during scanning. In order to comply with the restrictive strong magnetic environment inside the MRI scanner room, TCL2 had to be significantly redesigned compared to the first version of the Tracoline motion tracker [7, 25]. MRI compatibility is achieved by replacing all in-bore electronics and objectives with non-magnetic and non-electric components. The motion tracker requires a good view of the patient's head in order to make a 3D facial surface reconstruction. Therefore, to maintain a good in-bore FOV, 3 meter long optical image fibers are introduced to extend the view from the camera and light source, both placed out-bore behind the scanner and away from the personal and patient. The optical fibers thereby act as flexible vision extenders, creating a remote 3D surface scanner. The fragile fibers are enclosed in an energy chain cable carrier to protect them from mechanical injuries. At the end of the optical fibers in-bore, a vision probe facing the patient contains the image objectives, configured to have a focus distance between 10-25 cm. All the out-bore electronics are enclosed in a radio-frequency (RF)-shielded box. The box contains the potentially RF-emitting and ferromagnetic camera and light source. The box is custom made with a 9 mm wooden frame with the inside surfaces of the box are covered with 1 mm RF-shielding copper and all optical fibers pass though waveguides to avoid electromagnetic radiation. 5/12 V DC power is supplied from the adjacent control room through a standard Siemens RF wall filter and data are transferred via an optical cable through a waveguide to the control computer located in the adjacent room.

PET compatibility requires the in-bore vision extenders not to interfere with the in-bore PET detectors encircling the patient's head. The in-bore vision probe is therefore located slightly behind the PET detection area and tilted to an angle allowing for a clear view of the patient through one of the head coil openings.

The integration of the system with a PET/MRI scanner is conceptually illustrated in Fig 1. The motion tracker is installed with an mMR Biograph hybrid 3T PET/MRI scanner (Siemens Healthineers, Erlangen).

TCL2 uses a synchronized camera and light source to continuously scan the surface of the patient's head. The surface scanner produces high-resolution 3D point clouds consisting of thousands of individual points. Non-visible infra-red structured light is used to avoid patient discomfort [26]. The continuous stream of surface scans creates 30 point clouds per second. Each of these point clouds are used for geometric alignment relative to an initial reference position during the scanner image acquisition. Examples of a 3D point cloud can be seen in Fig 2. In this figure, parts of the head coil surface is visible in front of the patient's face. This stationary head coil within the FOV is treated as an inactive foreground segment and hence not included in the motion tracking procedure.

The TCL2 motion tracking software package (TracSuite) has also been updated and improved in terms of performance and reliability, to comply with the real-time tracking constraint of prospective MC. The motion tracking software was re-implemented for fast and parallel shared-memory multiprocessing. TracSuite estimates the patient's head pose using an Iterative Closest Point (ICP) algorithm [27]. The head pose is computed at a frequency of 30 Hz, a sample rate which is sufficient for most MC purposes.

The ICP alignment algorithm imposes the assumption of tracking a rigid surface. Occlusion, rapid motion or facial movements may violate such a rigidity assumption. Also, if the patient moves outside the FOV, accurate tracking is not possible. Therefore, the estimated pose is analyzed against the reference point cloud, in order to determine how reliable the tracking result is. A TVP $\in[0, 1]$, is introduced to indicate the tracking validity of each head pose. When the TVP value is equal or close to 1, it indicates high tracking validity. If the TVP becomes 0, the pose estimate is rejected and the previous pose will be used as a more reliable pose instead.

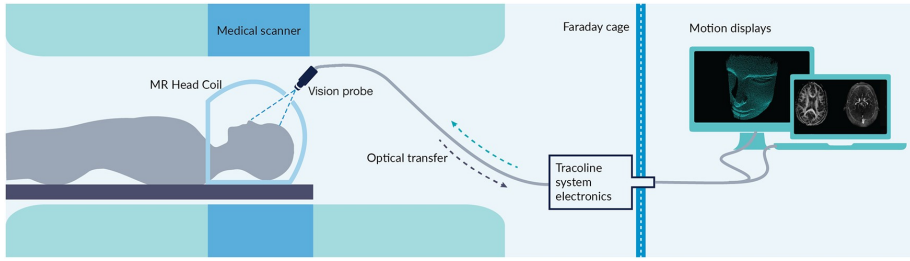

Fig 1. Tracoline 2.0 system integrated with the scanner. Sketch of the developed Tracoline 2.0 system integrated with the mMR Biograph hybrid 3T PET/MRI.

https://doi.org/10.1371/journal.pone.0215524.g001

Data

To demonstrate the compatibility of the motion tracker in a clinical PET and MRI environment, TCL2 was used for motion tracking in pediatric patients with presumed brain tumors. A total of 94 pediatric patient scans (median age 10.1 years, range 0.1-19.5 years) included in a clinical PET/MRI study using ^{18}F-FET were all obtained between March 2015 and January 2018 using an mMR Biograph hybrid 3T PET/MRI scanner (Siemens Healthineers, Erlangen). The pediatric scans consist of one 40 minutes PET acquisition and six MRI scans, where two of the MRI sequences are acquired after injection of intravenous contrast medium Gadovist.

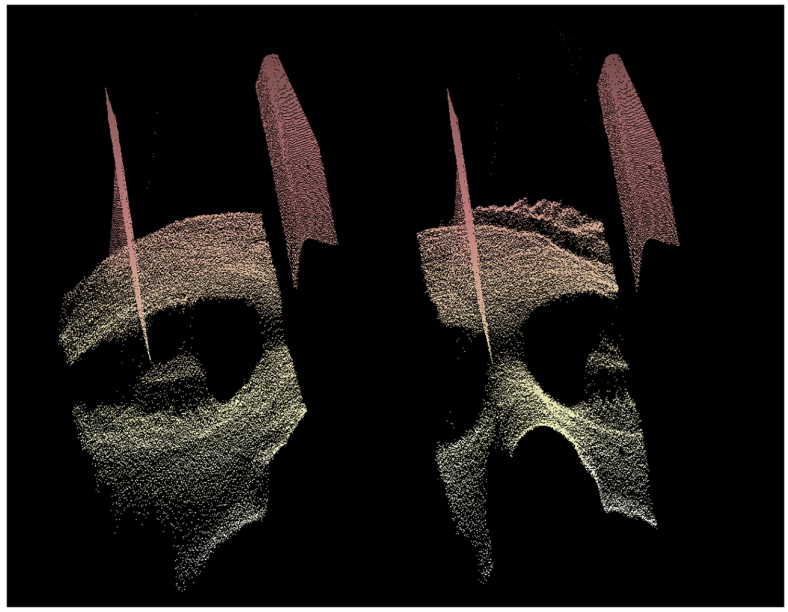

Fig 2. 3D facial point clouds of a subject. 3D facial point clouds of a subject inside an MRI head coil obtained during MRI acquisition using the TCL2 for motion tracking. The two point clouds are obtained at different times during the acquisition. Part of the MRI head coil is seen in front of the facial surface of the patient. It is clearly visible, that the head of the subject has moved relative to the head coil during the acquisition.

https://doi.org/10.1371/journal.pone.0215524.g002

Table 1. List of MRI sequences used in the pediatric scans.

Sequence	Parameters	Voxel Size [mm]
T1 MPRAGE	9° flip angle; TR/TE/TI 1900/2.52/900 ms	1.00x1.00x1.00
T1 TIRM	150° flip angle; TR/TE/TI 2000/34/800 ms	0.45x0.45x4.00
T2 FLAIR	130° flip angle; TR/TE/TI 9000/95/2500 ms	0.43x0.43x4.00
DWI	180° flip angle; TR/TE 5600/61 ms	1.15x1.15x4.00
T2 Blade(GD)	140° flip angle; TR/TE 4000/118 ms	0.72x0.72x5.00
T1 MPRAGE(GD)	9° flip angle; TR/TE/TI 1900/2.52/900 ms	1.00x1.00x1.00

(GD), Contrast enhanced sequences. Contrast medium Gadovist.

https://doi.org/10.1371/journal.pone.0215524.t001

Sequence type and parameters of the six MRI sequences are given in Table 1. The study was approved by The Regional Research Ethics Committees of Capital Region of Denmark (ID: H-6-2014-095) and registered at clinicaltrials.gov (NCT03402425). All patients or their parents gave written informed consent for participation in the study and a subset of the patients has been included in previous pulications [28, 29].

PET data. To demonstrate the use of TCL2 for correcting PET scans for motion artifacts, two of the pediatric PET patients were chosen, patient (a) and (b), for which the tracked motion data indicated rather large motion fluctuations and minor motion fluctuations, respectively. Patient (a) was selected to highlight the effect of MC for large motion while patient (b) was included to confirm that there is no reduction in image quality after MC for patients exhibiting small motion. The patients were scanned using ^{18}F-FET tracer, advantageous in PET imaging for brain tumor suspected patients, with a PET acquisition duration of 40 min. The scans were reconstructed using a dynamic framing, with matrix size 172 × 172 × 127, a Gaussian filter with full width half maximum: 3.5 mm, 3.5 mm, and 5 mm, and with respective frame durations of 6 × 10 s, 4 × 15 s, 2 × 30 s, 2 × 60 s, 2 × 150 s, and 4 × 300 s, resulting in a total of 22 frames for each patient according to our standard clinical procedure. Further for the scans, a static frame from 20-40 min was reconstructed with matrix size 344 × 344 × 127 and a Gaussian filter size of 3.5 mm, 3.5 mm, and 5 mm.

Prospective MRI data. Customized scan sequences supporting motion input were required for prospective MC of MRI. These were not currently available for clinical use. Moreover, prospective reconstruction of MRI disables the possibility of image reconstruction with and without MC for comparison. Therefore, to demonstrate the ability to support prospective MC in MRI, two healthy 24 year old male volunteers were studied in a separate method development study. They were both scanned using the same hybrid PET/MRI scanner as the pediatric patient group, to again demonstrate compatibility of both modalities. Each subject was scanned four times. In two of the scans, subjects were instructed to remain motionless (referred to as a *No motion* case), while in the other two scans they were instructed to perform a repeatable motion pattern during the scan (referred to as a *Motion* case). These four scans were divided into two with- and two without-MC-enabled conditions (referred to as *MC ON* and *MC OFF* cases, respectively). In the motion routine, subject (a) was instructed to do moderate drift-like movements, whereas subject (b) performed large motions to demonstrate the measuring volume of the tracking system. The subjects were scanned using a custom 3D FLASH sequence that can apply prospective MC based on the motion estimates from TracSuite [15], and the motion was tracked using TCL2. The 3D FLASH sequence has the following parameters: FOV 256 mm × 256 mm × 56 mm with 1 mm × 1 mm × 2 mm voxels (phase/read/slice directions respectively), bandwidth of 1000 Hz/pixel, TR of 15 ms, TE of 2.68 ms, and flip angle 35 degrees. A Siemens mMR Head/Neck 16-channel coil was used and no parallel acceleration was applied.

PET motion correction

The PET MC was conducted retrospectively using a customized version of the Multiple Acquisition Frame method incorporating subframes according to the tracked motion. The MC pipeline was implemented around the e7-reconstruction-tools from Siemens. A frame of PET data were chosen from the pool of listmode data. This frame was initially divided into several subframes according to a given threshold of motion (THM), where the individual subframe locations are equal to the patient pose at the given time of acquisition. The attenuation map (μ-map) was repositioned to align the individual subframes. The specified subframing and the aligned μ-map were given as inputs to the e7-tools performing the reconstruction using the ordered subset expectation maximization (OSEM) algorithm [30]. The reconstructed subframes from e7-tools were afterwards rotated and translated according to the motion data to a common pose of a chosen reference frame. Finally, the subframes were merged into a single motion corrected and reconstructed frame, using a duration-weighted average. In case of a dynamic scan, this method was conducted across all the dynamic frames.

The procedure of defining a subframe was constrained to comply with two conditions: A minimum of true counts must be available within the subframe to avoid lack of statistical information, and a THM must be achieved. A lower limit of true counts was found to be 3 million corresponding to a sufficient amount of applicable statistical information and a 2 mm THM was chosen, based on our experience.

Evaluation of PET motion correction. The dynamic PET reconstructions were evaluated with respect to PET tracer distribution over time (i.e. across a sequence of PET frames), where a time-activity curve (TAC) was drawn for the mean radioactivity in a given high uptake region of interest (ROI) with a size of approximately 0.2 cm^3. The tracer uptake in tissue is expressed as standardized uptake value (SUV) by dividing the radioactivity (kBq/mL) in the tissue by the radioactivity injected per gram of body weight [31]. The resulting TACs consists of 22 data points representing mean SUV values for each of the 22 frames in the dynamic reconstruction. This evaluation was conducted for TACs representing reconstruction with and without MC enabled.

For the TACs it was expected to see an increase in SUV, i.e. an increase in image intensity in the given ROI, for the motion corrected images, due to correction for the motion induced artifacts reducing image intensity in high uptake regions. Also a decrease in motion related noise in the TACs reprecenting MC was expected [32].

Prospective MRI motion correction

The TCL2 control unit was connected to the internal MRI scanner Ethernet network. The system control unit sets up an ethernet server, which accepts pose requests from the scanner and replies with the current head pose. The server automatically converts the head poses to the scanner device coordinate system (DCS), before sending them to the scanner. A 3D FLASH sequence was modified to request the current patient head pose from the TCL2 control once per TR. The sequence performs prospective MC every TR by adjusting the gradients, RF pulse frequencies and k-space sample phase every TR, in relation to the changes in the patient's head pose [15].

Cross calibration

For external tracking systems a cross calibration is required, describing the transformation between the tracking coordinate system (TCS) and the scanner DCS. TCL2 returns for each time interval a rigid transformation representing the overall relative motion of the tracked surface. Here, we use the Euler representation for rotations and utilize that a transformation is a

simple multiplication of rotation and translation in homogeneous coordinates. The transformation matrices are of the form

$$\mathbf{A} = \begin{bmatrix} \mathbf{R} & \mathbf{d} \\ 0 & 1 \end{bmatrix}, \tag{1}$$

where $\mathbf{R}$ denotes the 3×3 matrix of rotations and $\mathbf{d}$ is the 3×1 vector of displacements. The cross calibration is described through multiplication of two transformations

$$\mathbf{A}_{\mathrm{DCS2TCS}} = \mathbf{A}_{\mathrm{DCS2PCS}} \mathbf{A}_{\mathrm{PCS2TCS}} , \tag{2}$$

where PCS denotes the coordinate system relative to the patient. The transformation $\mathbf{A}_{\mathrm{DCS2PCS}}$ is defined according to the positioning of the patient in the scanner. In device coordinates of the PET/MRI system, using the head-first-supine patient orientation, this transformation is

$$\mathbf{A}_{\mathrm{PCS2DCS}} = \begin{bmatrix} 1 & 0 & 0 & 0 \\ 0 & -1 & 0 & 0 \\ 0 & 0 & -1 & 0 \\ 0 & 0 & 0 & 1 \end{bmatrix}. \tag{3}$$

The system software provides a semi-automatic cross calibration tool, where a point cloud of the tracked facial surface is first manually repositioned to roughly align to a point cloud of the patient's head extracted from an MRI scan. In these studies a clinical MPRAGE sequence was used with the following parameters: FOV 512 mm × 512 mm × 192 mm with 1 mm × 1 mm × 1 mm voxels (phase/read/slice directions respectively), bandwidth of 179 Hz/pixel, TR of 1900 ms, TE of 2.4 ms, flip angle 9 degrees and an aquisition duration of 5:02 min. Afterwards, the ICP alignment procedure finds a transformation from TCS to PCS, $\mathbf{A}_{\mathrm{PCS2TCS}}$. Prior to scanning, the vision probe can be moved to adjust the FOV to the patient's face. With a mobile system such as TCL2, a cross calibration is required each time the position of the vision probe changes.

For MC application of a tracking device in PET/MRI brain imaging, the rigid transformations describing conversion of tracking in TCL2 coordinates to tracking in scanner device coordinates at time t, is expressed as

$$\mathbf{A}_{\mathrm{DCS}}(t) = \mathbf{A}_{\mathrm{DCS2TCS}} \mathbf{A}_{\mathrm{TCS}}(t) \mathbf{A}_{\mathrm{DCS2TCS}}^{-1} , \tag{4}$$

where $\mathbf{A}_{\mathrm{TCS}}(t)$ describes the transformation of the point cloud in TCL2 coordinates.

Results

PET and MRI compatibility

The motion tracker has been installed and in use with the combined PET/MRI scanner during normal clinical routines for a period of more than two and a half years. In this period, the motion tracker were operated by unsupervised radiographers for the majority of all the examinations. During this period no problems related to compatibility between the scanner and the motion tracker were reported.

Motion tracking data were recorded during the clinical study for all 94 pediatric patients. Out of these 94 examinations, 34 patients received anesthesia during the scan. The average root mean square (RMS) motion of the 34 examinations was 2.00 mm, compared to an average

RMS motion of 5.27 mm for the 60 patients not receiving anesthesia. A t-test shows that the anesthetized patients have significant lower RMS motion with a p-value < 0.001.

The majority of the motion data has been computed with high tracking confidence, as 88 of the scans contain no rejected tracking estimates. The remaining six scans contain one or more rejected tracking estimates due to a low TVP. For five of these cases, the rejected tracking estimates occurred only during rapid motion with a duration for each rejection period never exceeding one second. The number of rejections corresponds to approximately 0.1% of the total number of estimates for these five cases. The final case contains a large proportion of rejected estimates of almost 15%. This loss is primarily caused by substantial motion and a non-optimal reference point cloud containing little information for the alignment procedure.

PET motion correction

Fig 3 shows image slices of a static (single frame) 20-40 min reconstruction of the 40 min dynamic ^{18}F-FET PET scan of patient (a) with and without MC. The reconstruction with MC is conducted using a subframing with a 2 mm THM. The scan shows increased uptake of ^{18}F-FET in a brain tumor in the left hemisphere. Within the scan range from 20 to 40 min, the patient exhibits head movements giving rise to the tumor motion seen from the motion tracking curves for patient (a) in Fig 4. The resulting effect of the MC is an increased intensity in the ROI in already high intensity regions compared to the images reconstructed without MC. This effect matches the expectation, i.e. that patient motion during a PET brain scan will result in images with blurred high intensity regions constituting a larger area with lower intensity, compared to images obtained from scans with no patient motion (cf. [32]). It is noted that in the coronal image slice, another tendency is seen in the upper neck region, however this is not a part of the brain and can not be considered rigid. During the 40 min scan 147 tracking

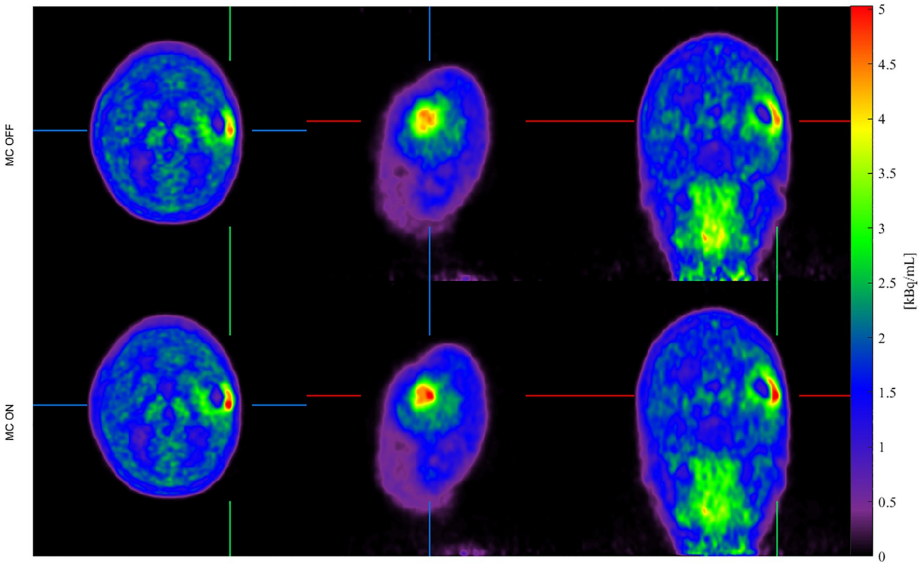

Fig 3. MC of 20-40 min. static PET image of patient (a). Static ^{18}F-FET PET image (20-40 min. after tracer injection) of patient (a). Top-to-bottom rows show axial, sagittal and coronal image slices for image reconstructions without motion correction (left column) and with motion correction (right column). It is seen that the intensity of the tumor has increased after MC is applied.

https://doi.org/10.1371/journal.pone.0215524.g003

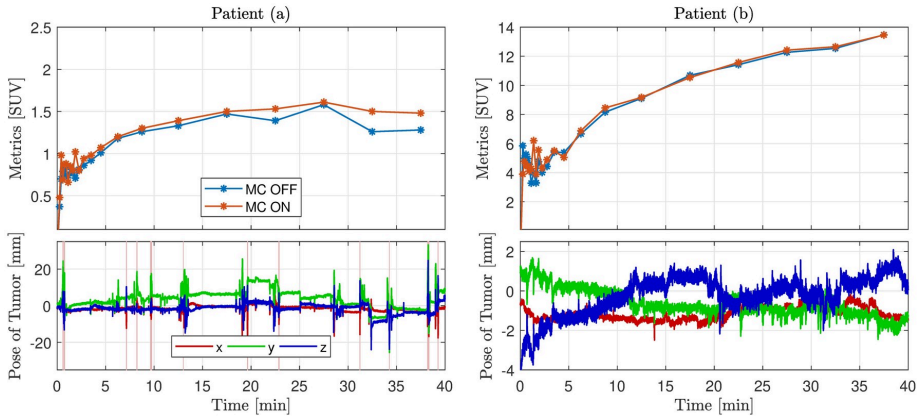

Fig 4. Time-activity curves and tumor motion of patient (a) and (b). Time-activity curves (TACs) and motion tracking curves corresponding to PET patients (a) and (b). For each patient the top plot indicates the TACs representing the mean standardized uptake value in a given tumor region of interest over time (i.e. for the respective dynamic frames). Reconstruction curves with MC and without MC are shown. Each point in a TAC corresponds to the beginning of a frame. The bottom plot shows the motion tracking curves indicating position of the tumor point along the x-, y- and z-axis. 149 tracking estimates are rejected due to low tracking validity for patient (a), marked by the vertical red lines. There are no rejected tracking estimates for patient (b). It is noted that the small rapid fluctuations of the motion curves are caused by respiratory motion as shown in Fig 5.

https://doi.org/10.1371/journal.pone.0215524.g004

estimates were rejected due to low tracking validity. These rejections occur only when the patient moves rapidly and the average total tumor 3D displacement before each rejected interval is 17 mm. None of the rejected estimates are used for the motion compensated image reconstruction.

The TACs for the dynamic reconstruction of the pediatric PET patients are shown in Fig 4 together with the motion of the examined tumor. The TAC represents a tracer increase and washout over time, resulting in a curve rising from the time of injection, and afterwards continuing to rise or decrease depending on the relationship between washout and uptake in the tumor. This curve pattern is seen from all the TACs in Fig 4. However, the motion corrected image for patient (a) yields a more smooth curve, which indicate that motion related noise has been reduced. For patient (b) the differences between MC and no MC are minor in accordance

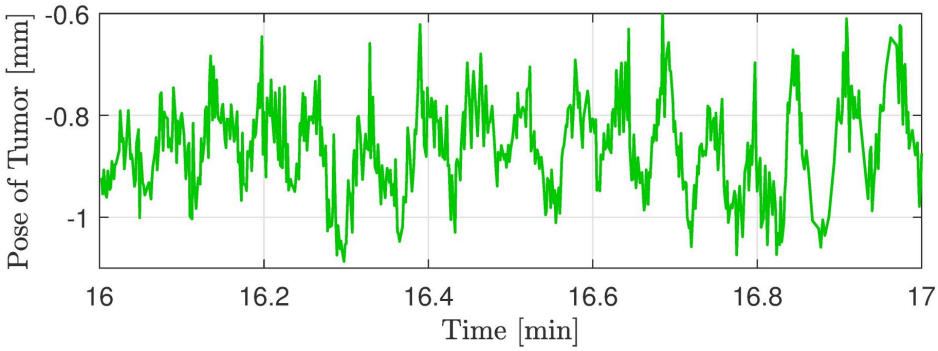

Fig 5. Magnification of tracking curve. Magnification of the y-direction tracking curve from patient (b) seen in Fig 4. The periodic oscillations are the respiratory motion performed by the patient.

https://doi.org/10.1371/journal.pone.0215524.g005

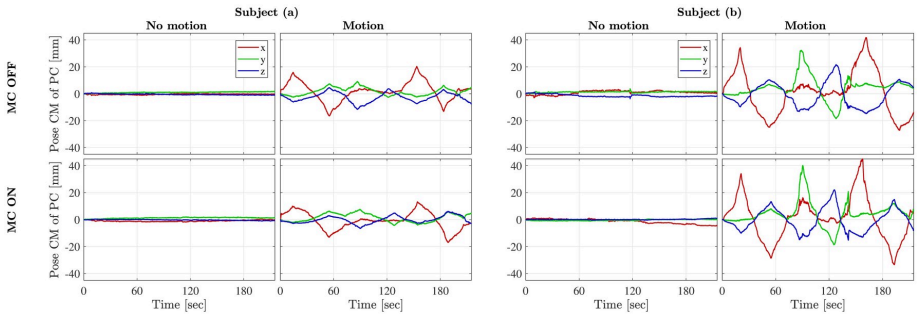

Fig 6. Motion of subject (a) and (b) from the four studied cases. Plots of the position of the center of mass (CM) of the 3D point cloud (PC) representing the motion of subject (a) and (b). The top row corresponds to the scans without motion correction and the bottom row to the scans with motion correction enabled. The plots show that the subjects were able to replicate the motion pattern between the scans with and without motion correction.

https://doi.org/10.1371/journal.pone.0215524.g006

with the small detected motion. The considerable fluctuations of all TACs within the first three minutes can be explained by the low signal-to-noise ratio caused by low frame duration and low tracer uptake resulting in few true counts.

The TAC investigations indicate, that for patient (a), the MC reconstructed image has higher SUV metrics compared to the non-motion corrected image. The frames corresponding to the largest effect of the MC also correspond to time intervals with large motion fluctuations. This substantiates the effect of the MC.

Prospective MRI motion correction

Fig 6 shows the performed motion corresponding to the MRI images of subject (a) and (b) shown in Fig 7. It is noted that the subjects have repeated the motion pattern between the scans with and without MC. Fig 7 shows the axial image slices of the 3D FLASH scan obtained from subject (a) and (b) respectively in the four cases: **A** *No motion, MC OFF*, **B** *Motion, MC OFF*, **C** *No motion, MC ON*, and **D** *Motion, MC ON*. Image **B**, **C** and **D** are all registered to image **A**. In the same figure, absolute difference images are visualized.

Motion artifacts are clearly visible from image **B** for both subjects and are evidently reduced after MC (cf. image **D**). For subject (a), the motion corrected image is similar to the non-motion corrupted image, however some artifacts remain after MC for subject (b) as expected for such large motion. This is reflected in the |**A-D**| images too.

Images for subject (a) in Fig 7 indicate that the TCL2 system is capable of substantially improving image quality with motions up to ±10-15 mm. When subject motions approached ±40 mm, images for subject (b) indicate that only incomplete correction was achieved.

Importantly, we see that the MC does not degrade the quality of scans without motion. This is consistent with what is seen from the difference image |**A-C**| for both of the subjects.

When it comes to *No motion, MC ON*, the differences are negligible, as it is the case for *Motion, MC ON* for subject (a). As shown, deviations are visible in the skull for subject (b) in the *Motion, MC ON* case (cf. difference image |**A-D**|, but reduced in comparison to the *Motion, MC OFF* case (cf. difference image |**A-B**|) for the same subject.

Discussion

We have demonstrated the first markerless motion tracker compatible with simultaneous PET and MRI. The system has been robust for tracking motion in real patients while acquiring

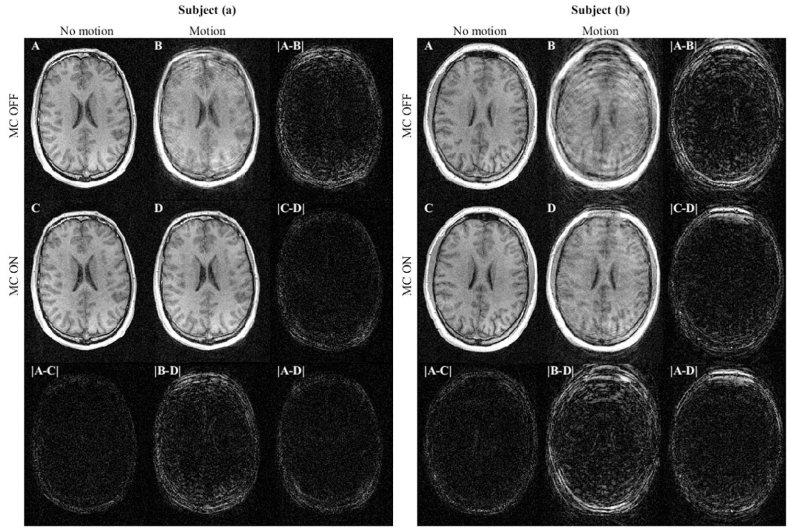

Fig 7. Axial image slices from the 3D FLASH scans of subjects (a) and (b). The motion performed during the acquisition corresponds to the graphs in Fig 6 subject (a) and (b), respectively. The four scan images representing scans with and without motion and with and without motion correction (MC): **A**: *No motion, MC OFF*, **B**: *Motion, MC OFF*, **C**: *No motion, MC ON*, and **D**: *Motion, MC ON*. The absolute difference between scans are present in the last row and column for both subjects. These are visualized using the same mapping from pixel intensities to grey scale values as in the MRI images. For both subjects image **B** show degraded image quality resulting from motion. Image **D** shows the improved image quality as a result of the prospective MC.

https://doi.org/10.1371/journal.pone.0215524.g007

both MRI and PET. Only few cases, where the patients moved rapidly, lead to situations where correct tracking poses could not be estimated. These tracking poses were properly detected by the TVP algorithm. A visual inspection of the point clouds and the rejected transformations for patient(a), confirms that some of these tracking estimates would not represent a correct transformation. In addition, none of the accepted tracking estimates are notably misaligned. In just one of the 94 pediatric scans, a sub-optimal reference point cloud was created leading to additional tracking rejections. A subsequent re-alignment with an updated point cloud improved the TVP, such that 4% of the tracking estimates were rejected instead of 15%. For all other patient scans, only five cases contained rejected tracking estimates, with rejection periods of less than one second each. In total, an acceptance rate of more than 99.9% of all the motion tracking estimates is achieved, indicating the tracking robustness of the motion tracker. The clinical feasibility of the motion tracker is evidenced by the robustness of tracking when the system is operated by radiographers in the normal clinical settings.

Results also show that the motion tracker is feasible for retrospective MC of PET and prospective MC of MRI with notable image improvements. The MC PET study of the two pediatric ^{18}F-FET PET patients with brain tumors demonstrated an enhancement of image contrast after MC in case of ±10 mm motion. In PET imaging no ground truth exists of how the functional images should actually appear, as it is the case in MRI imaging resembling anatomy. This makes it more difficult to quantify the impact of MC, as it was considered unethical to conduct two scans in the included patients, i.e. with and without motion. Nevertheless the time-activity curve and its progress can give a quantitative estimate of the MC. A TAC investigation showed that for large motions, a difference in SUV of up to 19% between the corrected

and non-corrected TACs was detected for certain frames. As an example, further investigation of the patient (a) seen in Figs 3 and 4 led to an increase in SUV values in the ROI after MC, which would change the interpretation of the scan and thereby have an actual impact in the clinical course for the patient in question. In the case of tumor motion in the ±2-3 mm range, e.g. as seen for the patient (b) in Fig 4, the MC pipeline dose not introduce errors related to the MC.

In the MRI study, the motion corrected images were noticeably improved compared to the non-corrected ones. TCL2 was able to track extreme motions, where subject (b) was asked to perform the largest possible motion inside the head coil with a slit width of 6 cm. For subject (b) there were remaining artifacts despite correction for motion. These artifacts are likely in part the result of B_0-field inhomogeneities induced by the extreme head motion, as B_0 field shimming is conducted before each scan assuming no motion within the scan. Additional artifacts may also have been induced by the motion of the subject relative to the B_0 receive fields of the coil elements, which is not accounted for in the prospective motion correction sequence we used. The study also shows, that the impact of MC in the case of no motion is minor, as seen from the difference images $|\mathbf{A}\text{-}\mathbf{C}|$ in Fig 7. The minor differences are likely caused by scan-to-scan variations and small motions despite the subjects' attempt not to move (cf. *No motion* plots of Fig 6).

In the present work we have demonstrated the application of our MC system to 3D FLASH data. This sequence was chosen because of it is a key component of many high-resolution structural imaging protocols, providing both good T1-weighted contrast and low distortion. However, 3D sequences, particularly those whose total scan time extends to minutes, are known to be acutely sensitive to subject motion. As such, this sequence makes a useful exemplar of the efficacy of the TCL2 motion tracker. While the present demonstration is not exhaustive of all the possible ways an optical tracking system such as ours could be used in MRI, other groups have previously employed optical trackers (usually with markers and/or not compatible with PET) for prospective correction. Those results have demonstrated that the direct, prospective correction of the FOV and excitation pulses can reduce motion-induced artifacts in 3D scans using parallel acceleration [33] as well as 2D EPI- and TSE-based sequences [4, 17, 34, 35].

TCL2 demonstrated sufficient sensitivity to detect respiratory motions of size ±0.5 mm, as seen from Fig 5, showing a magnification of the tracking curve for patient (b). This indicates a tracking sensitivity substantially better than the general MRI image resolution. In this relation, investigations of the TCL2 tracking were made. A stationary face phantom was tracked in the mMR Biograph during a similar scan situation to the clinical scans. The tracking curves seen in Fig 8 shows the low tracking noise level of the system. The tracking has maximal fluctuations of ±0.026 mm and a standard deviation of 0.0089 mm. These investigations substantiate the high sensitivity of TCL2 and indicate, that the respiratory fluctuations are in the order of 16 times the noise level. It is noted, that fluctuations of the tracking curve of the z-direction is significantly larger compared to the two other directions. Immediately this is explained by relatively parallel images axes of the vision system with the depth measure almost aligned with the scanner z-direction.

The cross calibration, aligning the tracking and the scanner coordinate systems, is easily conducted with a standard sequence. This makes the system mobile and simple to set up with different kinds of scanners. The FOV of the vision probe is adjusted to fit each patient regarding the wide span of patient size and figure (as an example, some of the pediatric patients do not reach as far into the headcoil and lies further down compared to the adult patients). This procedure takes approximately 10s and is the only additional manual adjustment for each patients. The TCL2 requirement of a cross calibration makes the system dependent on a non

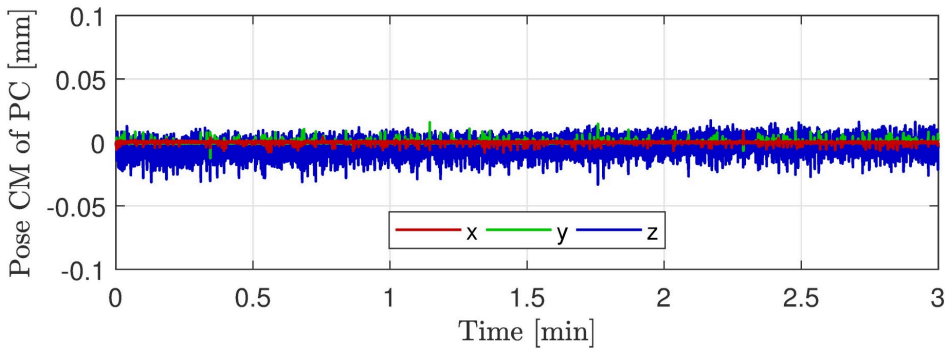

Fig 8. Tracking of stationary face phantom. Tracking curves represented by center of mass of the 3D point cloud (PC) obtained from a TCL2 tracking of a stationary face phantom during an mMR Biograph MRI scan.

https://doi.org/10.1371/journal.pone.0215524.g008

motion corrupted MRI sequence. This dependence could be minimized by introducing a fast acquirable MRI sequence only containing what is essential to the cross calibration. The MPRAGE sequence used in these studies aquire the total head volume, however only image data of the patients's facial surface is necessary as an input to the cross calibration. The scan-time can hence be reduced through reduction of the FOV of the MRI sequence.

In this work an MRI compatible motion tracker has been demonstrated to robustly estimate rigid head motion during MRI, PET, or PET/MRI examinations. The system is designed for head motion tracking, and the motion tracker is therefore only evaluated for brain imaging. However, the tracking system may be able to track motion of other body parts provided that the motion is relative rigid and that the body part has sufficient surface features to allow a unique rigid transformation between a current PC and the reference PC for accurate motion estimation in all directions.

Conclusion

We have presented the TCL2 motion tracker, performing real-time markerless motion tracking and monitoring compatible with both PET and MRI scanners. Design optimization makes the motion tracker feasible for the MRI environment while not compromising PET sensitivity. It is the first time that a motion tracking system has been successfully demonstrated in simultaneous PET/MRI for brain imaging including prospective MC of MRI. For both modalities, a reduction in motion-induced artifacts has been achieved after MC. The system demonstrates robust motion tracking using a TVP to avoid invalid tracking from being used in critical situation such as prospective MC. During the clinical study of 94 pediatric patients, 88 scans had no rejected tracking estimates, while five scans had only minor dropouts. The tracking capabilities of motions ranging from small respiratory motions to the largest possible motion within the MRI head coil have been demonstrated.

Acknowledgments

The authors would like to thank the Department of Clinical Physiology, Nuclear Medicine and PET, Rigshospitalet, University of Copenhagen, Denmark for general support and availability of clinical scanner facilities. They would also like to thank the clinical staff at the department, who collected the tracking data.

Author Contributions

Conceptualization: Jakob M. Slipsager, Oline V. Olesen.

Data curation: Jakob M. Slipsager, Andreas H. Ellegaard, Lisbeth Marner, Otto M. Henriksen, Ian Law, Oline V. Olesen.

Formal analysis: Jakob M. Slipsager, Andreas H. Ellegaard.

Funding acquisition: Lisbeth Marner, Oline V. Olesen.

Investigation: Jakob M. Slipsager, Andreas H. Ellegaard.

Methodology: Jakob M. Slipsager, Andreas H. Ellegaard, M. Dylan Tisdall, Paul Wighton, Oline V. Olesen.

Project administration: Jakob M. Slipsager, Andreas H. Ellegaard.

Resources: Jakob M. Slipsager, Andreas H. Ellegaard.

Software: Jakob M. Slipsager, Andreas H. Ellegaard, Stefan L. Glimberg, M. Dylan Tisdall, Paul Wighton, André van der Kouwe, Oline V. Olesen.

Supervision: Stefan L. Glimberg, Rasmus R. Paulsen, M. Dylan Tisdall, André van der Kouwe, Lisbeth Marner, Otto M. Henriksen, Ian Law, Oline V. Olesen.

Validation: Jakob M. Slipsager, Andreas H. Ellegaard.

Visualization: Jakob M. Slipsager, Andreas H. Ellegaard.

Writing – original draft: Jakob M. Slipsager, Andreas H. Ellegaard, Stefan L. Glimberg, M. Dylan Tisdall, André van der Kouwe.

Writing – review & editing: Jakob M. Slipsager, Andreas H. Ellegaard, Stefan L. Glimberg, Rasmus R. Paulsen, M. Dylan Tisdall, André van der Kouwe, Lisbeth Marner, Otto M. Henriksen, Oline V. Olesen.

References

1. Andre JB, Bresnahan BW, Mossa-Basha M, Hoff MN, Smith CP, Anzai Y, et al. Toward quantifying the prevalence, severity, and cost associated with patient motion during clinical MR examinations. Journal of the American College of Radiology. 2015; 12(7):689–695. https://doi.org/10.1016/j.jacr.2015.03.007 PMID: 25963225
2. Havidich JE, Beach M, Dierdorf SF, Onega T, Suresh G, Cravero JP. Preterm Versus Term Children: Analysis of Sedation/Anesthesia Adverse Events and Longitudinal Risk. Pediatrics. 2016; 137(3):1–9. https://doi.org/10.1542/peds.2015-0463
3. Afacan O, Erem B, Roby DP, Roth N, Roth A, Prabhu SP, et al. Evaluation of motion and its effect on brain magnetic resonance image quality in children. Pediatric radiology. 2016; 46(12):1728–1735. https://doi.org/10.1007/s00247-016-3677-9 PMID: 27488508
4. Maclaren J, Herbst M, Speck O, Zaitsev M. Prospective Motion Correction in Brain Imaging: A Review. Magnetic resonance in medicine. 2013; 69(3):621–636. https://doi.org/10.1002/mrm.24314 PMID: 22570274
5. Zaitsev M, Maclaren J, Herbst M. Motion Artifacts in MRI: A Complex Problem With Many Partial Solutions. Journal of Magnetic Resonance Imaging. 2015; 42(4):887–901. https://doi.org/10.1002/jmri.24850 PMID: 25630632
6. Carson RE, Barker WC, Liow JS, Johnson CA. Design of a Motion-Compensation OSEM List-mode Algorithm for Resolution-Recovery Reconstruction for the HRRT. In: Nuclear Science Symposium Conference Record, 2003 IEEE. vol. 5; 2003. p. 3281–3285.
7. Olesen OV, Sullivan JM, Mulnix T, Paulsen RR, Hojgaard L, Roed B, et al. List-Mode PET Motion Correction Using Markerless Head Tracking: Proof-of-Concept With Acans of Human Subject. IEEE transactions on medical imaging. 2013; 32(2):200–209. https://doi.org/10.1109/TMI.2012.2219693 PMID: 23008249

8. Spangler-Bickell MG, Zhou L, Kyme AZ, De Laat B, Fulton RR, Nuyts J. Optimising rigid motion compensation for small animal brain PET imaging. Physics in Medicine and Biology. 2016; 61(19):7074. https://doi.org/10.1088/0031-9155/61/19/7074 PMID: 27648644
9. Picard Y, Thompson CJ. Motion Correction of PET Images Using Multiple Acquisition Frames. IEEE transactions on medical imaging. 1997; 16(2):137–144. https://doi.org/10.1109/42.563659 PMID: 9101323
10. Tellmann L, Fulton R, Pietrzyk U, Nickel I, Stangier I, Winz O, et al. Concepts of Registration and Correction of Head Motion in Positron Emission Tomography. Zeitschrift für medizinische Physik. 2006; 16 (1):67–74. https://doi.org/10.1078/0939-3889-00293 PMID: 16696372
11. Mukherjee J, Lindsay C, Mukherjee A, Olivier P, Shao L, King M, et al. Improved frame-based estimation of head motion in PET brain imaging. Medical physics. 2016; 43(5):2443–2454. https://doi.org/10.1118/1.4946814 PMID: 27147355
12. Sengupta S, Tadanki S, Gore JC, Welch EB. Prospective Real-Time Head Motion Correction Using Inductively Coupled Wireless NMR Probes. Magnetic resonance in medicine. 2014; 72(4):971–985. https://doi.org/10.1002/mrm.25001 PMID: 24243810
13. Haeberlin M, Kasper L, Barmet C, Brunner DO, Dietrich BE, Gross S, et al. Real-Time Motion Correction Using Gradient Tones and Head-Mounted NMR Field Probes. Magnetic resonance in medicine. 2015; 74(3):647–660. https://doi.org/10.1002/mrm.25432 PMID: 25219482
14. Ooi MB, Krueger S, Thomas WJ, Swaminathan SV, Brown TR. Prospective Real-Time Correction for Arbitrary Head Motion Using Active Markers. Magnetic resonance in medicine. 2009; 62(4):943–954. https://doi.org/10.1002/mrm.22082 PMID: 19488989
15. Wighton P, Tisdall DM, Bhat H, Nevo E, Van der Kouwe A. Slice-by-slice prospective motion correction in EPI sequences;.
16. Maclaren J, Armstrong BS, Barrows RT, Danishad K, Ernst T, Foster CL, et al. Measurement and Correction of Microscopic Head Motion during Magnetic Resonance Imaging of the Brain. PLOS one. 2012; 7(11):e48088. https://doi.org/10.1371/journal.pone.0048088 PMID: 23144848
17. Todd N, Josephs O, Callaghan MF, Lutti A, Weiskopf N. Prospective motion correction of 3D echo-planar imaging data for functional MRI using optical tracking. NeuroImage. 2015; 113:1–12. https://doi.org/10.1016/j.neuroimage.2015.03.013 PMID: 25783205
18. Aksoy M, Maclaren J, Bammer R. Prospective motion correction for 3D pseudo-continuous arterial spin labeling using an external optical tracking system. Magnetic Resonance Imaging. 2017; p. 44–52. https://doi.org/10.1016/j.mri.2017.01.018 PMID: 28137627
19. Maclaren J, Kyme A, Aksoy M, Zahneisen B, Bammer R. Markerless Optical Tracking for Motion Correction in MR and PET/MR Imaging of the Brain;.
20. Schleyer P, Dunn J, Reeves S, Brownings S, Marsden P, Thielemans K. Detecting and estimating head motion in brain PET acquisitions using raw time-of-flight PET data. Physics in medicine and biology. 2015; 60(16):6441–6458. https://doi.org/10.1088/0031-9155/60/16/6441 PMID: 26248198
21. Raghunath N, Faber T, Suryanarayanan S, Votaw J. Motion correction of PET brain images through deconvolution: II. Practical implementation and algorithm optimization. Physics in Medicine and Biology. 2009; 54(3):813–829. https://doi.org/10.1088/0031-9155/54/3/022 PMID: 19131667
22. Kyme A, Se S, Meikle S, Angelis G, Ryder W, Popovic K, et al. Markerless motion tracking of awake animals in positron emission tomography. IEEE transactions on medical imaging. 2014; 33(11):2180–2190. https://doi.org/10.1109/TMI.2014.2332821 PMID: 24988591
23. Miranda A, Staelens S, Stroobants S, Verhaeghe J. Markerless rat head motion tracking using structured light for brain PET imaging of unrestrained awake small animals. Physics in Medicine and Biology. 2017; 62(5):1744. https://doi.org/10.1088/1361-6560/aa5a46 PMID: 28102175
24. Keller SH, Hansen C, Hansen C, Andersen FL, Ladefoged C, Svarer C, et al. Motion correction in simultaneous PET/MR brain imaging using sparsely sampled MR navigators: a clinically feasible tool. EJNMMI physics. 2015; 2(1):2–14. https://doi.org/10.1186/s40658-015-0126-z
25. Olesen OV, Jørgensen MR, Paulsen RR, Højgaard L, Roed B, Larsen R. Structured Light 3D Tracking System for Measuring Motions in PET Brain Imaging. In: SPIE Medical Imaging. vol. 7625. International Society for Optics and Photonics; 2010. p. 76250X.
26. Olesen OV, Paulsen RR, Hojgaard L, Roed B, Larsen R. Motion Tracking for Medical Imaging: A Nonvisible Structured Light Tracking Approach. IEEE transactions on medical imaging. 2012; 31(1):79–87. https://doi.org/10.1109/TMI.2011.2165157 PMID: 21859614
27. Rusinkiewicz S, Levoy M. Efficient Variants of the ICP Algorithm. In: 3-D Digital Imaging and Modeling, 2001. Proceedings. Third International Conference on. IEEE; 2001. p. 145–152.
28. Marner L, Nysom K, Sehested A, Borgwardt L, Mathiasen R, Henriksen OM, et al. Early Postoperative 18F-FET PET/MRI for Pediatric Brain and Spinal Cord Tumors. Journal of Nuclear Medicine. 2019; p. jnumed–118. https://doi.org/10.2967/jnumed.118.220293 PMID: 30683767

29. Ladefoged CN, Marner L, Hindsholm A, Law I, Højgaard L, Andersen FL. Deep learning based attenuation correction of PET/MRI in pediatric brain tumor patients: Evaluation in a clinical setting. Frontiers in neuroscience. 2018; 12. https://doi.org/10.3389/fnins.2018.01005 PMID: 30666184

30. Hudson HM, Larkin RS. Accelerated Image Reconstruction Using Ordered Subsets of Projection Data. IEEE transactions on medical imaging. 1994; 13(4):601–609. https://doi.org/10.1109/42.363108 PMID: 18218538

31. Dunkl V, Cleff C, Stoffels G, Judov N, Sarikaya-Seiwert S, Law I, et al. The Usefulness of Dynamic O-(2-18F-Fluoroethyl)-L-Tyrosine PET in the Clinical Evaluation of Brain Tumors in Children and Adolescents. Journal of nuclear medicine. 2015; 56(1):88–92. https://doi.org/10.2967/jnumed.114.148734 PMID: 25525183

32. Green MV, Seidel J, Stein SD, Tedder TE, Kempner KM, Kertzman C, et al. Head Movement in Normal Subjects During Simulated PET Brain Imaging with and without Head Restraint. Journal of Nuclear Medicine. 1994; 35(9):1538–1546. PMID: 8071706

33. Callaghan MF, Josephs O, Herbst M, Zaitsev M, Todd N, Weiskopf N. An evaluation of prospective motion correction (PMC) for high resolution quantitative MRI. Frontiers in neuroscience. 2015; 9:97. https://doi.org/10.3389/fnins.2015.00097 PMID: 25859178

34. Herbst M, Maclaren J, Weigel M, Korvink J, Hennig J, Zaitsev M. Prospective motion correction with continuous gradient updates in diffusion weighted imaging. Magnetic resonance in medicine. 2012; 67 (2):326–338. https://doi.org/10.1002/mrm.23230 PMID: 22161984

35. Zaitsev M, Akin B, Levan P, Knowles BR. Prospective motion correction in functional MRI. NeuroImage. 2017; 154:33–42. https://doi.org/10.1016/j.neuroimage.2016.11.014 PMID: 27845256

Appendix C

Paper III

Slipsager JM, Glimberg SL, Højgaard L, Paulsen RR, Wighton P, Tisdall D, Jaimes C, Gagoski BA, Grant PE ,van der Kouwe A ,Olesen OV, Frost R. *Comparison of prospective and retrospective motion correction in 3D-encoded neuroanatomical MRI.* Accepted for publication in Magnetic Resonance in Medicine.

Comparison of Prospective and Retrospective Motion Correction in 3D-encoded Neuroanatomical MRI

Jakob M. Slipsager[*†‡§], Stefan L. Glimberg[‡], Liselotte Højgaard[†], Rasmus R. Paulsen[*], Paul Wighton[§], M. Dylan Tisdall[¶], Camilo Jaimes[‖**], Borjan A. Gagoski[**††], P. Ellen Grant[**††], André van der Kouwe[§**], Oline V. Olesen[*†‡], Robert Frost[§**]

[*]DTU Compute, Technical University of Denmark, Denmark

[†]Dept. of Clinical Physiology, Nuclear Medicine & PET, Rigshospitalet, University of Copenhagen, Denmark

[‡]TracInnovations, Ballerup, Denmark

[§]Athinoula A. Martinos Center for Biomedical Imaging, Massachusetts General Hospital, Charlestown, Massachusetts

[¶]Dept. of Radiology, Perelman School of Medicine, University of Pennsylvania, Philadelphia, Pennsylvania

[‖]Boston Children's Hospital, Boston, Massachusetts

[**]Dept. of Radiology, Harvard Medical School, Boston, Massachusetts

[††]Fetal-Neonatal Neuroimaging & Developmental Science Center, Boston Children's Hospital, Boston, Massachusetts

***Abstract*—To compare prospective motion correction (PMC) and retrospective motion correction (RMC) in Cartesian 3D-encoded MPRAGE scans and to investigate the effects of correction frequency and parallel imaging on the performance of RMC.**

Head motion was estimated using a markerless tracking system and sent to a modified MPRAGE sequence which can continuously update the imaging FOV to perform PMC. The prospective correction was applied either before each echo-train (Before-ET) or at every sixth readout within the echo-train (Within-ET). RMC was achieved by adjusting k-space trajectories according to the measured motion during image reconstruction. The motion correction frequency was retrospectively decreased or increased through RMC or reverse RMC. Phantom and in vivo experiments were used to compare PMC and RMC, and to compare Within-ET and Before-ET correction frequency during continuous motion. The correction quality was quantitatively evaluated using the structural similarity index measure using a reference image without motion correction and without intentional motion.

PMC resulted in superior image quality compared to RMC both visually and quantitatively. Increasing the correction frequency from Before-ET to Within-ET reduced motion artifacts in RMC. A hybrid PMC and RMC correction, i.e. retrospectively increasing the correction frequency of Before-ET PMC to Within-ET also reduced motion artifacts. Inferior performance of RMC compared to PMC was shown with GRAPPA calibration data without intentional motion, and without any GRAPPA acceleration.

Reductions in local Nyquist violations with PMC resulted in superior image quality compared to RMC. Increasing the motion correction frequency to Within-ET reduced motion artifacts in both RMC and PMC.

I. Introduction

Head motion is an ongoing problem in MR imaging of the brain, causing artifacts that reduce clinical image quality and introduce bias and variance in research results [1, 2]. In the clinic, sequences may be repeated to ensure images with sufficient quality are obtained for diagnostic use, but at the expense of prolonged examination times and increased financial cost. Andre et al. [3] showed that in 19.8% of the MRI examinations they studied it was necessary to repeat at least one of the sequences, adding an estimated extra cost of $115,000 per scanner per year. In pediatric MRI examinations, sedation or anesthesia are commonly used to mitigate motion, but these methods are associated with increased health risk and additional costs [4, 5]. In a recent study the estimated annual cost of pediatric anesthesia in MRI examinations was $319,000 per scanner [6].

To reduce the negative effects of head motion, several motion correction (MC) strategies have been proposed. Overall, MC techniques can be divided into either prospective motion correction (PMC) or retrospective motion correction (RMC).

In PMC, the correction is performed by modifying the acquisition as data is acquired. This requires continuous, low latency estimation of the rigid body position and orientation (pose) of the patient's head throughout the scan. These estimates are used to dynamically adjust the encoding field-of-view (FOV) to keep it stationary relative to the patient's head [7, 8]. The different approaches to estimate head motion can be divided into MR-based "navigator" techniques, and external systems that require some additional hardware. Navigators are sequence modules embedded in the parent sequence that acquire additional data for motion estimation, and with some common methods a new motion estimate is provided every few seconds [9–13]. There are also various self-navigated approaches that estimate head motion directly from the acquired imaging data [14–18]. In contrast, external tracking systems use additional hardware, either MR or optical (e.g. cameras, light sources, and markers) to estimate motion at a temporal scale in the

millisecond range [19–26] .

RMC covers a large group of strategies, where the correction of motion takes place after the data acquisition is complete. Methods working in the k-space domain, use the estimated motion to update the k-space trajectory in the image reconstruction [12, 27]. The k-space trajectory can also be updated without explicitly measuring the motion. Early methods iteratively corrected the acquired data to optimize image quality measures (e.g. entropy or gradient entropy) [28, 29]. Recent methods estimate motion from the data itself using the motion information encoded in the multiple receiver coils [15, 16].

Some of the advantages of RMC are that it preserves the original uncorrected image and it is not dependent on receiving real-time motion measurements with low latency. However, RMC is less effective in 2D multi-slice segmented sequences when there is through-slice motion between segments [30]. 3D-encoded acquisitions also suffer from k-space under-sampling in the presence of head rotations [8] which lead to violation of the Nyquist criterion and cannot be compensated by RMC using the non-uniform Fourier transform to reconstruct the irregularly-sampled k-space. In principle, prospective correction of the acquisition will sample k-space as intended and thereby avoid such gaps in k-space. For this reason, PMC is expected to be less susceptible to under-sampling artifacts, although to date, this has not been shown empirically.

In the context of recent developments for RMC in 3D-encoded MRI [12, 17, 18, 31], the first aim of this work was to compare the motion correction performance of PMC and RMC in 3D-encoded structural MRI of the brain. Previously, navigator and optical tracking modalities have been compared for retrospective correction of involuntary motion in high-resolution structural sequences [32]. Also, prospective correction with NMR field probes versus optical tracking [33] has been compared. In this study, we directly compare retrospective and prospective correction in Cartesian 3D-encoded MPRAGE with the same markerless optical tracking [25, 26, 34].

The second aim was to investigate the effect of the correction frequency on the encoding error and the performance of RMC. Increasing the correction frequency of PMC in 3D MPRAGE has previously been shown to reduce image artifacts [26]. RMC was used to retrospectively increase and decrease the correction frequency of the acquired data.

Finally, experiments were performed to investigate the effects of GRAPPA calibration and reconstruction in comparisons between PMC and RMC. Parallel imaging is routinely used to accelerate 3D-encoded MRI acquisitions. However, differences in performance between RMC and PMC could be due to motion-related effects on the calibration and parallel imaging reconstruction. The use of GRAPPA auto-calibration signal (ACS) data without intentional motion from a pre-scan was compared with integrated ACS. Furthermore, comparisons of PMC and RMC were performed without any GRAPPA acceleration – this removes the GRAPPA confound in performance comparisons and leaves only the effect of k-space undersampling due to rotation.

II. Methods

A. Motion tracking

Rigid-body head motion was estimated using a 2nd generation of the markerless tracking system [35] Tracoline TCL3.1 (TracInnovations, Ballerup, Denmark) [25, 26]. The TCL3 system was placed behind the scanner and the vision probe containing the non-electronic system optics was attached to the scanner table. The probe was positioned to have an unobstructed line of sight to the subject's face through the 64-channel head coil (Siemens Healthineers, Erlangen, Germany). The TCL3 system estimates motion by capturing 3D surface scans of the subject's face at a rate of 30 Hz using near-infrared structured light. Head motion is estimated by computing the rigid body transformation that maps the current surface scan back to the initial reference surface. TCL3 uses an iterative closest point algorithm to estimate the rigid body transformation between the surface scans [35].

A geometric calibration between the scanner and the TCL3 system is necessary to represent the estimated motion in the coordinate system of the scanner. For retrospective correction, a temporal calibration is also required. The geometric alignment consists of a cross-calibration where the reference surface scan of the subject is matched to a surface extracted from a structural MRI calibration scan [36]. The subjects were asked to remain still during the cross-calibration scan and this was verified with the tracking. The cross-calibration results in a transformation ${}_{scs}\mathbf{A}_{tcs}$ between the scanner coordinate system (scs) and the TCL3 coordinate system (tcs).

The temporal calibration was achieved by a time synchronization between the TCL3 computer and the host computer of the scanner. Both calibration steps were performed before each scan session.

B. Prospective motion correction

PMC was enabled by modifying a Cartesian 3D-encoded MPRAGE sequence to adjust the imaging field of view (FOV) according to motion estimates received from the TCL3 system [26]. To examine the effect of the update frequency on the correction performance, two different versions of the PMC MPRAGE sequences were tested [26]. In the first version, referred to as Before-ET-PMC, the FOV was updated before each ET, with ETs 2500 ms apart. In the second version, referred to as Within-ET-PMC, the FOV was updated before each ET and every six readouts (48 ms update interval) within the ET.

C. Retrospective motion correction

RMC was performed on an external computer using a modified version of the freely available retroMoCoBox software package [37] and consists of the following steps:

1) Reconstruction of missing k-space lines due to GRAPPA acceleration [38].
2) Each k-space readout is temporally matched to the nearest available motion estimate recorded by the tracking device. As a result, each readout is then assigned a 4x4 homogeneous transformation matrix ${}_{tcs}\mathbf{T}_{tcs}(e, r)$.

The transformation matrix encodes the head pose of the subject at the r'th readout in the e'th ET relative to a reference position of the subject.

3) The assigned motion is transformed into scanner's coordinate system (scs) using the cross-calibration ${}_{scs}\mathbf{T}_{scs}\left(e,r\right) = {}_{scs}\mathbf{A}_{tcs}\ {}_{tcs}\mathbf{T}_{tcs}(e,r)\ {}_{scs}\mathbf{A}_{tcs}^{-1}$.
4) Translations are corrected by adding additional phase ramps to each k-space readout using the assigned translation parameters.
5) Correction of rotations is done by rotating each k-space line according to the assigned rotations.
6) An implementation of the non-uniform fast Fourier transformation (NUFFT) running on the GPU [39] is used to reconstruct the image since k-space is no longer uniformly sampled as a result of the k-space trajectory correction.

RMC was also applied to data acquired with Before-ET-PMC to retrospectively increase the motion correction frequency during echo-trains. This hybrid motion correction (HMC) strategy could be termed Within-ET-HMC. This was done by passing the raw data from the Before-ET-PMC scan through the RMC pipeline to correct for residual motion that occurred when the subject moved during an echo-train (See Supporting Information Figure S 1). The residual motion $\mathbf{T}_{res}$ was determined by

$$\mathbf{T}_{res}\left(e,r\right) = \mathbf{T}^{-1}\left(e,0\right)\mathbf{T}\left(e,r\right), \tag{1}$$

where $\mathbf{T}\left(e,0\right)$ is the transformation that was used to update the FOV before the e'th ET and $\mathbf{T}(e,r)$ is a recorded transformation at the r'th readout in the e'th ET.

"Reverse" MC was performed on PMC data [27, 40], to create "uncorrected" versions of both Within-ET and Before-ET PMC scans. Raw k-space data acquired with PMC were passed through the RMC pipeline. The k-space trajectory was reverse corrected with the inverted motion estimates that were used to update the FOV in real-time.

Finally, reverse motion correction was used to reconstruct Before-ET images based on Within-ET PMC data. Here, the k-space trajectory was reverse corrected by the difference between the Within-ET and the Before-ET transformations. This set of transformations were determined by

$$\mathbf{T}_{res}\left(e,r\right) = \mathbf{T}^{-1}\left(e,r\right)\mathbf{T}\left(e,0\right), \tag{2}$$

D. Data acquisition and reconstruction

Data in this work were acquired on a 3 T Prisma scanner (Siemens Healthineers, Erlangen, Germany) using a 64-channel head coil. All MPRAGE sequences used in the experiments had the following protocol: FOV=256x256 mm^2, matrix=256x256, 176 1 mm sagittal slices, in-plane GRAPPA R=2, TR=2500 ms, TE=3.3 ms, TI = 1070 ms, bandwidth=240 Hz/px, echo spacing=8 ms, and turbo factor=176. The scan time was 5:59 min with integrated GRAPPA ACS acquisition and 5:19 min with external ACS. A subset of the MPRAGE scans were acquired without GRAPPA acceleration. The scan time was kept to 6:02 min by modifying the following parameters: FOV=240x225.6 mm^2, matrix=192x180, TR=2000.

E. Image reconstruction

To avoid any potential differences between the reconstruction running on the scanner and the offline RMC reconstruction, all data were transferred to an external computer and reconstructed using the RMC reconstruction pipeline. For the reconstruction of PMC images, the acquired raw data were reconstructed with the RMC pipeline, but the k-space trajectory was updated with the identity matrix instead of real motion estimates, as illustrated in Fig. 1A. Reconstruction of RMC and uncorrected images is illustrated in Fig. 1B. Here the k-space trajectory was updated either with motion estimates recorded during the scan for RMC images, or with the identity matrix for uncorrected images.

F. GRAPPA calibration and reconstruction

The relevance of GRAPPA to the comparison of PMC and RMC is that commonly-used RMC based on Gallichan et al. [12] estimates the GRAPPA weights and reconstructs missing k-space data before any motion correction. The autocalibration signal (ACS) data [38] for GRAPPA-accelerated MPRAGE is typically integrated into the acquisition by fully sampling central k-space lines, but alternatively, can be acquired in an external FLASH pre-scan. Hence, with integrated ACS acquisition, motion during the ACS region is expected to corrupt both the estimation of GRAPPA weights and the reconstruction of missing k-space data. Alternatively, if we arrange an "ideal" external ACS acquisition without intentional motion, the GRAPPA weights can be estimated accurately, but we expect that the reconstruction of missing k-space still suffers from applying a "correct" GRAPPA kernel to irregularly sampled k-space lines that are phase-shifted or rotated by rigid motion.

RMC using the external ACS option was compared with using integrated ACS. The integrated ACS images have higher signal-to-noise ratio than external ACS images, because the extra ACS k-space data are used in the reconstruction instead of estimated. Hence, for controlled comparisons with external ACS images, the integrated ACS k-space lines were not used in the reconstructed images, i.e., they were only used to calculate the GRAPPA weights.

To remove the confound of GRAPPA in the comparison of PMC and RMC, experiments without GRAPPA acceleration were also performed.

G. Experiments

Phantom and in vivo experiments were performed to investigate the correction performance of PMC and RMC and to assess the effect of correction frequency on the performance during continuous motion. A summary of the performed experiments is given in Table I. As a gold standard for the image quality, an uncorrected reference scan without intentional motion was acquired for every subject.

The in vivo experiments were performed on six healthy volunteers, who were scanned in accordance with Institutional Review Board guidelines. Before each scan session, the volunteers were trained to move their heads in a repeatable

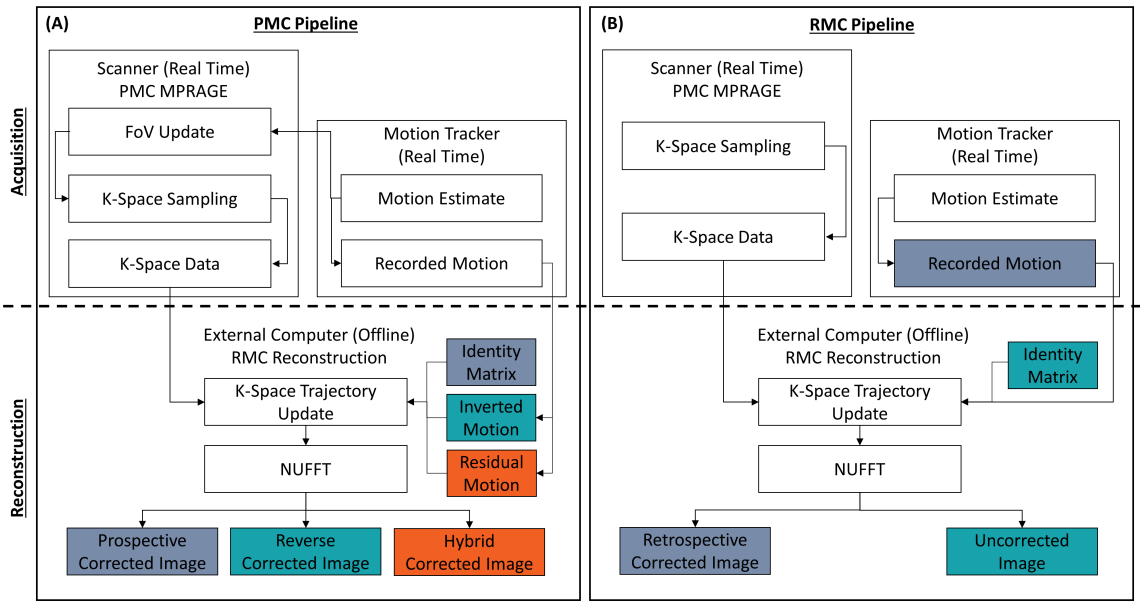

Fig. 1. Flow chart showing the data acquisition and reconstruction pipeline used to generate images without motion correction (MC), with prospective MC (PMC), retrospective MC (RMC), reverse MC, and hybrid PMC and RMC. Matching colors illustrate what type of motion a given image was corrected by. The non-uniform fast Fourier transform (NUFFT) was used to reconstruct the images in all cases. (A) Shows the pipeline for PMC data. The PMC takes place on the scanner, where the field of view (FOV) is updated. The hybrid and the reverse correction were performed during the reconstruction on an external computer. (B) Shows the pipeline for both RMC and without MC. The trajectory of the acquired k-space data was updated with the recorded motion and with the identity matrix to generate the RMC and uncorrected images, respectively.

pattern in order to obtain PMC data and uncorrected data (for RMC) corrupted by similar motion. Subjects did not have head padding so they could move and maintain a head pose without having to strain against the padding. Similar motion across compared scans could be qualitatively confirmed from motion plots on the TCL3 display. MPRAGE scans using Within-ET PMC and no MC (for RMC) were carried out for every subject.

H. Comparison of PMC and RMC in vivo experiments

In session one, the performed pattern was discrete, abrupt motion, where the volunteer changed head position (look right, up, left, down, back to center) at 1-minute intervals. In scan session two, the performed pattern was periodic, continuous motion. Here, for a 1-minute period that started 2 minutes into the sequence the volunteer continuously changed head position by looking left to right. In session one and two, the pattern was performed with a medium and high motion amplitude. The maximum amplitude of deviation in scanner coordinates from the starting positions were: $\sim$2.5 mm and $\sim$5° for medium discrete motion; $\sim$5 mm and $\sim$10° for large discrete motion; $\sim$1.5 mm and $\sim$3° for medium continuous motion; $\sim$2.5 mm and $\sim$5° for large continuous motion. Motion plots are provided along with each image comparison. In session three, both the discrete and periodic continuous motion patterns were tested in separate scans.

I. Motion correction frequency phantom experiments

A pineapple was placed in a mechanical device that was able to rotate the pineapple around the scanner's vertical y-axis. The pineapple was continuously moved back and forth for 1 minute with maximum amplitude of deviation in scanner coordinates from the starting positions of $\sim$5 mm and $\sim$3.5°. This motion was reproduced as consistently as possible during MPRAGE scans with no MC, Before-ET PMC, and Within-ET PMC. This procedure was performed for three motion onset times, with the motion period beginning at approximately 0, 1, and 2 minutes into the MPRAGE scans (see Supporting Information Figure S 2). The recorded motion for the 2 minute motion onset time is shown in Fig. 5 in the coordinate system of the scanner.

J. Motion correction frequency in vivo experiments

Scan session two was designed to investigate the effect of update frequency on motion correction performance and thus, Before-ET PMC scans were also acquired in session two.

TABLE I. LIST OF THE PERFORMED EXPERIMENTS.

Session	Motion Pattern	Experiments	Performed Sequences
Phantom	Continuous	Three experiments were performed, where the motion period began 0, 1, and 2 minutes into the sequence.	3 x No MC 3 x Before-ET-PMC 3 x Within-ET-PMC
Subject 1	Discrete	The pattern was performed with medium and high motion amplitude.	2 x No MC 2 x Within-ET-PMC
Subject 2	Continuous	The pattern was performed with medium and high motion amplitude.	2 x No MC 2 x Before-ET-PMC 2 x Within-ET-PMC
Subject 3	Discrete Continuous	Both the discrete and the continuous motion patterns were performed.	2 x No MC 2 x Within-ET-PMC
Subject 4	Discrete	The pattern was repeated in all 3 scans.	1 x No MC, External ACS 1 x No MC, Integrated ACS 1 x Within-ET-PMC, External ACS
Subject 5	Continuous	The pattern was repeated in all 3 scans.	1 x No MC, External ACS 1 x No MC, Integrated ACS 1 x Within-ET-PMC, External ACS
Subject 6	Discrete Continuous	Both the discrete and the continuous motion patterns were performed.	2 x No MC, No GRAPPA 2 x Within-ET-PMC, No GRAPPA

K. GRAPPA calibration in vivo experiments

Scan sessions four and five investigated the effect of using integrated versus external acquired GRAPPA calibration data on the quality of RMC during discrete and continuous motion. The volunteers did not move intentionally during the external ACS acquisitions at the start of the scan.

L. In vivo experiments without GRAPPA acceleration

In scan session six the potential confounds related to GRAPPA were removed by comparing PMC and RMC in unaccelerated acquisitions, leaving only effects related to k-space undersampling. Discrete and continuous motion patterns were tested.

M. Quantification of motion

Image encoding errors were quantified by calculating the discrepancy between the encoded FOV and the estimated true FOV (based on the pose from the motion tracker) at each k-space readout [26]. At each readout r in each ET e, the true and the encoded positions can be described by a 4x4 transformation matrix $\mathbf{T}_{true}(e,r)$ and $\mathbf{T}_{encode}(e,r)$, respectively. The discrepancy $d(e,r)$ between encoded and true positions was determined as the average voxel displacement deviation over a 64 mm-radius sphere [41]. The discrepancy over the entire sequence is quantified as the RMS discrepancy by

$$RMS_{discrepancy} = \sqrt{\frac{1}{ER}\sum_{e=1}^{E}\sum_{r=1}^{R} d\left(e,r\right)^2}, \qquad (3)$$

where R is the number of readouts in an ET and E is the number of ETs. The head motion in each scan was also quantified using the RMS discrepancy. The discrepancy $d(e,r)$ was calculated between the recorded $\mathbf{T}_{recorded}(e,r)$ motion and the identity matrix.

N. Quantification of image quality

Image quality was quantified relative to an uncorrected image without intentional motion (reference image) recorded in each scan session. Rigid registration with the Insight Toolkit [42, 43] was performed on each image volume within a session using the reference image as the fixed volume. The background of each volume was removed by a mask created from the reference image. The structural similarity index measure (SSIM) [44] between the foreground of the evaluated image and the reference image was used as a measure of the image quality.

III. RESULTS

A. Image quality comparison of prospective and retrospective correction

Comparisons of image quality during discrete and continuous head motion are shown in Fig. 2 and 3 respectively, together with the recorded head motion. Results from scan session 3 are shown in Supporting Information Figure S 3. Both PMC and RMC provide improved image quality compared to the uncorrected scans. A direct comparison of the images in the medium amplitude discrete motion cases in Fig. 2B shows that the PMC image is marginally better than the RMC image which is more blurred and has less contrast. However, in the case of large discrete motion (Fig. 2B and Supporting Information Figure S 3B), the PMC image quality is substantially better than for the corresponding RMC images. In the periodic continuous motion experiments (Fig. 3B and

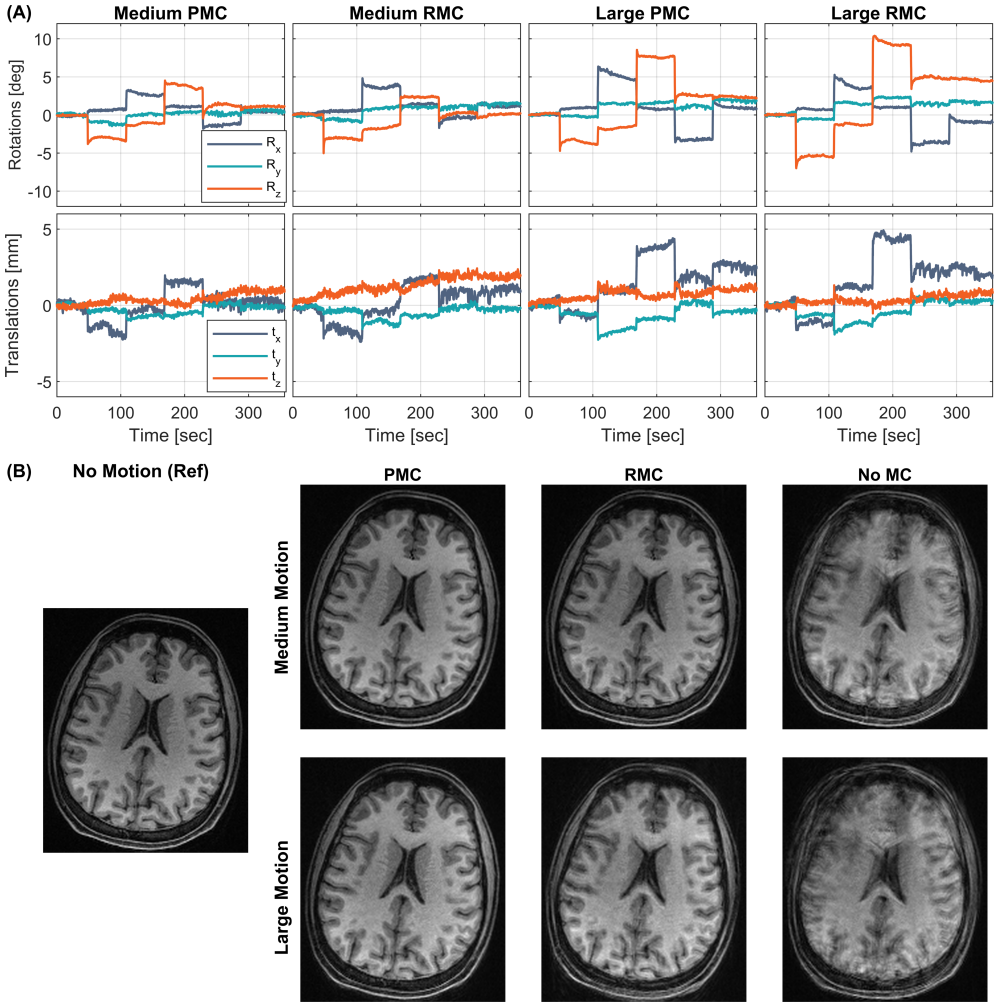

Fig. 2. In vivo comparison of within echo train (Within-ET) PMC, Within-ET RMC, and no MC during scans with discrete motion with medium and large amplitude (Subject 1). (A) The motion measurements during the four scans. (B) MPRAGE image reconstructions from scans with medium and large motion with PMC, RMC, and no correction. The leftmost MPRAGE image was acquired in a scan with no motion and without motion correction and was used as a reference for image quality. PMC: prospective motion correction; RMC retrospective motion correction; no MC: without motion correction.

Supporting Information Figure S 3B) more artifacts are evident in RMC than in the PMC images. The three volunteers were able to repeat similar motion patterns in nearly all scans. However, in the case of large discrete (subject 1) and continuous (subject 3) motion, there is lower motion amplitude during the PMC scans than in the uncorrected scans used for RMC.

The magnitude of k-space data after no MC, PMC, and RMC during high amplitude discrete and continuous motion are shown in Supporting Information Figure S 4 demonstrating that k-space after RMC contains under- and over-sampled regions. This effect is seen from both types of motion pattern, but it is most notable in the discrete motion case.

Figure 4 shows the image quality as measured by SSIM plotted as a function of the RMS discrepancy during the corresponding motion. The image quality is reduced (lower SSIM) when the motion increases in nearly every case. It is also seen that both PMC and RMC results in higher SSIM compared to the uncorrected images, however, PMC results in the highest SSIM in every case. In the scan corrupted by large continuous motion (subject 2), RMC resulted in a slightly

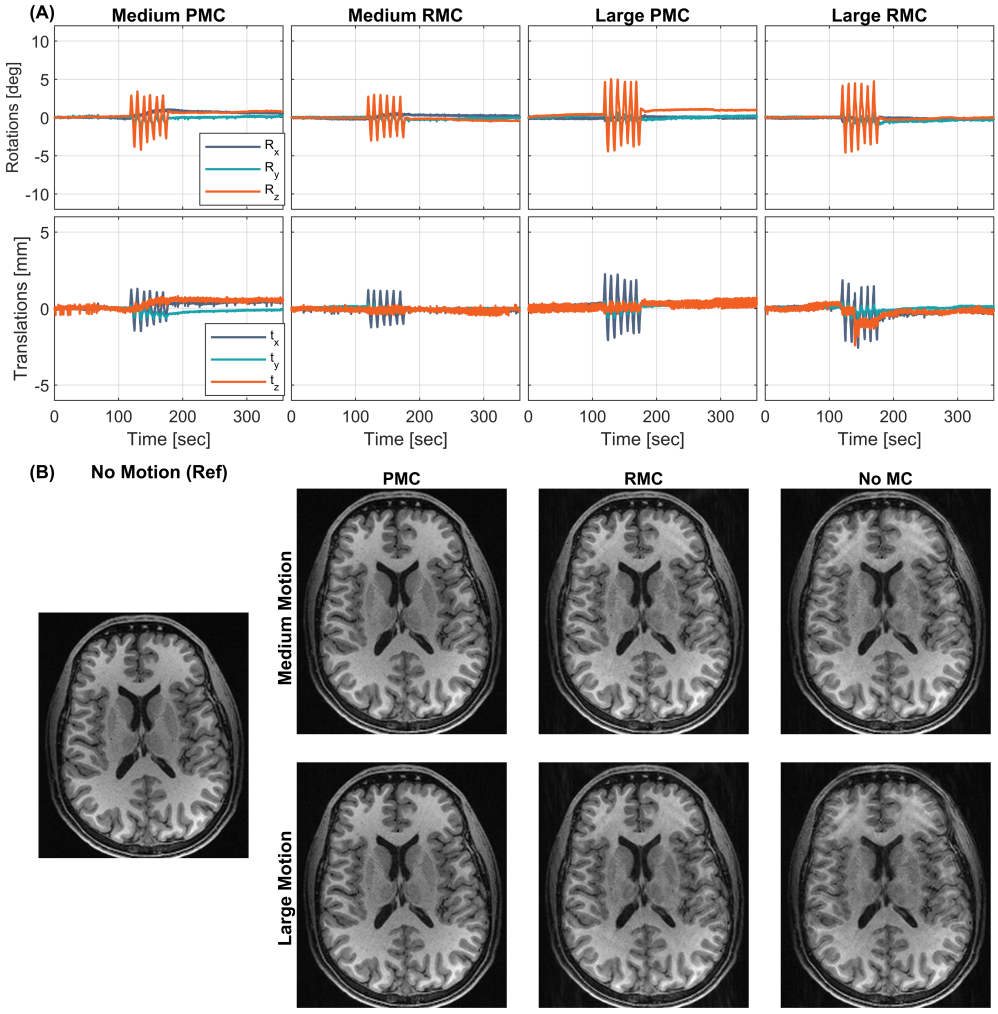

Fig. 3. In vivo comparison of within echo train (Within-ET) PMC, Within-ET RMC, and no MC during periodic continuous motion with medium and large amplitude (Subject 2). (A) The motion measurements during the four scans. (B) MPRAGE image reconstructions from scans with medium and large motion, with PMC, RMC, and no correction. The leftmost MPRAGE image was acquired in a scan with no motion and without motion correction and was used as a reference for image quality. PMC: prospective motion correction; RMC retrospective motion correction; no MC: without motion correction.

lower SSIM compared to the uncorrected image, despite a visual improvement in sharpness and contrast (see Fig. 3B, bottom row).

B. Effect of FOV correction frequency on RMC image quality.

The recorded motion estimates and images from the phantom experiments with motion onset at 0, 1, and 2 minutes into the sequence are shown in Supporting Information Figure S 2. Images acquired during motion starting 2 minutes into the sequences are shown in Fig. 5A. Images along the diagonal were acquired with PMC off, Before-ET PMC, and Within-ET PMC and reconstructed without RMC. Images outside the diagonal are retrospectively corrected or reverse corrected versions of the images in the diagonal. Thus, there are three reconstructed images for each acquired scan. Both RMC and PMC before each ET increase image quality (column 2, rows 1 and 2). Increasing the update rate to Within-ET MC results in even better image quality for data acquired with PMC

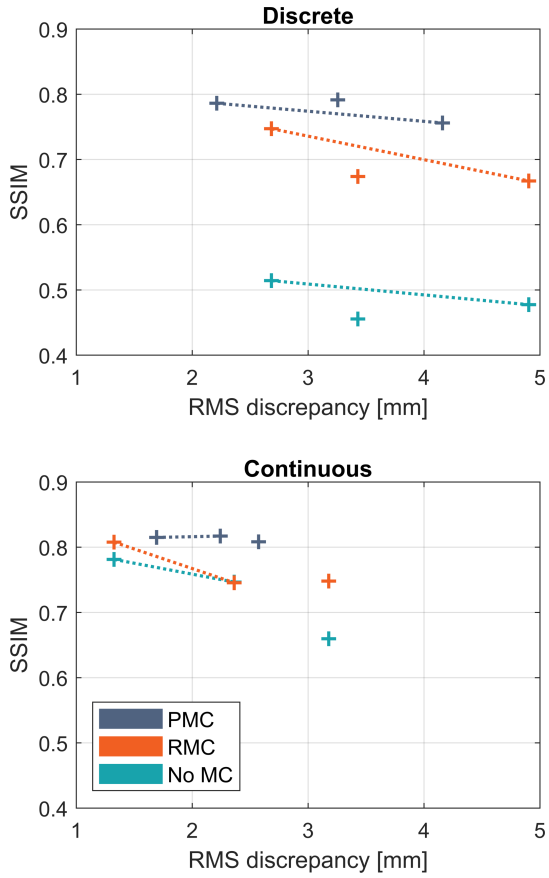

Fig. 4. Quantitative comparison of the correction performance of Within-ET PMC and Within-ET RMC during discrete and continuous motion. The structural similarity index measure (SSIM) relative to a scan without motion correction and intentional motion is plotted as a function of RMS discrepancy between the recorded motion and no motion (identity matrix). Connected points correspond to experiments with the same motion correction but with varied amplitude of motion. PMC: prospective motion correction; RMC retrospective motion correction; no MC: without motion correction.

off and Before-ET PMC, as seen from rows 1 and 2 in column 3. Retrospectively updating the Before-ET PMC scan to Within-ET correction resulted in similar quality to the native Within-ET PMC scan (column 3, rows 2 and 3). The same retrospective correction and reverse correction schemes were applied to the phantom experiments with motion starting 0 and 1 minute into the sequences. These experiments show similar results to the experiment with motion starting at 2 minutes, but with fewer motion artifacts in the uncorrected images and therefore less-notable effects of MC were seen.

The same retrospective correction scheme was applied to the in vivo experiments with periodic continuous motion (subject 2). The recorded motion and reconstructed images are shown in Fig. 6 for the high motion amplitude experiment, where each row corresponds to a scan. The in vivo experiments show similar results as the phantom experiments, where Within-ET correction (both PMC and RMC) provides images with the best quality. However, in the in vivo experiments the best quality was provided by the PMC, while RMC resulted in lower visual quality. The quality of the combined PMC and RMC falls between the PMC and RMC.

In both the phantom and in vivo experiments, the discrepancy between the true motion and the encoded motion was used as a measure of the encoding error of the correction. Supporting Information Figure S 1 shows the discrepancy of rotation around the z-axis for the in vivo experiment with medium amplitude. Within-ET MC resulted in the lowest discrepancy, and Before-ET MC reduced the discrepancy compared to no MC.

In Fig. 7 the SSIM is plotted as a function of the RMS discrepancy for every acquired, retrospectively corrected, and reverse corrected image. k-Space data acquired with PMC off, Before-ET PMC, and Within-ET PMC are labeled with a blue marker. Images reconstructed from the same k-space data are connected and data points with the same color were corrupted by similar motion patterns and amplitudes. The phantom experiments (Fig. 7A) show that when motion occurred early in the scan, the image quality was better than compared to scans where the motion was applied in the middle (closer to the center of k-space). Secondly, Within-ET MC images have the best quality, while Before-ET MC resulted in lower quality. For a given motion onset time, image quality increases when correction frequency increases with PMC, RMC, or hybrid MC. With reverse RMC, image quality decreases when the correction frequency is reduced. The same tendencies are seen in the in vivo experiments, except in the case of high amplitude with Before-ET RMC, which resulted in lower quality compared to the uncorrected image.

C. GRAPPA-related effects

The results of using internal or external acquired GRAPPA reference data for RMC are shown in Fig. 8. Quantitative evaluations, in Fig. 8A and 8B, do not show a clear difference in SSIM between RMC with integrated versus external ACS acquisition. However, for the continuous motion experiment the RMS discrepancy shows increased motion during the scan with external ACS, which reduced the baseline artifact level in the uncorrected external ACS images, as seen from the top row in Fig. 8C and the blue "No MC" data points in Fig. 8A. Motion parameters for all scans are shown in Supporting Information Figure S 5. Figures 8C and 8D show the reconstructed images corrupted by continuous and discrete motion respectively. Artifacts are evident in RMC images with both integrated and external ACS. Within-ET PMC results in superior image quality compared to Within-ET RMC with either integrated or external ACS in both tested motion patterns.

The results of the comparison of PMC and RMC performed on scans without GRAPPA acceleration (Subject 6) are shown in Fig. 9. The quantitative evaluations in Fig. 9A and Fig. 9B

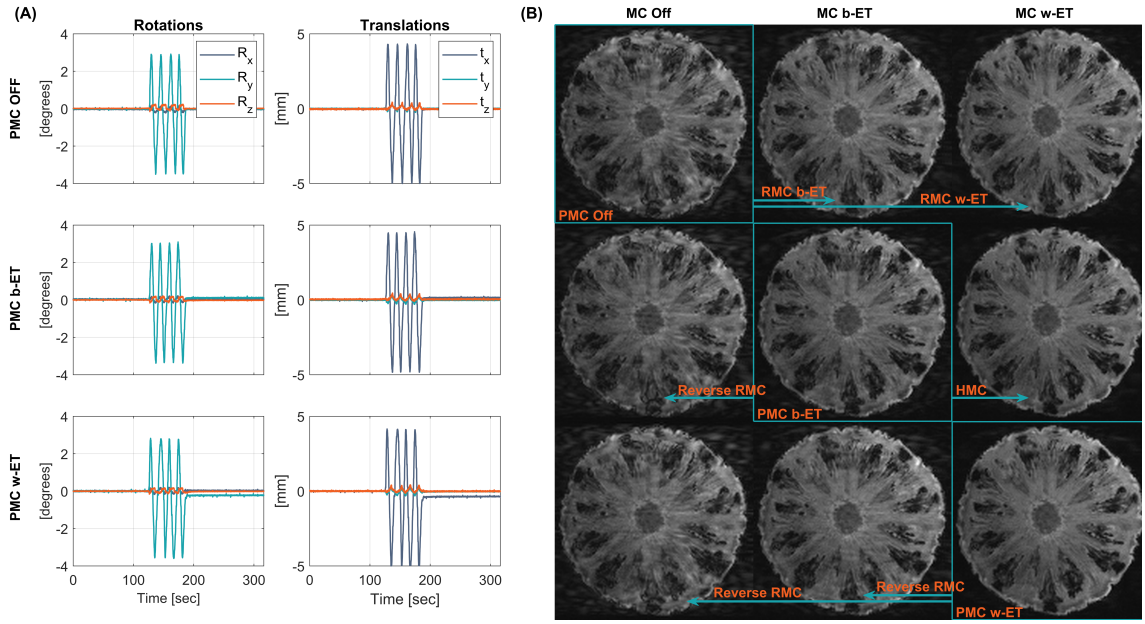

Fig. 5. Phantom comparison of MC OFF, PMC and RMC during periodic continuous motion. (A) Recorded motion parameters of the performed motion with start time 2 minutes into the sequence. (B) MPRAGE images along the diagonal show increasing image quality and were acquired with PMC off, Before echo train PMC (PMC b-ET), and Within echo train PMC (PMC w-ET). Images outside the diagonal are retrospectively corrected or reverse corrected versions of the highlighted image along the same row (indicated by the arrows). These images include RMC, reverse RMC and HMC. PMC: prospective motion correction; RMC retrospective motion correction; MC OFF: without motion correction; HMC: hybrid prospective, retrospective motion correction.

and the reconstructed images in Fig. 9C show that both methods lead to improved image quality. However, images corrected by RMC contain notably more motion artifacts compared to images corrected by PMC, although the motion in the PMC scans was higher. The recorded motion parameters are shown in Supporting Information Figure S 6.

IV. Discussion

The experimental results showed that the correction performance of PMC was superior to RMC during the tested discrete and continuous motion patterns. In the presence of continuous motion, increasing the correction frequency of PMC and RMC from no correction to Within-ET updates lead to an improvement in the image quality corresponding with a reduction in the encoding error of the correction. This improvement in image quality with correction frequency was also demonstrated with a hybrid approach that applied additional RMC to data acquired with Before-ET PMC. Experiments without GRAPPA acceleration confirmed that the superior performance of PMC compared to RMC is due to the lack of k-space undersampling.

A. Comparison of PMC and RMC

Both PMC and RMC improve the image quality substantially in cases of discrete and periodic continuous motion for the two tested motion amplitudes. PMC resulted in higher image quality than RMC and the improvement in quality increases when the amplitude of the motion is increased, as shown in Fig. 4. This is relevant to clinical scans where substantial head movement is expected. It also implies that the performance of PMC and RMC in research scans with compliant subjects is probably similar.

The periodic continuous motion was more challenging to correct retrospectively compared to the discrete motion patterns. For both tested motion amplitudes, RMC provides a reduction in the amount of motion artifacts, especially in the front of the brain (the region that moves the most during head shaking). However, RMC does not fully resolve the signal loss and ghosting as seen in Fig. 3.

PMC and RMC have not been directly compared in previous studies. Visual assessment of the results in Zahneisen et al, 2016 [27] shows similar performance of PMC and RMC during a discrete motion pattern, although there was substantial variation in motion amplitude between the PMC and RMC scans.

B. GRAPPA-related effects

In this study, the majority of the scans were acquired with GRAPPA acceleration, consistent with typical use of parallel imaging to accelerate 3D-encoded MRI, and with integrated

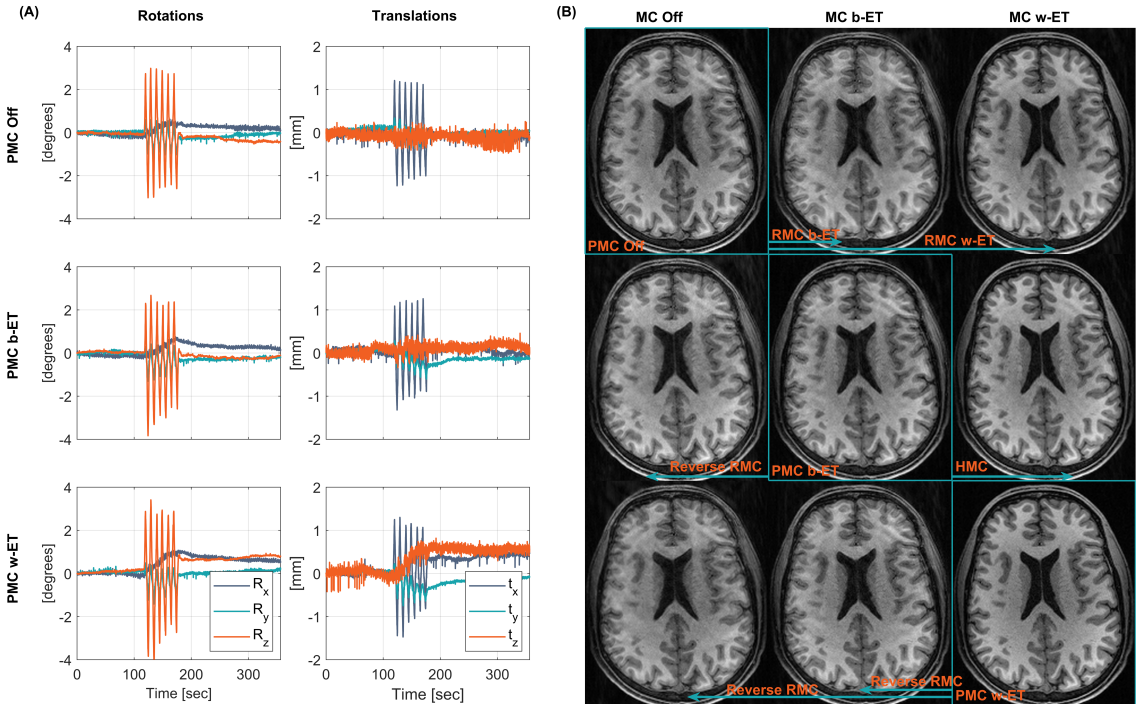

Fig. 6. In vivo comparison of MC OFF, PMC and RMC during periodic continuous motion (large amplitude, subject 2. (A) Recorded motion parameters of the performed motion. (B) MPRAGE images along the diagonal were acquired with PMC off, Before echo train PMC (PMC b-ET), and Within echo train PMC (PMC w-ET). Images outside the diagonal are retrospectively corrected or reverse corrected versions of the highlighted image along the same row (indicated by the arrows). These images include RMC, reverse RMC and HMC. PMC: prospective motion correction; RMC retrospective motion correction; MC OFF: without motion correction; HMC: hybrid prospective, retrospective motion correction.

ACS data. In our implementation of RMC based on a widely-used toolbox [37], both the estimation of GRAPPA weights and reconstruction of missing data were performed before the motion correction. This is not the case for PMC, where all the data, including the reference data, are motion corrected before the reconstruction. Using external ACS acquisition, to test whether estimation of the GRAPPA weights without intentional motion would improve final image quality, did not show a clear benefit in image quality, and PMC resulted in better image quality than RMC with either integrated or external ACS (Fig. 8).

Experiments without GRAPPA (Fig. 9) demonstrate that PMC leads to superior image quality, which is similar to the findings of the experiment with GRAPPA (Fig. 2, 3, and 8 and Supporting Information Figure S3). This demonstrates that the superior performance of PMC compared to RMC can be attributed to the lack of k-space undersampling violating the Nyquist criterion.

C. Under-sampled k-space during motion

This study has empirically confirmed the expected disadvantage of RMC for 3D-encoded sequences – that it suffers from k-space under-sampling in the presence of head rotation [8] – showing that there is a measurable image quality improvement with PMC. The repositioning of k-space lines in the RMC method to account for motion causes these Nyquist violations. This effect is seen in the corrected k-space from the scan during large periodic continuous motion in Supporting Information Figure S 4, which shows that the repositioning of the k-space lines during RMC resulted in under-sampled regions close to the center of k-space. Using methods that compensate for the k-space undersampling, such as motion-aware iterative parallel imaging reconstructions [45] , may reduce artifacts in the retrospectively corrected images.

We expect that these results based on sequential Cartesian k-space acquisition will generalize to situations when motion results in contiguous "chunks" of under-sampled k-space. The phase-encode ordering and relative timing of motion (e.g. see Supporting Information Figure S2) are relevant to the extent and location of k-space under-sampling when there is head

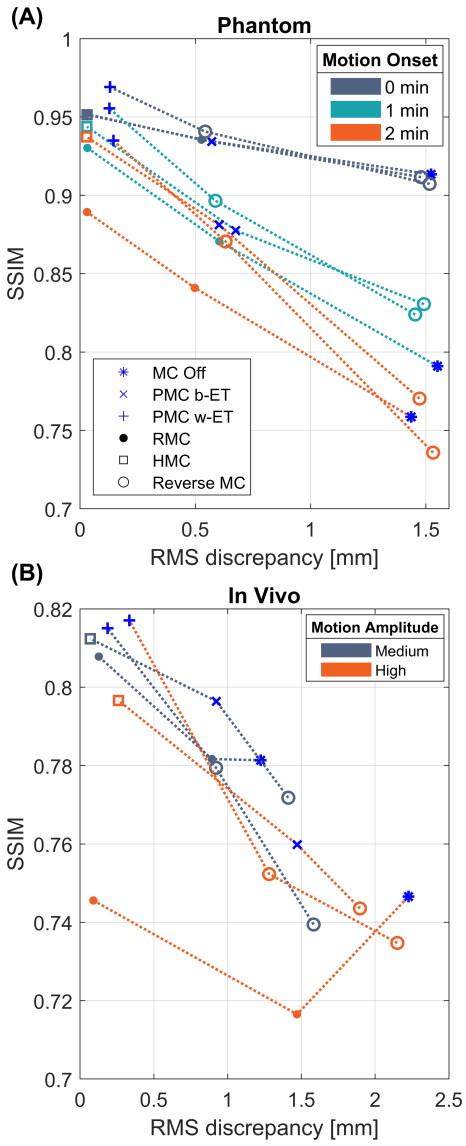

Fig. 7. Structural similarity index measure (SSIM) as a function of RMS discrepancy between true motion and encoded motion. Blue markers correspond to data acquired with PMC off, b-ET PMC, and w-ET PMC. Connected points represent images reconstructed from the same data. The color corresponds to a given type of motion. In the phantom scans (A) the colors correspond to the motion starting 0, 1, and 2 minutes into the sequences. In the in vivo scans (B) the colors correspond to the medium and high motion amplitude experiments. The MC off images in (A) show that motion occurring further into the sequences (closer to the k-space center) is more disruptive of the image quality. Both figures show that increasing the correction frequency from Before-ET to Within-ET results in lower RMS-discrepancy and higher image quality. PMC: prospective motion correction; RMC retrospective motion correction; MC OFF: without motion correction; HMC: hybrid prospective, retrospective motion correction; b-ET: before echo train; w-ET within echo train.

rotation. Similar comparisons with distributed [18] or radial [17, 31] k-space sampling are interesting areas of future work.

D. Effect of correction frequency on RMC performance

The results of the continuous motion experiments in Fig. 5, 6, and 7 show that increasing the correction frequency of RMC and thereby reducing the encoding error substantially improves the image quality. Previous work has shown that increasing the correction frequency of PMC in MPRAGE from no correction, to Before-ET, to Within-ET results in a gradual reduction of motion artifacts [26], and this study shows that the same is true for RMC.

This work also demonstrates that the correction frequency of a Before-ET PMC scan can be retrospectively increased to Within-ET. This hybrid prospective-retrospective MC improves the image quality substantially compared to the quality of the acquired Before-ET PMC images. The quantitative image quality of the HMC is also superior compared to Within-ET RMC from PMC off data. This suggests a hybrid approach with initial Before-ET PMC could ensure that the k-space is roughly uniformly sampled and subsequently RMC could fine-tune the acquired data.

The phantom experiment consisted of three scan sessions, where the performed motion pattern was initiated 0, 1, and 2 minutes into the sequence, respectively. The results in Fig. 7A and in Supporting Information Figure S 2 show that motion occurring further into the sequences causes more motion-related artifacts compared to the same motion occurring at the start of the sequence. This confirms that motion affecting the center of k-space is more detrimental to image quality as measured by SSIM.

E. Tracking noise

Although the results in this work show a superior correction performance of PMC, in general the PMC approach is sensitive to errors and noise from the tracking modality [27, 45, 46]. RMC can be less sensitive to tracking noise and it preserves the original uncorrected image because the correction takes place after all the data are acquired. Also, more effective temporal filtering of the tracking signal is possible retrospectively. Zahneisen et al. [27] and Maclaren et al. [45] have previously demonstrated that RMC can be used to reduce artifacts caused by tracking noise in a PMC scan. This was done by retrospectively estimating the residual tracking noise through filtering and then using reverse motion correction on the acquired PMC data. The hybrid approach of increasing the update frequency of a Before-ET PMC scan to a Within-ET MC retrospectively is a potential solution to the tracking noise if a Before-ET PMC scan is more robust to tracking noise.

Another synergy combining PMC and RMC is to estimate the uncorrected image through reverse correction as shown in Fig. 5 and 6. Reverse correction can be used for 3D-encoded sequences where retrospective correction is not limited by through-slice motion. The possibility of generating the uncorrected image with reverse motion correction [27, 40] simplifies the evaluation of PMC especially in a clinical setting where it is not possible to acquire scans with and without PMC during

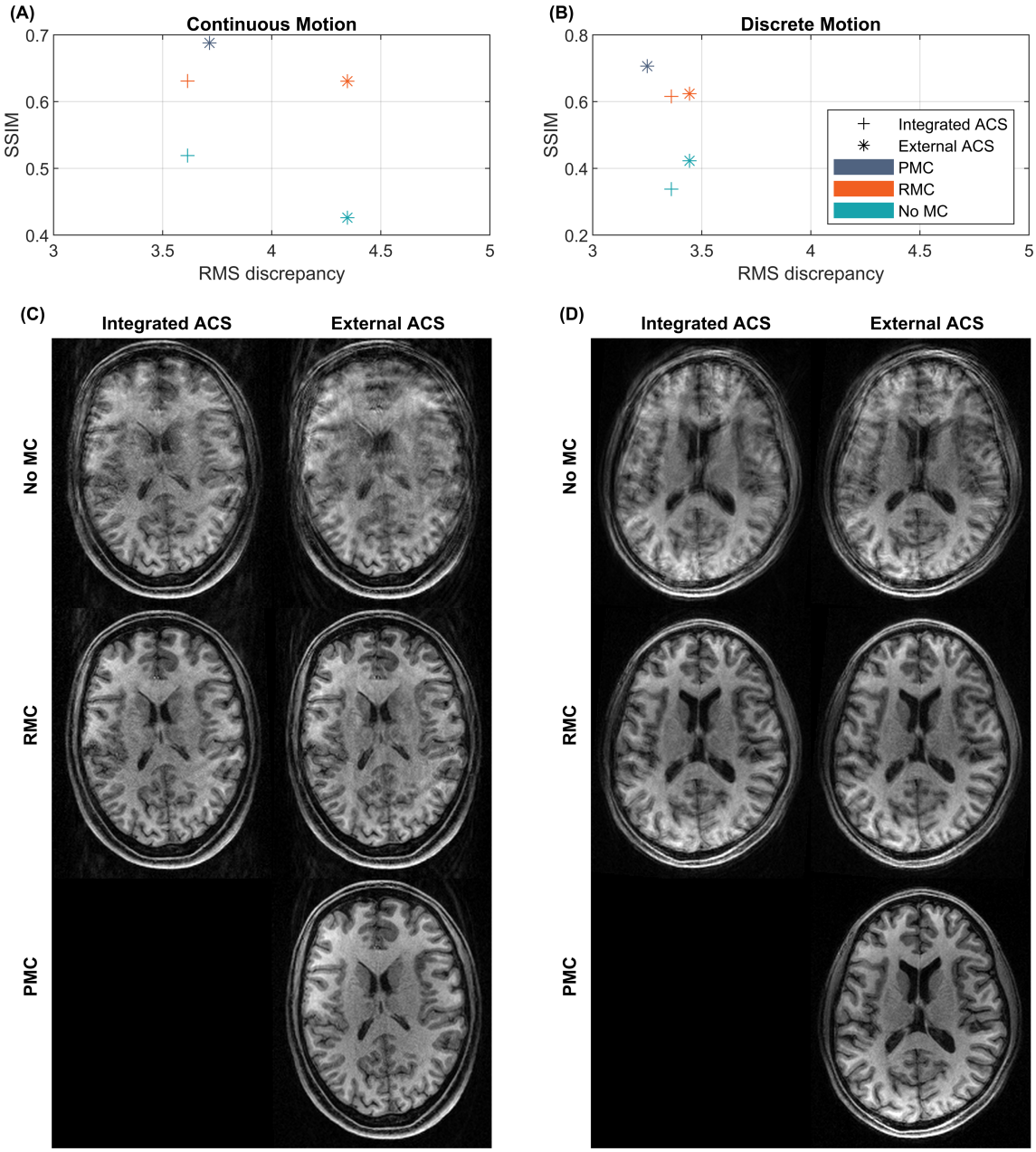

Fig. 8. Comparison of image quality of MPRAGE scans with integrated or externally acquired GRAPPA ACS data. Quantitative comparisons are shown in (A) and (B), where the structural similarity index measure (SSIM) relative to a scan without intentional motion and with external reference and no MC is plotted as a function of the root mean square (RMS) discrepancy. (C) Reconstructed images corrupted by continuous motion. (D) Reconstructed images corrupted by discrete motion. PMC: prospective motion correction; RMC retrospective motion correction; No MC: without motion correction; ACS: auto-calibration signal.

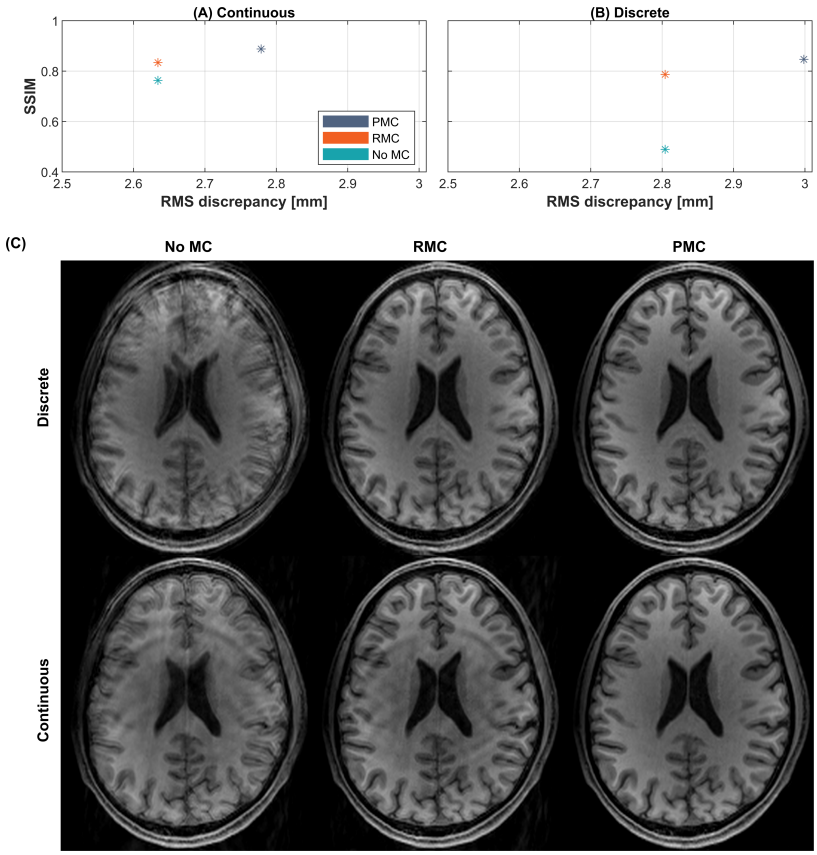

Fig. 9. Comparison of image quality of MPRAGE scans without GRAPPA. Quantitative comparisons are shown in (A) and (B), where the structural similarity index measure (SSIM) relative to a scan without motion correction and intentional motion is plotted as a function of the root mean square (RMS) discrepancy. (C) Reconstructed images corrupted by discrete or continuous motion. PMC: prospective motion correction; RMC retrospective motion correction; No MC: without motion correction; ACS: auto-calibration signal.

the same motion-pattern. In terms of implementation in the vendor image reconstruction, reverse correction would share the same framework as retrospective motion correction but would use the inverse of the motion transformations that were prospectively applied.

V. Conclusion

This study has demonstrated that the reduction in local Nyquist violations with prospective motion correction in Cartesian 3D-encoded MPRAGE leads to measurable improvements in image quality compared to retrospective motion correction. Comparisons were performed using the same markerless, high-frequency, optical motion tracking during discrete and continuous motion. In the presence of continuous motion, increasing the correction frequency of prospective and retrospective correction during MPRAGE echo-trains improves image quality. Hybrid correction combining PMC and RMC to retrospectively increase the correction frequency of data acquired with low-frequency Before-ET PMC also resulted in improved image quality.

Acknowledgment

We are grateful for support for this research which was provided in part by the National Institute of Biomedical Imaging and Bioengineering (R21EB029641); National Institute of Child Health and Development (R01HD093578, R01HD099846, R01HD085813); Innovation Fund Denmark (8053-00155B), and was made possible by resources provided by Shared Instrumentation Grants (S10OD025253 and MGH ECOR, 1S10RR023401, 1S10RR019307, and 1S10RR023043)

REFERENCES

[1] M. Reuter, M. D. Tisdall, A. Qureshi, R. L. Buckner, A. J. van der Kouwe, and B. Fischl, "Head motion during MRI acquisition reduces gray matter volume and thickness estimates," *NeuroImage*, vol. 107, pp. 107–115, 2015.

[2] M. D. Tisdall, M. Reuter, A. Qureshi, R. L. Buckner, B. Fischl, and A. J. van der Kouwe, "Prospective motion correction with volumetric navigators (vNavs) reduces the bias and variance in brain morphometry induced by subject motion," *NeuroImage*, vol. 127, pp. 11–22, 2016.

[3] J. B. Andre, B. W. Bresnahan, M. Mossa-Basha, M. N. Hoff, C. Patrick Smith, Y. Anzai, and W. A. Cohen, "Toward quantifying the prevalence, severity, and cost associated with patient motion during clinical MR examinations," *Journal of the American College of Radiology*, vol. 12, no. 7, pp. 689–695, 2015.

[4] R. D. Sanders, J. Hassell, A. J. Davidson, N. J. Robertson, and D. Ma, "Impact of anaesthetics and surgery on neurodevelopment: An update," *British Journal of Anaesthesia*, vol. 110, pp. 53–72, 2013.

[5] D. Blumenthal and M. Tavenner, "Anesthesia and Developing Brains — Implications of the FDA Warning," *The New England Journal of Medicine*, vol. 376, no. 10, pp. 905–907, 2017.

[6] J. M. Slipsager, S. L. Glimberg, J. Søgaard, R. R. Paulsen, H. H. Johannesen, P. C. Martens, A. Seth, L. Marner, O. M. Henriksen, O. V. Olesen, and L. Højgaard, "Quantifying the Financial Savings of Motion Correction in Brain MRI : A Model-Based Estimate of the Costs Arising From Patient Head Motion and Potential Savings From Implementation of Motion Correction," *Journal of Magnetic Resonance Imaging*, vol. 52, no. 3, pp. 731–738, 2020.

[7] E. M. Haacke and J. L. Patrick, "Reducing motion artifacts in two-dimensional Fourier transform imaging," *Magnetic Resonance Imaging*, vol. 4, no. 4, pp. 359–376, 1986.

[8] J. Maclaren, M. Herbst, O. Speck, and M. Zaitsev, "Prospective Motion Correction in Brain Imaging: A Review," *Magnetic resonance in medicine*, vol. 69, no. 3, pp. 621–636, 2013.

[9] A. J. W. Van der Kouwe, T. Benner, and A. M. Dale, "Real-time rigid body motion correction and shimming using cloverleaf navigators," *Magnetic resonance in medicine*, vol. 56, no. 5, pp. 1019–1032, 2006.

[10] N. White, C. Roddey, A. Shankaranarayanan, E. Han, D. Rettmann, J. Santos, J. Kuperman, and A. Dale, "PROMO: Real-time prospective motion correction in MRI using image-based tracking," *Magnetic Resonance in Medicine*, vol. 63, no. 1, pp. 91–105, 2010.

[11] M. D. Tisdall, A. T. Hess, M. Reuter, E. M. Meintjes, B. Fischl, and A. J. W. van der Kouwe, "Volumetric navigators for prospective motion correction and selective reacquisition in neuroanatomical MRI," *Magnetic resonance in medicine*, vol. 68, no. 2, pp. 389–399, 2012.

[12] D. Gallichan, J. P. Marques, and R. Gruetter, "Retrospective correction of involuntary microscopic head movement using highly accelerated fat image navigators (3D FatNavs) at 7T," *Magnetic Resonance in Medicine*, vol. 75, no. 3, pp. 1030–1039, 2016.

[13] T. E. Wallace, O. Afacan, M. Waszak, T. Kober, and S. K. Warfield, "Head motion measurement and correction using FID navigators," *Magnetic Resonance in Medicine*, vol. 81, no. 1, pp. 258–274, 2019.

[14] J. G. Pipe, "Motion correction with PROPELLER MRI: application to head motion and free-breathing cardiac imaging," *Magnetic Resonance in Medicine*, vol. 42, no. 5, pp. 963–969, 1999.

[15] L. Cordero-Grande, R. P. A. G. Teixeira, E. J. Hughes, J. Hutter, A. N. Price, and J. V. Hajnal, "Sensitivity Encoding for Aligned Multishot Magnetic Resonance Reconstruction," *IEEE Transactions on Computational Imaging*, vol. 2, no. 3, pp. 266–280, 2016.

[16] M. W. Haskell, S. F. Cauley, and L. L. Wald, "TArgeted Motion Estimation and Reduction (TAMER): Data consistency based motion mitigation for mri using a reduced model joint optimization," *IEEE Transactions on Medical Imaging*, vol. 37, no. 5, pp. 1253–1265, 2018.

[17] S. Kecskemeti, A. Samsonov, J. Velikina, A. S. Field, P. Turski, H. Rowley, J. E. Lainhart, and A. L. Alexander, "Robust motion correction strategy for structural MRI in unsedated children demonstrated with three-dimensional radial MPnRAGE," *Radiology*, vol. 289, no. 2, pp. 509–516, 2018.

[18] L. Cordero-Grande, G. Ferrazzi, R. P. A. Teixeira, J. O'Muircheartaigh, A. N. Price, and J. V. Hajnal, "Motion-corrected MRI with DISORDER: Distributed and incoherent sample orders for reconstruction deblurring using encoding redundancy," *Magnetic Resonance in Medicine*, vol. 84, no. 2, pp. 713–726, 2020.

[19] M. Zaitsev, C. Dold, G. Sakas, J. Hennig, and O. Speck, "Magnetic resonance imaging of freely moving objects: prospective real-time motion correction using an external optical motion tracking system," *Neuroimage*, vol. 31, no. 3, pp. 1038–1050, 2006.

[20] M. B. Ooi, S. Krueger, W. J. Thomas, S. V. Swaminathan, and T. R. Brown, "Prospective Real-Time Correction for Arbitrary Head Motion Using Active Markers," *Magnetic resonance in medicine*, vol. 62, no. 4, pp. 943–954, 2009.

[21] M. Aksoy, C. Forman, M. Straka, S. Skare, S. Holdsworth, J. Hornegger, and R. Bammer, "Real-time optical motion correction for diffusion tensor imaging," *Magnetic Resonance in Medicine*, vol. 66, no. 2, pp. 366–378, 2011.

[22] A. Aranovitch, M. Haeberlin, S. Gross, B. E. Dietrich, B. J. Wilm, D. O. Brunner, T. Schmid, R. Luechinger, and K. P. Pruessmann, "Prospective motion correction with NMR markers using only native sequence elements," *Magnetic Resonance in Medicine*, vol. 79, no. 4, pp. 2046–2056, 2018.

[23] A. van Niekerk, A. van der Kouwe, and E. Meintjes, "Toward "plug and play" prospective motion correction for MRI by combining observations of the time varying gradient and static vector fields," *Magnetic Resonance in Medicine*, vol. 82, no. 3, pp. 1214–1228, 2019.

[24] O. V. Olesen, M. R. Jørgensen, R. R. Paulsen, L. Højgaard, B. Roed, and R. Larsen, "Structured Light 3D Tracking System for Measuring Motions in PET Brain Imaging," in *SPIE Medical Imaging*, vol. 7625. International Society for Optics and Photonics, 2010, p. 76250X.

[25] J. M. Slipsager, A. H. Ellegaard, S. L. Glimberg, R. R. Paulsen, M. Dylan Tisdall, P. Wighton, A. Van Der Kouwe, L. Marner, O. M. Henriksen, I. Law, and O. V. Olesen, "Markerless motion tracking and correction for PET, MRI, and simultaneous PET/MRI," *PLoS ONE*, vol. 14, no. 4, pp. 1–17, 2019.

[26] R. Frost, P. Wighton, F. I. Karahanoğlu, R. L. Robertson, P. E. Grant, B. Fischl, M. D. Tisdall, and A. van der Kouwe, "Markerless high-frequency prospective motion correction for neuroanatomical MRI," *Magnetic Resonance in Medicine*, vol. 82, no. 1, pp. 126–144, 2019.

[27] B. Zahneisen, B. Keating, A. Singh, M. Herbst, and T. Ernst, "Reverse retrospective motion correction," *Magnetic Resonance in Medicine*, vol. 75, no. 6, pp. 2341–2349, 2016.

[28] D. Atkinson, D. L. Hill, P. N. Stoyle, P. E. Summers, S. Clare,

R. Bowtell, and S. F. Keevil, "Automatic compensation of motion artifacts in MRI," *Magnetic Resonance in Medicine*, vol. 41, no. 1, pp. 163–170, 1999.

[29] A. Loktyushin, H. Nickisch, R. Pohmann, and B. Schölkopf, "Blind retrospective motion correction of MR images," *Magnetic Resonance in Medicine*, vol. 70, no. 6, pp. 1608–1618, 2013.

[30] O. Norbeck, A. van Niekerk, E. Avventi, H. Rydén, J. Berglund, T. Sprenger, and S. Skare, "T1-FLAIR imaging during continuous head motion: Combining PROPELLER with an intelligent marker," *Magnetic Resonance in Medicine*, vol. 85, no. 2, pp. 868–882, 2021.

[31] D. Polak, S. Cauley, B. Bilgic, D. N. Splitthoff, P. Bachert, L. L. Wald, and K. Setsompop, "Scout Acquisition enables rapid Motion Estimation (SAME) for retrospective motion mitigation," in *28th Annual Meeting of the International Society of Magnetic Resonance in Medicine*, 2020, p. Abstract 463.

[32] F. Gretsch, H. Mattern, D. Gallichan, and O. Speck, "Fat navigators and Moiré phase tracking comparison for motion estimation and retrospective correction," *Magnetic Resonance in Medicine*, vol. 83, no. 1, pp. 83–93, 2020.

[33] M. Eschelbach, A. Aghaeifar, J. Bause, J. Handwerker, J. Anders, E. M. Engel, A. Thielscher, and K. Scheffler, "Comparison of prospective head motion correction with NMR field probes and an optical tracking system," *Magnetic Resonance in Medicine*, vol. 81, no. 1, pp. 719–729, 2019.

[34] J. M. Slipsager, S. L. Glimberg, L. Højgaard, R. R. Paulsen, A. J. W. V. D. Kouwe, O. V. Olesen, and R. Frost, "Comparison of Prospective and Retrospective Motion Correction for 3D Structural Brain MRI," in *28th Annual Meeting of the International Society of Magnetic Resonance in Medicine.*, 2020, p. Abstract 0466.

[35] O. V. Olesen, R. R. Paulsen, L. Hojgaard, B. Roed, and R. Larsen, "Motion Tracking for Medical Imaging: A Nonvisible Structured Light Tracking Approach," *IEEE transactions on medical imaging*, vol. 31, no. 1, pp. 79–87, 2012.

[36] O. V. Olesen, J. M. Sullivan, T. Mulnix, R. R. Paulsen, L. Hojgaard, B. Roed, R. E. Carson, E. D. Morris, and R. Larsen, "List-Mode PET Motion Correction Using Markerless Head Tracking: Proof-of-Concept With Acans of Human Subject," *IEEE transactions on medical imaging*, vol. 32, no. 2, pp. 200–209, 2013.

[37] D. Gallichan, "RetroMoCoBox Toolbox." [Online]. Available: https://github.com/dgallichan/retroMoCoBox

[38] M. A. Griswold, P. M. Jakob, R. M. Heidemann, M. Nittka, V. Jellus, J. Wang, B. Kiefer, and A. Haase, "Generalized Autocalibrating Partially Parallel Acquisitions (GRAPPA)," *Magnetic Resonance in Medicine*, vol. 47, no. 6, pp. 1202–1210, 2002.

[39] A. Schwarzl and F. Knoll, "Implementation of Non Uniform Fast Fourier Transformation." [Online]. Available: https://github.com/andyschwarzl/gpuNUFFT

[40] R. Frost, M. D. Tisdall, M. Hoffmann, B. Fischl, D. Salat, and A. J. van der Kouwe, "Scan-specific assessment of vNav motion artifact mitigation in the HCP Aging study using reverse motion correction," in *28th Annual Meeting of the International Society of Magnetic Resonance in Medicine*, 2020, p. Abstract 467.

[41] M. Jenkinson, "Measuring Transformation Error by RMS Deviation," Oxford Centre for Functional Magnetic Resonance Imaging of the Brain (FMRIB), Oxford, Tech. Rep., 1999.

[42] Yoo, T.S., M. J. Ackerman, W. E. Lorensen, W. Schroeder, V. Chalana, S. Aylward, D. Metaxas, and R. Whitaker., "Engineering and Algorithm Design for an Image Processing API: A Technical Report on ITK - The Insight Toolkit. In Proc. of Medicine Meets Virtual Reality,," *J. Westwood, ed., IOS Press Amsterdam*, vol. 85, pp. 586–592, 2002.

[43] M. Mccormick, X. Liu, J. Jomier, C. Marion, and L. Ibanez, "Itk: Enabling reproducible research and open science," *Frontiers in Neuroinformatics*, vol. 8, no. FEB, pp. 1–11, 2014.

[44] Z. Wang, A. C. Bovik, H. R. Sheikh, and E. P. Simoncelli, "Image quality assessment: From error visibility to structural similarity," *IEEE Transactions on Image Processing*, vol. 13, no. 4, pp. 600–612, 2004.

[45] J. MacLaren, K. J. Lee, C. Luengviriya, O. Speck, and M. Zaitsev, "Combined prospective and retrospective motion correction to relax navigator requirements," *Magnetic Resonance in Medicine*, vol. 65, no. 6, pp. 1724–1732, 2011.

[46] A. Singh, B. Zahneisen, B. Keating, M. Herbst, L. Chang, M. Zaitsev, and T. Ernst, "Optical tracking with two markers for robust prospective motion correction for brain imaging," *Magnetic Resonance Materials in Physics, Biology and Medicine*, vol. 28, no. 6, pp. 523–534, 2015.

SUPPORTING INFORMATION

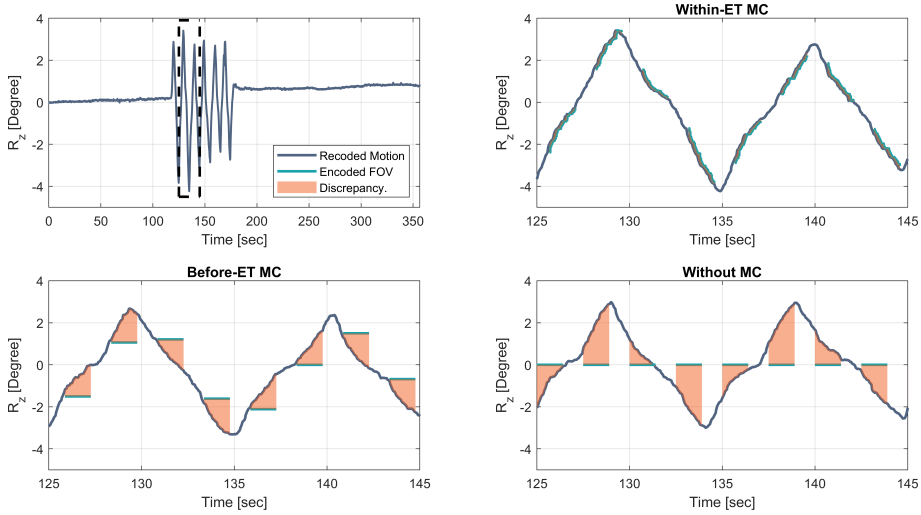

Fig. S 1. Discrepancy between the true motion and the encoded FOV of scan session 2, where the volunteer performed periodic continuous head motion with a medium amplitude. Only the discrepancy of rotation around the z-axis (Rz) is shown. MC: motion correction; ET: echo train.

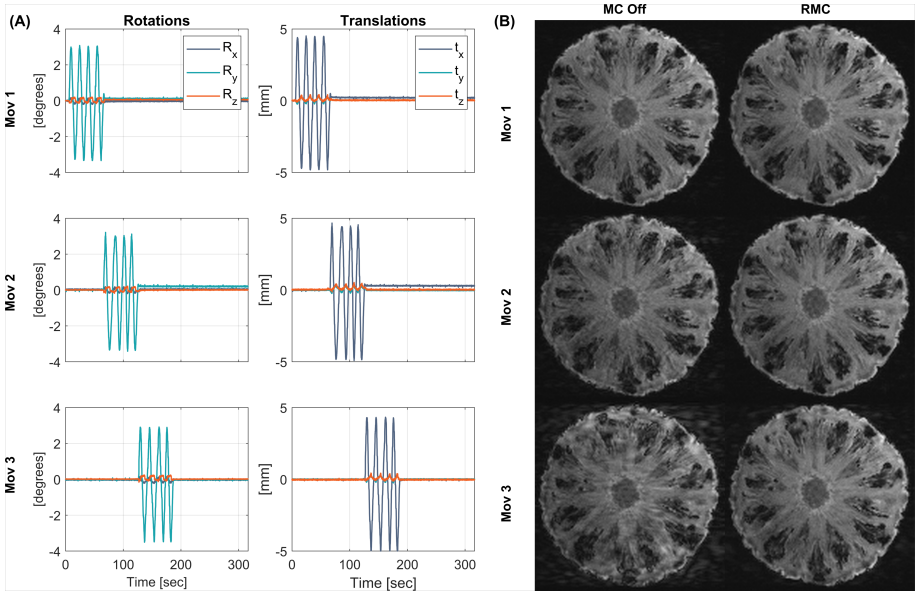

Fig. S 2. Phantom comparison of MC Off, and RMC during periodic continuous motion. (A) Recorded motion parameters of the performed motion with start time at 0, 1, and 2 minutes into the sequence (referred to as Mov 1, Mov 2, and Mov 3, respectively). (B) MPRAGE images reconstructed with and without high frequency RMC. The MC Off images show how more artifacts are present when the motion occurs closer to the center of k-space (acquired during the middle of the scan). MC Off: without motion correction; RMC: retrospective motion correction.

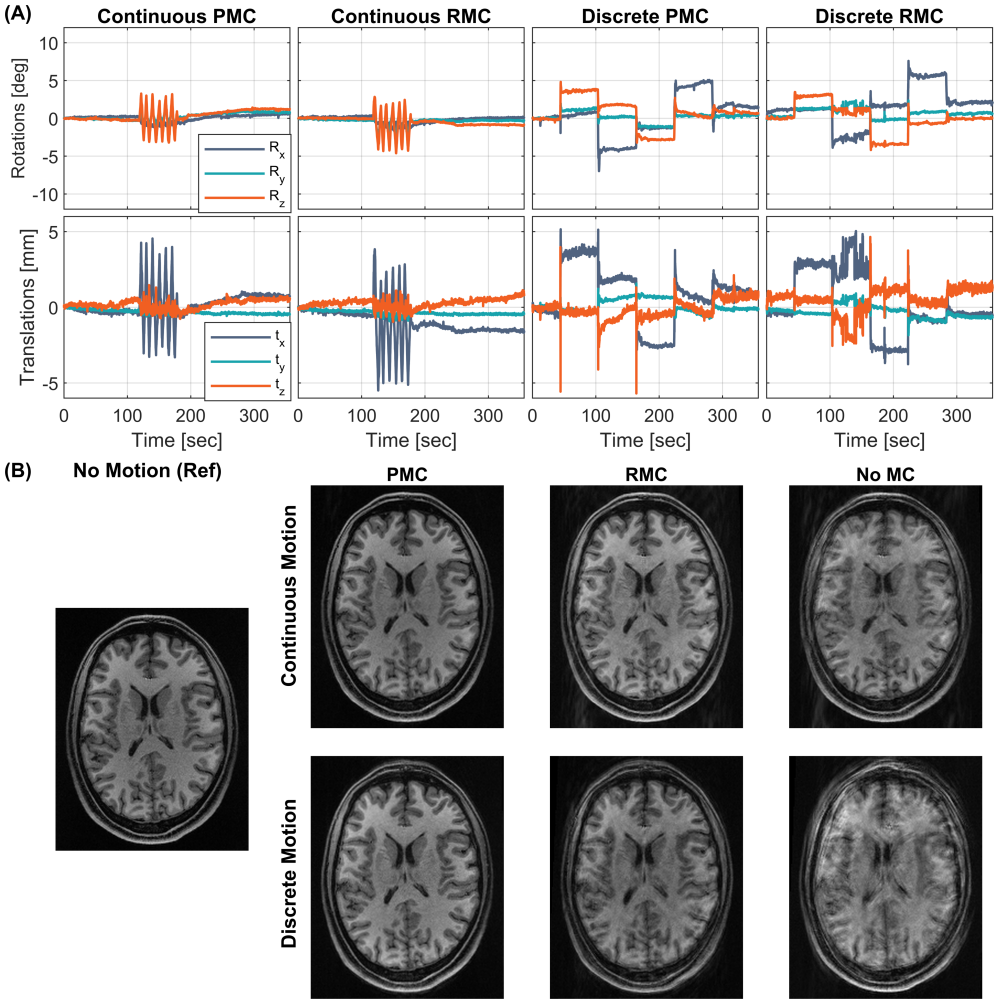

Fig. S 3. In vivo comparison of Within-ET PMC, Within-ET RMC, and No MC during periodic continuous and discrete motion (Subject 3). (A) The motion measurements during the four scans. (B) MPRAGE image reconstructions from scans with continuous and discrete motion, with PMC, RMC, and no correction. The leftmost MPRAGE image was acquired in a scan with no motion and without motion correction and was used as a reference for image quality. PMC: prospective motion correction; RMC retrospective motion correction; No MC: without motion correction; Within-ET: within echo train.

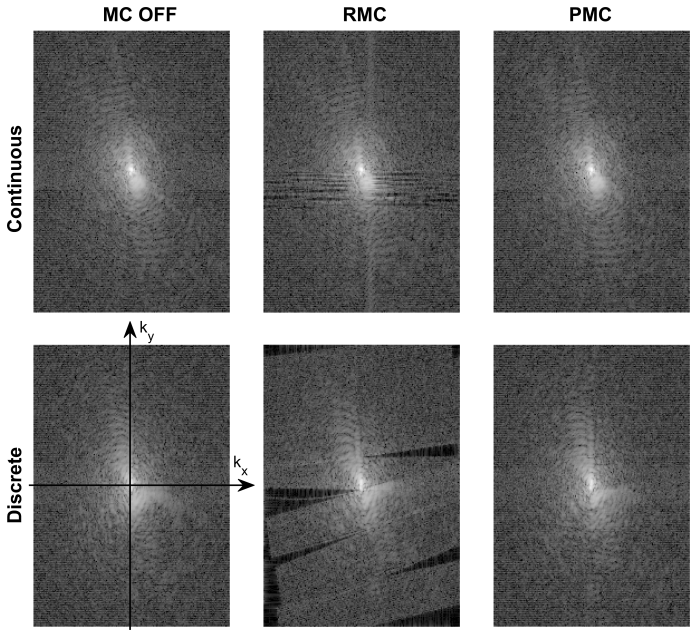

Fig. S 4. The magnitude of the k-space with MC Off, RMC, and PMC from a single receiver channel. The k-space data were acquired during periodic continuous (subject 2) and discrete motion (subject 1) with large amplitude. The k-space data are from one receiver channel and the logarithm was applied for better visualization. PMC: prospective motion correction; RMC retrospective motion correction; MC OFF: without motion correction.

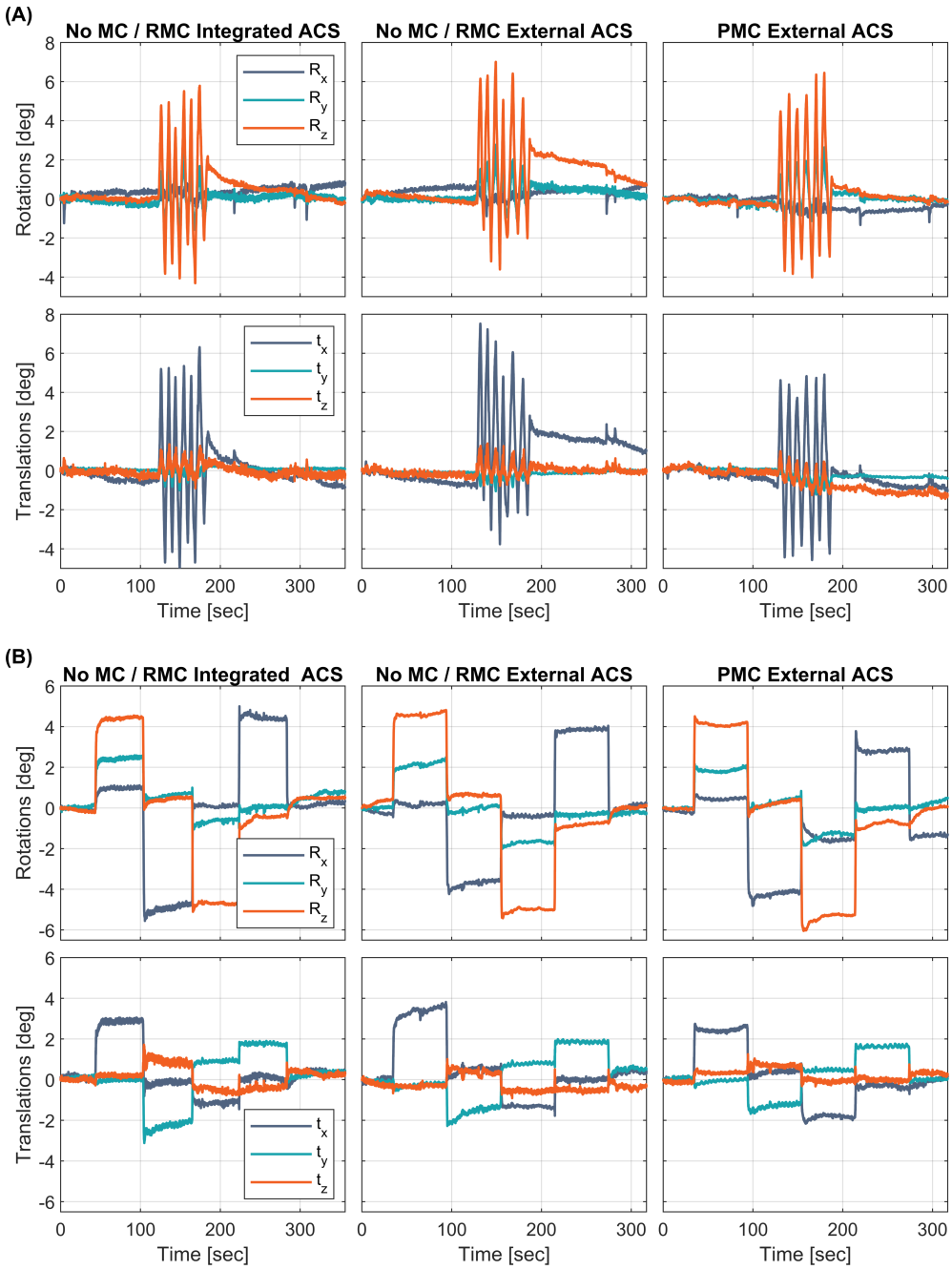

Fig. S 5. Motion parameters from the comparison of image quality of MPRAGE scans with integrated or externally acquired GRAPPA ACS data. (A) Continuous motion. (B) Discrete motion. PMC: prospective motion correction; RMC retrospective motion correction; No MC: without motion correction; ACS: auto-calibration signal.

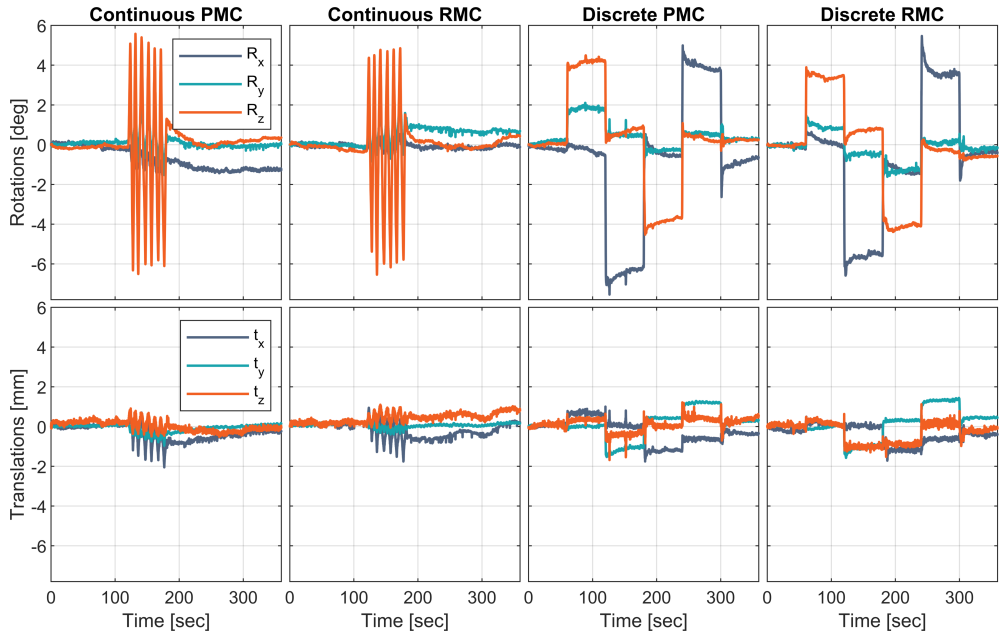

Fig. S 6. Motion parameters from the comparison of image quality of MPRAGE scans without GRAPPA. PMC: prospective motion correction; RMC retrospective motion correction.